

## 11. Nejvýznamnější prestižní publikace

- [1] J. Libich, S. Zvánovec, „Influences of Turbulences in Near Vicinity of Buildings on Free Space Optical Links“, *IET Microwaves, Antennas & Propagation*, 2011, vol. 5 , issue 9, p. 1039 - 1044.
- [2] S. Zvánovec, P. Pechač, „Validation of Rain Spatial Classification for High Altitude Platform Systems“, *IEEE Trans. on Antennas and Propagation*, 2011, vol. 59, issue 7, p. 2746-2750.
- [3] M.Komanec, P. Honzátko, S. Zvánovec, „Single-shot all-optical sampling oscilloscope using a polarization-maintaining resonator for pulse replication“. *Microwave and Optical Technology Letters*. 2010, vol. 52, no. 11, p. 2452-2456. ISSN 0895-2477.
- [4] P. Černý, P. Piksa, S. Zvánovec, T. Kořínek, V. Kabourek, „Improved Axial Excitation of Fabry-Perot Resonator for High Resolution Spectroscopy Applications“, *Microwave and Optical Technology Letters*. 2011, vol. 53, no. 11, p. 2456-2462. ISSN 0895-2477.
- [5] S. Zvánovec, P. Pechač, „Rain Spatial Classification for Availability Studies of Point-to-Multipoint Systems“, *IEEE Transactions on Antennas and Propagation*, vol. 54, no. 12, 2006. pp. 3789-3796.
- [6] S. Zvánovec, P. Černý, P. Piksa, T. Kořínek, P. Pechač, et al., „The use of the Fabry-Perot interferometer for high resolution microwave spectroscopy“. *Journal of Molecular Spectroscopy*. 2009, vol. 256, no. 1, p. 141-145. ISSN 0022-2852.
- [7] M. Polívka, M. Švanda, P. Hudec, S. Zvánovec, „UHF Radiofrequency Identification of People in Indoor and Open Areas“, *IEEE Transactions on Microwave Theory and Techniques*, volume 57, Issue 5, Part 2, , pp.1341-1347, May 2009.
- [8] S. Zvánovec, P. Piksa, M. Mazánek, P. Pechač, „A Study of Gas and Rain Propagation Effects at 48GHz for HAP Scenarios“, *EURASIP Journal on Wireless Communications and Networking* , 2008, vol. 5, no. 1, pp. 1-7.

Published in IET Microwaves, Antennas & Propagation  
 Received on 30th December 2010  
 Revised on 11th March 2011  
 doi: 10.1049/iet-map.2010.0630

In Special Section on Selected Papers from Mosharaka  
 International Conference on Communications,  
 Propagation and Electronics (MIC-CPE2010)



ISSN 1751-8725

# Influences of turbulences in near vicinity of buildings on free-space optical links

J. Libich S. Zvanovec

Department of Electromagnetic Field, Czech Technical University, Technicka 2, Prague 166 27, Czech Republic  
 E-mail: xzvanove@fel.cvut.cz

**Abstract:** Free-space optical systems offer many advantages for modern wireless communication compared to classical radio-band systems. Nevertheless, unlike fibre optics, their availability is highly affected by atmospheric disturbances. This study discusses the influences of temperature gradients around buildings that cause turbulent areas within the atmosphere, leading to the spatial change of the refractive index and consequently resulting in the bending or widening of transmitted optical beams. The influences of a nearby building on free-space optical links are discussed on the basis of measured data.

## 1 Introduction

Free-space optics (FSO) introduce a line-of-sight optical wireless communication technology which uses narrow optical beams for the transmission of information [1]. FSO offer many advantages for modern communication, including larger frequency bandwidths and substantially higher available data rates, immunity to interference, free license, higher safety of transmission due to narrow optical beams and so on [1]. Nevertheless, many factors may affect an optical beam causing the extinction or fluctuation of the received optical signal. Some of the most important effects – including absorption by atmospheric gases, scattering of small particles, beam wandering and scintillation caused by thermal turbulence within the transmission medium and the non-homogeneities of the refractive index – are described in [2–5].

Most FSO links are nowadays deployed in dense urban areas, where thermal influences (owing to building heating, air-conditioning, wind circulation etc.) can be substantial. It would therefore be beneficial to investigate the statistical influence of turbulences on FSO links not only in open areas but also in the vicinity of buildings. To support system performance analyses, a measurement campaign has been set up at the Czech Technical University in Prague (CTU). The goal of this paper is to demonstrate the relationship between fluctuation of the received optical power and temperature gradients along the path of the optical beam caused by turbulence around buildings.

The paper is organised along the following pattern. It opens with a discussion of the performance of the optical link, based on a measurement of the free-space optical link reception statistics and turbulent atmosphere effects and providing essential background information. After this the measurement campaign performed on the CTU campus is introduced

in detail. In the next part, measured results from the FSO link, meteorological stations and a special thermal sensor line are analysed and compared to typical turbulence statistics. A discussion follows on the specific dependence of the turbulence features on the distance from the building. This paper concludes with a brief summary.

## 2 Scintillation due to turbulences

Scintillation and wandering of optical beams are mainly caused by thermal turbulence within the transmission medium and non-homogeneities of the refractive index. As air circulates within the urban environment, assuming temporal gradients from buildings and the ground, thermal characteristics can change dramatically along the optical link. For instance, temporal differences of up to 13°C/100 m were observed during a study of airflow distribution inside street canyons in [6]. Such thermal divergences result in a divergence of the beam and the fluctuation of received optical power over time. The frequency of received signal fluctuations can reach up to 200 Hz [2]. The variance of scintillation ( $\sigma_\chi^2$ ) can be expressed by Rytov variance [5, 7]

$$\sigma_\chi^2 = 1.23 C_n^2 \left( \sqrt{\left( \frac{2\pi}{\lambda} \right)^7 L^{11}} \right) \quad (1)$$

where  $\lambda$  represents the wavelength and  $L$  is the length of the link.  $C_n^2$  introduces the so-called refractive index structure parameter – a vital measure of turbulence strength. Extensive research has been carried out, especially in cases of vertical variations of the structure parameter. The

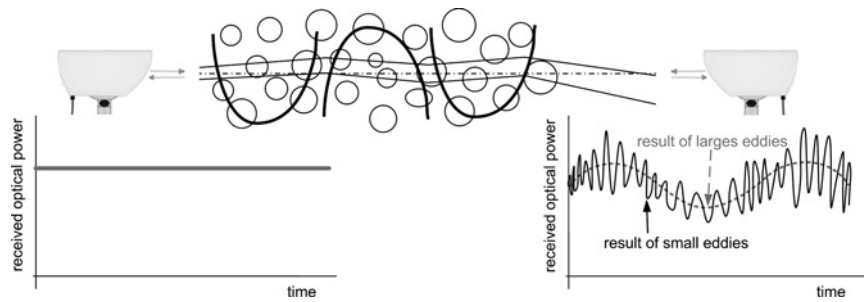


**Fig. 1** Demonstration of the turbulent atmosphere influence on a free-space optical link

Hufnagel–Valley model [8] is used for altitude  $h$  dependence

$$C_n^2(h) = 0.00594 \left(\frac{v}{27}\right)^2 (10^{-5}h)^{10} \exp\left(-\frac{h}{1000}\right) + 2.7 \times 10^{-16} \exp\left(-\frac{h}{1500}\right) + A \exp\left(-\frac{h}{100}\right) \quad (2)$$

where  $A$  is the reference parameter (for ground level around  $1.7 \times 10^{-14} \text{ m}^{-2/3}$ ) and  $v$  stands for the root mean square (RMS) of wind speed. For terrestrial sites (up to 100 m of the Earth’s atmosphere) the optical turbulence described by  $C_n^2$  reaches typical values ranging from  $10^{-17} \text{ m}^{-2/3}$  (weaker turbulence) to  $10^{-13} \text{ m}^{-2/3}$  (stronger turbulence). According to [8] optical turbulence shows approximately diurnal cycles with peaks during midday hours and minima near sunrise and sunset.

A submarine laser communication (SLC) day model derived empirically from averaged measured data [9] proposes for terrestrial links

$$C_n^2(h) = 1.7 \times 10^{-14}, \quad 0 < h < 18.5 \text{ m} \\ = 3.13 \times 10^{-13} / h^{1.05}, \quad 18.5 < h < 240 \text{ m} \quad (3)$$

and a SLC night model [9] suggests

$$C_n^2(h) = 8.4 \times 10^{-15}, \quad 0 < h < 18.5 \text{ m} \\ = 2.87 \times 10^{-12} / h^2, \quad 18.5 < h < 110 \text{ m} \quad (4)$$

The classical view of turbulence derives from the Kolmogorov theory of turbulences [4, 10]. Turbulence energy injection results in the breakup of large-scale structures into small-scale structures. It assumes that the small-scale structures are statistically homogeneous, isotropic and independent of the large-scale structure. The source of energy is wind or thermal conduction.

Randomly distributed cells of different refractive indexes (so-called eddies) can occupy areas from tens of centimetres up to units of kilometres. The amplitude as well as the frequency of received optical signal scintillations is subsequently highly dependent on the turbulent cell size to beam diameter ratio. In this regard, an optical beam is deviated/bent in the case of large turbulent areas, widened in the case of a small area or, most typically, a combination of both mechanisms can be observed [1] (see the illustration of the turbulent zones influence on received optical power depicted in Fig. 1).

Many statistical models were proposed to describe received signal fluctuations caused by atmospheric turbulence. The most widely used statistical models include lognormal distribution,  $K$ -distribution or gamma–gamma distribution [7]. Weak turbulences have been proved to have a probability density function (PDF) of the lognormal distribution (5) [11] while for strong turbulences, the  $K$ -distribution (6) [12] is used.

$$f(I) = \frac{1}{\sqrt{2\pi\sigma_I^2}} \exp\left\{-\frac{(\ln I/I_0 + \sigma_I^2/2)^2}{2\sigma_I^2}\right\}, \quad I > 0 \quad (5)$$

$$f(I) = \frac{2\alpha}{\Gamma(\alpha)} (\alpha I)^{(\alpha-1)/2} K_{\alpha-1}(2\sqrt{\alpha I}), \quad I > 0 \quad (6)$$

$\sigma_I^2$  is the scintillation index,  $I$  and  $I_0$  denote the irradiance (intensity of the optical wave) and its mean value in cases without turbulence.  $K_j(x)$  stands for a modified Bessel function of the second kind,  $\Gamma(x)$  is the gamma function and  $\alpha$  introduces the effective number of discrete scatterers.

Under the assumption that small-scale irradiance fluctuations are modulated by large-scale irradiance fluctuations of the propagating wave, gamma–gamma distribution can be utilised in a free-space optical channel. This can be expressed by [13]

$$f(I) = \frac{2(\alpha\beta)^{(\alpha+\beta)/2}}{\Gamma(\alpha)\Gamma(\beta)} I^{(\alpha+\beta)/2-1} K_{\alpha-\beta}(2\sqrt{\alpha\beta I}), \quad I > 0 \quad (7)$$

where  $\alpha$  and  $\beta$  are the effective numbers of small- and large-scale eddies defined in [13, 14]. Several analyses of FSO bit error rate dependences on turbulence were accomplished in [12, 13, 15–17]. The method of turbulence mitigation was proposed in [18]. For more details on particular statistics, see [7].

### 3 Measurements

In this section, the measuring system will be introduced and then turbulence features in the near vicinity of buildings together with FSO-link performance characteristics will be discussed based on actual measured data.

#### 3.1 Measuring system

To validate the influence of building heating effects on the free-space optical link, an experimental campaign was set up in the university campus of the Faculty of Electrical Engineering, Czech Technical University in Prague (Czech Republic). Two free-space optical transceivers WaveBridge 500 by Plaintree [19] were placed on the roofs of two eight-story buildings in the CTU campus, approximately 30 m above ground level (see the measuring system deployment in Fig. 2). This allowed us to build an optical link with a length

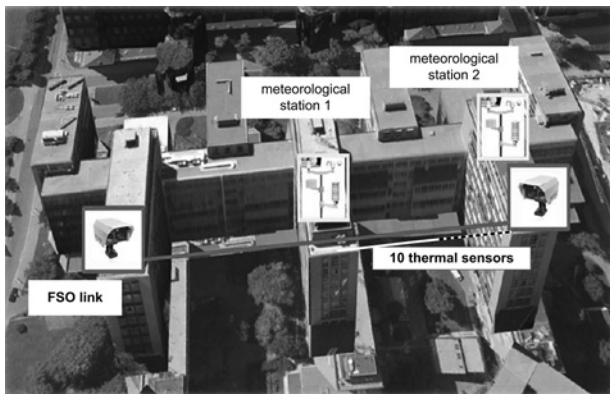


**Fig. 2** Deployment of the FSO link and weather sensors

of around 120 m. The optical wireless system works at a wavelength of 850 nm, transmitted power was set at 20 dBm and the LED beamwidth is  $1^\circ$ . The data rate 150 Mbps (OC-3) has been set in the link, while a router on one side returns back the sent data. Received optical power detected in terms of a strength signal indicator is read using an adjusted digital voltmeter and stored on computer – levels of the received optical power corresponding to the voltage were carefully calibrated. At the time this paper was submitted, a second free-space link consisting of a four-beam free-space optical communication systems FlightStrata G by LightPointe (1.25 Gbps of full-duplex, VCSEL at 850 nm) is being established at the Department of Electromagnetic Field, CTU.

Data from two meteorological stations WS981 by Anemo Corporation, Czech Republic, [20] located in the middle of the link and one of the FSO transceivers, respectively (measuring network configuration and setup for system performance monitoring are shown in Fig. 2) were used for further analyses. The first station collected data recording the temperature and humidity (a temperature sensor  $-30$  to  $+70^\circ\text{C}$  and hygrometer), as well as atmospheric pressure (barometer with range 800–1200 hPa), precipitations (heated tipping-bucket rain gauge with the collecting area of  $500\text{ cm}^2$ , and the rain amount per one tip 0.1 mm) and the speed and direction of the wind (anemometer AN 955C). The second station gathered temperature, atmospheric pressure and precipitation data.

The temperature gradient was measured using a system of ten thermal sensors TQS3 E by the Papouch Corporation, Czech Republic (temperature measured within a range of  $-55$  to  $+125^\circ\text{C}$  with a resolution of  $0.1^\circ\text{C}$ ), equidistantly spaced (with a distance of 2 m between sensors) on the cable at the first quarter of the free-space optical link (approximately 2 m below the optical link). In this way, thermal gradients are observed in various places around buildings, that is, above the two buildings and from close proximity to the building to a point halfway between both building blocks.

## 4 Results

Samples of the dependency of received optical power and temperature as measured during two days in April 2010 are shown in Fig. 3a. Table 1 then gives an example of received signal fluctuations in terms of deviations of the structural parameter of the refractive index and a correlation coefficient between temperature (measured by the meteorological station 2) and FSO received power level for different time periods in November 2009. In particular, this clearly demonstrates the difference between the short and

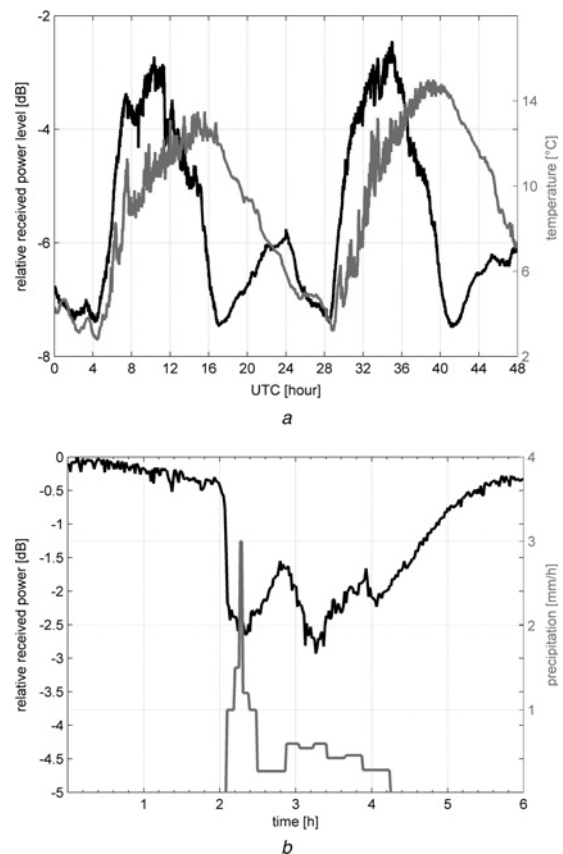


**Fig. 3** Sample of measured data

*a* Normalised received optical power and temperature during a two-day period in April 2010

*b* Dependence of normalised received optical power on precipitation measured on 15th of March 2010

**Table 1** Example of enumerated parameters of thermal influence on FSO link

Number of days [-]	2	10	30
$\Delta C_n^2 [\text{m}^{-2/3}]$	$4.7 \times 10^{-17}$	$9.3 \times 10^{-17}$	$2.7 \times 10^{-16}$
$r [-]$	0.676	0.371	0.195

relatively long time periods of the data sets. The correlation coefficient  $r$  was calculated using the following equation [21]

$$r = \frac{\text{Cov}(X, Y)}{\sqrt{\text{Var}(X)\text{Var}(Y)}} \quad (8)$$

where  $\text{Cov}(X, Y)$  is covariance and  $\text{Var}(X)$  and  $\text{Var}(Y)$  stand for variations of random variables  $X$  and  $Y$ . In our case,  $X$  and  $Y$  introduced the received optical power and measured temperature. Other correlations can be found in relation to FSO links calculated between laser beams and ideal Gaussian beams as determined during laboratory measurements of influences of turbulences on a laser beam, for example, in [22, 23].

The dependence of rain intensity on received power level as measured on 15th of March 2010 is depicted in Fig. 3b. It should be mentioned that rain does not influence optical links as much as atmospheric turbulences or fog scattering, contrary to the millimetre waveband, where significant rain attenuation can be observed [24, 25].

Fig. 4 demonstrates a measured influence of turbulences on FSO – expressed in terms of the refractive index structure parameter determined from fluctuations of received optical power by (1). It was evaluated over several calculation windows and compared with the refractive structure parameter derived from thermal variations in the atmosphere as described below. The best results were obtained within a 1 h span. Contrary to the results published in [26], where maximal turbulences were observed in diurnal periods from 9 am to 3 pm, in the case of the tested free-space optical link crossing buildings, an earlier diurnal increase of the refractive index structure parameter – from approximately 5 am – was observed with maximum values at around 8:30 am. The values of the scintillation indexes (normalised variance of the received optical power) reached by recalculation to the link length were eight times higher than those observed in [27].

Compared to log-normal measurement statistics presented for several maritime links in [28], the normalised scintillation index (by a mean value of 0.013) was not as strictly followed by a fitted log-normal cumulative function in our measurement (see the cumulative probability of normalised scintillation index from September 2010 depicted in Fig. 5a). For higher scintillation indices (cumulative probabilities higher than 0.94) the gamma–gamma statistical approach dominates. The fit error calculated according to [28] as the difference between measured data and the particular statistical model is shown in Fig. 5b. In the case of the log-normal model, the overall fitting quality measure – RMS error – reached a value of 0.0239. This is quite a huge difference from the theoretical assumption – compared to [28], where RMS errors were almost ten times smaller in case of maritime optical links having lengths 6, 9.4, 17.7 and 23.6 km. The worst fit was observed with the gamma–gamma statistical model, where an RMS error of 0.0409 was enumerated.

Based on statistics derived from sensor line measurements, the thermal influence of buildings was analysed. An example of thermal distribution measured on the 15th of September 2010 from approximately 8 am is shown in Fig. 6 (sensors are placed in the direction from the building, i.e. the 0th placed on the building, and the 10th at a distance of 20 m).

Significant thermal variations were observed along the measured path. At the beginning of the measurement campaign, undesirable heating of sensors by sunshine was distinguished. Therefore in the next step, sensors had to be improved by an upper alumina shield with special holes enabling even top-down air circulation.

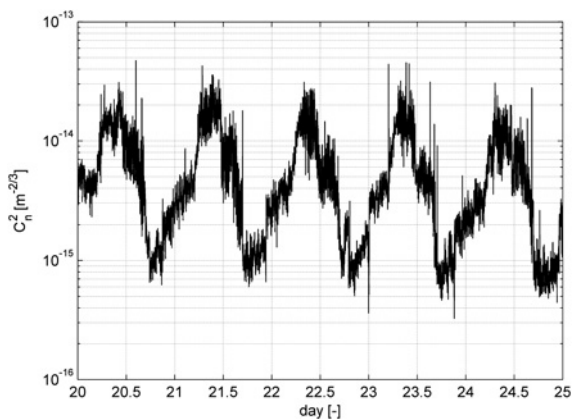


Fig. 4 Refractive index structure parameter determined by (1) from fluctuations of FSO received signal measured in September 2010

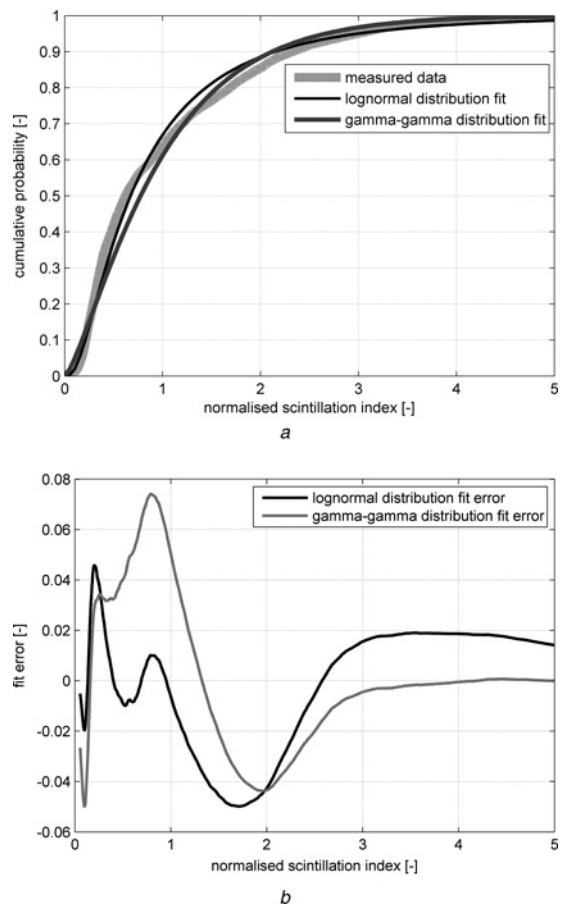


Fig. 5 Comparison of measured and theoretically derived statistics

- a Cumulative probability of normalised scintillation index from September 2010
- b Fit error between measured data and the calculated model

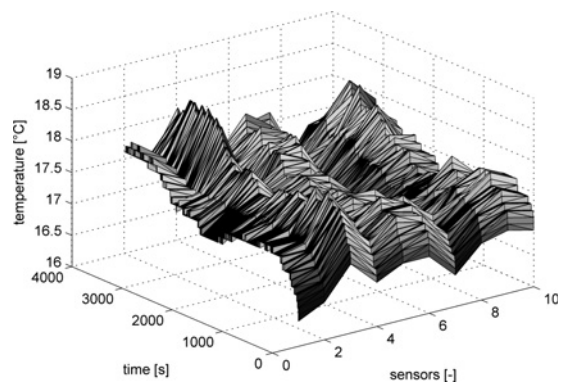


Fig. 6 Thermal distribution measured by the sensor line from 8:23 am on 15th of September 2010

To validate the influences of the turbulent zones, the refractive index structure parameter was determined from the thermal sensor line measured data using the empirical equation

$$C_n^2 = \left(79 \times 10^{-6} \frac{P}{T^2}\right)^2 \times \frac{(T_1 - T_2)^2}{R^{C_{par}}} \quad (9)$$

where  $T_1$  and  $T_2$  stand for temperatures measured by two adjacent thermal sensors separated by a distance  $R$ ,  $T$

represents mean temperature from all sensors and  $P$  introduces atmospheric pressure. Parameter  $C_{\text{par}}$  represents the thermal influence expressed by the so-called temperature structure function [10]. Equation (9) has a physical background in the relation between the spatial fluctuations of the refractive index (given by  $C_n^2$ ) and temperature (thermal structure parameter  $C_T^2$ ) [4]

$$C_n^2 = \left( \frac{\partial n}{\partial T} \right)^2 C_T^2 \quad (10)$$

Based on Kolmogorov statistics of fluctuations, it was determined in [29] that for vertical profiles, the value 2/3 of  $C_{\text{par}}$  is prevalent in the atmosphere when the following condition is satisfied

$$l_0 \leq R < L_0 \quad (11)$$

It characterises the dissipation range (inertial range) from largest eddies expressed by diameter  $L_0$  (up to outer scale of turbulence) towards the smallest ones with a diameter of  $l_0$ .  $C_{\text{par}} = 2$  was determined for smaller sensor separations  $R < l_0$  [4]. It has to be mentioned that in the above-mentioned cases, either the vertical profile of turbulences were measured by balloon thermal radiosondes or horizontal measurements were performed in an open area.

Contrary to the above-mentioned open-field measurements, in our case, when the link passed a built up area,  $C_{\text{par}}$  tended to reach a value of 2 even in the dissipation range (more specifically  $C_{\text{par}} = 1.96$  was optimised from Kolmogorov statistics of measured data). Therefore in the next analyses performed  $C_{\text{par}}$  was equal to 2. The refractive index structure parameter dependence on different distances from the building, which was determined from thermal sensors line measured data (September 2010) by using (9), is depicted in Fig. 7. When compared to Fig. 6, a very close resemblance can be distinguished, especially for smaller sensor separations. The highest daily correlation of up to 0.874 was observed in the case of thermal sensor separation  $R = 8$  m. For sensor separations higher than 12 m, correlations to FSO data rapidly decrease because such distances very often exceeded the diameters of the turbulence zones.

From the measured data, it was seen that turbulence emerges approximately in the first 1–2 m surrounding

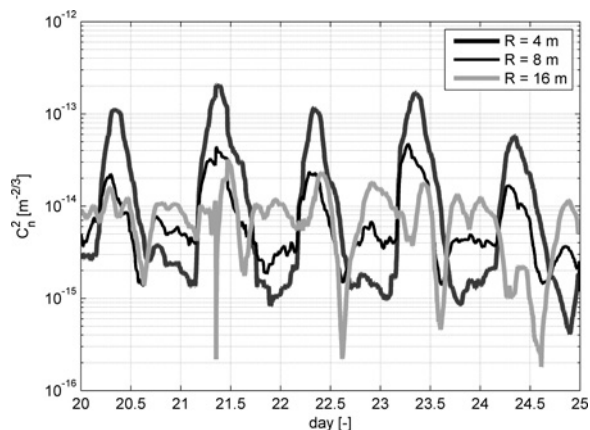


**Fig. 7** Refractive index structure parameter dependence for different distances from a building as determined by (9) from thermal sensors line measurement in September 2010

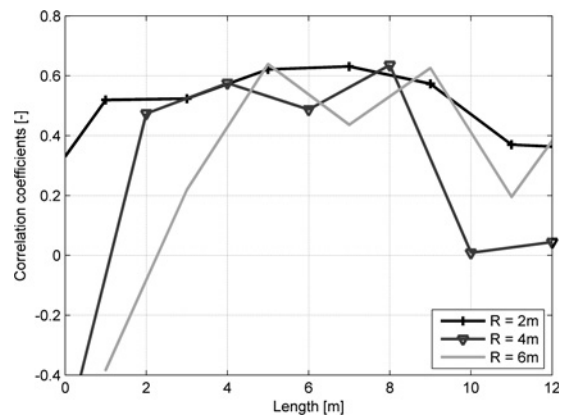


**Fig. 8** Dependence of the mean correlation coefficient between the refractive index structure parameter derived from FSO data and from thermal sensors based on sensor distance

buildings (derived from a two-month measuring period). A high influence on the fluctuation of the received optical signals can be observed from turbulences arising up to 8 m from the building. This is true especially during colder days, when the thermal heating of buildings radically changes the scintillation effects on a FSO link deployed in urban areas compared to links crossing free, non-built-up areas. Fig. 8 depicts the relationship between the turbulence and the FSO received signal expressed by a mean correlation coefficient from a two-month observation period calculated by (9).

## 5 Conclusion

The performance of free-space optical links is highly dependent on many limiting factors, particularly due to the time-variant properties of the transmitting medium. Temperature gradients within turbulent areas result in the bending or widening of transmitted optical beams. Analyses of the influence of turbulences on a free-space optical link in the vicinity of buildings were accomplished on the basis of a measurement campaign. The different dependences of the refractive index structure parameter were observed in the case of a FSO link deployed in an urban area compared to results published for links crossing free non-built-up areas. During the next stage of our research, data will be collected and analysed over a longer time period (several years) in order to obtain/derive a more precise description of the statistical characteristics of thermal influences.

## 6 Acknowledgments

This work was supported in part by the Czech Science Foundation under grant P102/10/1901 ‘Basic Research of Radiometeorology Properties of Tropospheric Ducting Layers by Using Artificial Intelligence Methods’. The measurements were supported by Czech Science Foundation grant 102/08/P346.

## 7 References

- 1 Bouchet, O.: ‘Free-space optics: propagation and communication’ (ISTE, 2006, 1st edn.)
- 2 Rec. ITU-R P.1814: ‘Prediction methods required for the design of terrestrial free-space optical links’, 2007
- 3 Prokes, A.: ‘Modeling of atmospheric turbulence effect on terrestrial FSO link’, *Radioengineering*, 2009, **18**, (1), pp. 42–47

- 4 Andrews, L.C., Phillips, R.L.: 'Laser beam propagation through random media' (SPIE Press, 2005, 2nd edn.), pp. 57–80
- 5 Al-Habash, A., Fischer, K.W., Cornish, C.S., Desmet, K.N., Nash, J.: 'Comparison between experimental and theoretical probability of fade for free space optical communications'. Proc. Conf. Optical Wireless Communications V, Boston, USA, August 2002, pp. 79–89
- 6 Niachou, K., Livada, I., Santamouris, M.: 'Experimental study of temperature and airflow distribution inside an urban street canyon during hot summer weather conditions – Part I: air and surface temperatures', *Build. Environ.*, 2008, **43**, (8), pp. 1383–1392
- 7 Andrews, L.C., Phillips, R.L., Hopen, C.Y.: 'Laser beam scintillation with applications' (SPIE Press, 2001, 1st edn.), pp. 86–92
- 8 Andrews, L.C.: 'Field guide to atmospheric optics' (SPIE Press, 2004, 1st edn.)
- 9 Miller, M., Zieske, P.L.: 'Turbulence environmental characterization'. RAD-TR-79-131, ADA072379, 1976 (Rome Air Development Center)
- 10 Kolmogorov, A.N.: 'The local structure of turbulence in incompressible viscous fluid for very large Reynolds numbers', *Doklady Akad. Nauk, S.S.S.R.*, 1941, **30**, pp. 301–305
- 11 Tang, X., Rajbhandari, S., Popoola, W.O., *et al.*: 'Performance of BPSK subcarrier intensity modulation free-space optical communications using a log-normal atmospheric turbulence model'. The Int. Symp. Photonics and Optoelectronics, Chengdu, China, June 2010, pp. 1–4
- 12 Samimi, H., Azmi, P.: 'Subcarrier intensity modulated free-space optical communications in K-distributed turbulence channels', *J. Opt. Commun. Netw.*, 2010, **2**, (8), pp. 625–632
- 13 Uysal, M., Li, J.T., Yu, M.: 'Error rate performance analysis of coded free-space optical links over gamma-gamma atmospheric turbulence channels', *IEEE Trans. Wirel. Commun.*, 2006, **5**, (6), pp. 1229–1233
- 14 Al-Habash, M.A., Andrews, L.C., Phillips, R.L.: 'Mathematical model for the irradiance probability density function of a laser beam propagating through turbulent media', *Opt. Eng.*, 2001, **40**, (8), pp. 1554–1562
- 15 Han, L., Wang, Q., Kutsunori, S.: 'Performance of free space optical communication through gamma-gamma turbulence channels with spatial diversity'. 2010 Int. Conf. Computer and Communication Technologies in Agriculture Engineering, Chengdu, China, 2010, pp. 109–112
- 16 Jurado-Navas, A., Garcia-Zambrana, A., Puerta-Notario, A.: 'Efficient lognormal channel model for turbulent FSO communications', *Electron. Lett.*, 2007, **43**, (3), pp. 178–180
- 17 Nistazakis, H.E., Karagianni, E.A., Tsigopoulos, A.D., Fafalios, M.E., Tombras, G.S.: 'Average capacity of optical wireless communication systems over atmospheric turbulence channels', *J. Lightwave Technol.*, 2009, **27**, (5–8), pp. 974–979
- 18 Khalighi, M.A., Aitamer, N., Schwartz, N., Bourennane, S.: 'Turbulence mitigation by aperture averaging in wireless optical systems'. Proc. 10th Int. Conf. Telecommunications Contel 2009, Zagreb, Croatia, June 2009, pp. 59–66
- 19 <http://freespaceoptics.ca>, accessed March 2010
- 20 [www.anemo.cz](http://www.anemo.cz), accessed February 2010
- 21 Ramachandran, K.M., Tsokos, C.P.: 'Mathematical statistics with applications' (Elsevier Academic Press, 2009, 1st edn.)
- 22 Dordova, L., Wilfert, O.: 'Volume of atmospheric turbulences evaluation on the basis of the turbulent area quantification'. Proc. 14th Conf. Microwave Techniques: Comite 2008, Prague, Czech Republic, April 2008, pp. 325–328
- 23 Diblik, J., Wilfert, O.: 'The influence of atmospheric turbulence on the rangefinder laser beam'. 15th Conf. Microwave Techniques, Brno, Czech Republic, April 2010, pp. 131–133
- 24 Zvanovec, S., Pechac, P.: 'Rain spatial classification for availability studies of point-to-multipoint systems', *IEEE Trans. Antennas Propag.*, 2006, **54**, (12), pp. 3789–3796
- 25 Colvero, C.P., Cordeiro, M.C.R., von der Weid, J.P.: 'FSO systems: rain, drizzle, fog and haze attenuation at different windows propagation'. SBMO/IEEE MTT-S Int. Microwave and Optoelectronics Conf., Salvador, Brazil, November 2007, pp. 563–568
- 26 Majumdar, A.K., Davis, C.C., (SPIE (Society): 'Free-space laser communications VIII: 10–12 August 2008, San Diego, California, USA' (SPIE, 2008, 1st edn.)
- 27 Giggenbach, D., Henniger, H., David, F.X.: 'Long-term near-ground optical scintillation measurements', in Cynthia, Y.Y., John, S.S. (Eds.): 'Atmospheric propagation – Proc. SPIE' (SPIE, 2003, vol. 4976, 1st edn.), pp. 132–140
- 28 Henniger, H., Epple, B., Haan, H.: 'Maritime mobile optical-propagation channel measurements'. IEEE Int. Conf. Communications, Cape Town, South Africa, May 2010, pp. 1–5
- 29 Jumper, G.Y., Vermin, J., Azoit, M., Trinquet, H.: 'Comparison of recent measurements of atmospheric optical turbulence'. 36th Plasmadynamics and Lasers Conf., Toronto, Ontario, June 2005, pp. 1–12

common edge of an RWG triangle pair. The benefits of the basis function include the approximate orthogonality to the RWG basis function, the association with the RWG basis function, the constant charge density within each polygon, the vanishing charges within a polygon pair and no fictitious line charges across polygon boundaries. When used with the RWG basis function together to represent the magnetic current and electric current, respectively, the resultant system matrix is naturally well-conditioned with a simple testing scheme. This is because each operator in the SIEs is well tested and the system matrix is diagonally dominant. The good conditioning of the system matrix is very desirable in fast algorithms because they use iterative methods to solve the matrix equations and the convergence strongly relies on the conditioning. We implement the above dual basis function with the partnership of RWG basis function in the MoM and the process is accelerated with the MLFMA for solving the SIEs with penetrable media. Numerical examples for scattering by large composite objects are presented to demonstrate the scheme and fast convergence of solutions can be observed.

## REFERENCES

- [1] W. C. Chew, M. S. Tong, and B. Hu, *Integral Equation Methods for Electromagnetic and Elastic Waves*. San Rafael, CA: Morgan & Claypool, 2008.
- [2] E. K. Miller, L. Medgyesi-Mitschang, and E. H. Newman, *Computational Electromagnetics: Frequency-Domain Method of Moments*. New York: IEEE Press, 1992.
- [3] S. M. Rao, D. R. Wilton, and A. W. Glisson, "Electromagnetic scattering by surfaces of arbitrary shape," *IEEE Trans. Antennas Propag.*, vol. AP-30, no. 3, pp. 409–418, Mar. 1982.
- [4] S. M. Rao and D. R. Wilton, "E-field, H-field and combined field solution for arbitrarily shaped three-dimensional dielectric bodies," *Electromagn.*, vol. 10, no. 4, pp. 407–421, Oct. 1990.
- [5] Q. L. Chen, "Electromagnetic modeling of three-dimensional piecewise homogeneous material bodies of arbitrary composition and geometry," Ph.D. dissertation, Univ. Houston, TX, 1990.
- [6] A. Buffa and S. H. Christiansen, "A dual finite element complex on the barycentric refinement," *Math. Comput.*, vol. 76, no. 260, pp. 1743–1769, Oct. 2007.
- [7] F. P. Andriulli, K. Cools, H. Bagci, F. Olyslager, A. Buffa, S. Christiansen, and E. Michielssen, "A multiplicative Calderón preconditioner for the electric field integral equation," *IEEE Trans. Antennas Propag.*, vol. 56, no. 8, pp. 2398–2412, Aug. 2008.
- [8] J. Board and K. Schulten, "The fast multipole algorithm," *IEEE Comput. Sci. Eng.*, vol. 2, no. 1, pp. 76–79, Jan./Feb. 2000.
- [9] W. C. Chew, J. M. Jin, E. Michielssen, and J. M. Song, *Fast and Efficient Algorithms in Computational Electromagnetics*. Boston: Artech House, 2001.
- [10] Ö. Ergül and L. Gürel, "Rigorous solutions of electromagnetics problems involving hundreds of millions of unknowns," *IEEE Antennas Propag. Mag.*, Jun. 2010.
- [11] K. Sertel and J. L. Volakis, "Incomplete LU preconditioner for FMM implementation," *Microw. Opt. Tech. Lett.*, vol. 26, no. 4, pp. 265–267, Aug. 2000.
- [12] J. Lee, J. Zhang, and C.-C. Lu, "Sparse inverse preconditioning of multilevel fast multipole algorithm for hybrid integral equations in electromagnetics," *IEEE Trans. Antennas Propag.*, vol. 52, no. 9, pp. 2277–2287, Sep. 2004.
- [13] B. Carpentieri, I. S. Duff, L. Giraud, and G. Sylvand, "Combining fast multipole techniques and an approximate inverse preconditioner for large electromagnetism calculations," *SIAM J. Sci. Comput.*, vol. 27, no. 3, pp. 774–792, Nov. 2005.
- [14] T. Malas and L. Gürel, "Incomplete LU preconditioning with the multilevel fast multipole algorithm for electromagnetic scattering," *SIAM J. Sci. Comput.*, vol. 29, no. 4, pp. 1476–1494, Jun. 2007.
- [15] B. M. Kolundzija, "Electromagnetic modeling of composite metallic and dielectric structures," *IEEE Trans. Microw. Theory Tech.*, vol. 47, no. 7, pp. 1021–1032, Jul. 1999.
- [16] M. S. Tong, W. C. Chew, B. J. Rubin, J. D. Morsey, and L. Jiang, "On the dual basis for solving electromagnetic surface integral equations," *IEEE Trans. Antennas Propag.*, vol. 57, no. 10, pp. 3136–3146, Oct. 2009.
- [17] X. Q. Sheng, J. M. Jin, J. M. Song, W. C. Chew, and C. C. Lu, "Solution of combined-field integral equation using multilevel fast multipole algorithm for scattering by homogeneous bodies," *IEEE Trans. Antennas Propag.*, vol. 46, no. 11, pp. 1718–1726, Nov. 1998.
- [18] M. S. Tong and W. C. Chew, "A higher-order Nyström scheme for electromagnetic scattering by arbitrarily shaped surfaces," *IEEE Antennas Wireless Propag. Lett.*, vol. 4, pp. 277–280, 2005.
- [19] G. T. Ruck, D. E. Barrick, W. D. Stuart, and C. K. Krichbaum, *Radar Cross Section Handbook*. New York: Plenum Press, 1970.

## Validation of Rain Spatial Classification for High Altitude Platform Systems

Stanislav Zvanovec and Pavel Pechac

**Abstract**—Previous work on rain spatial classification for terrestrial PMP radio systems has been extended in this communication to stratospheric systems—high altitude platform systems. It was found that the rain spatial parameter concept can also be effectively applied to HAP systems, although specific adjustments have had to be made to the method. The differences between terrestrial and stratospheric systems are discussed with regard to the new derived dependences.

**Index Terms**—Diversity methods, millimeter wave propagation, rain.

## I. INTRODUCTION

High altitude platforms (HAP), also known as stratospheric repeaters/systems [1], could offer the possibility of very fast additional coverage or could be utilized as an alternative to satellite or terrestrial systems. Broadband reliable transmissions in the millimeter waveband are also envisaged [2], therefore the influence of rain on propagated electromagnetic waves is of a great importance for system planning. Among other factors, rain spatial properties and the corresponding fade mitigation techniques, e.g., route diversity schemes, should be considered. The route diversity given by the recommendation ITU-R P. 618 [3] for satellite links cannot be accurately applied, since the link geometry is different in the case of HAP systems.

Rather than analyzing only two HAP link joint statistics (e.g., elaborately studied in [4]), many simultaneous diversity links representing overall system performance were tested under specific conditions, both in time and space, within a defined area. The methodology and a rain spatial classification method relevant to rainfall influence on terrestrial PMP radio systems were proposed in [5]. This communication extends this work (briefly summarized in Section II) to the specific case of stratospheric systems. Based on extensive simulations, the method is

Manuscript received February 24, 2010; revised November 02, 2010; accepted December 10, 2010. Date of publication May 10, 2011; date of current version July 07, 2011. This work was supported by Czech Science Foundation Grant 102/08/P346 and research project no. OC09075 of the Czech Ministry of Education, Youth and Sports.

The authors are members of the Department of Electromagnetic Field, Czech Technical University in Prague, Czech Republic (e-mail: xzvanove@fel.cvut.cz; pechac@fel.cvut.cz).

Color versions of one or more of the figures in this communication are available online at <http://ieeexplore.ieee.org>.

Digital Object Identifier 10.1109/TAP.2011.2152325

validated for a HAP network and particular adjustments of the method are proposed.

## II. APPROACH USED FOR TERRESTRIAL SYSTEMS

To validate HAP systems, the approach to rain spatial classification for terrestrial systems [5] was utilized. It is based on an enumeration of the outage improvement probability  $P$  defined as a percentage of terminal stations with a successfully established diversity link (i.e., with received power  $P_{P_{div}}$  higher than the threshold  $P_{P_{threshold}}$ ) throughout the network from  $n_{out}$  links having a received power level  $P_{P_{main}}$  below the threshold due to rain attenuation

$$P = \frac{\sum_1^{n_{out}} (P_{P_{div}} > P_{P_{threshold}})}{n_{out}} \cdot 100 \quad (1)$$

$$n_{out} = \sum (P_{P_{main}} < P_{P_{threshold}}). \quad (2)$$

In the case of terrestrial systems, the outage improvement was derived as a function of angular separation  $\vartheta$  (rad) and the ratio of the main and diversity link lengths  $d_{main}/d_{div}$  [5]

$$P = a_{const} \cdot \left( 1 - \left( \frac{\vartheta - \pi}{\pi - b_{const} \sqrt{1 - \frac{d_{main}}{d_{div}}}} \right)^2 \right) \cdot \left( \frac{d_{main}}{d_{div}} \right)^{c_{const}}. \quad (3)$$

An empirical parameter  $a_{const}$  is dependent on the maximum rain rate  $R_{MAX}$  taken from the whole rainfall radar scan and on the rain fade margin  $P_{MARG}$  set in the system as [5]

$$a_{const} = a_1 + a_2 \cdot P_{MARG} - R_{MAX} \quad (4)$$

where  $a_1 = 110.64$  and  $a_2 = 2.14$  were derived for terrestrial systems from the radar and simulated data.

The other coefficients,  $b_{const}$  and  $c_{const}$ , are then highly dependent on the rate spatial distribution described by the rain spatial parameter  $S$  in  $\text{km}^2$  as [5]

$$c_{const} = S^{c_1} \cdot (1 - \exp(-c_1 \cdot S)) \quad (5)$$

$$b_{const} = \pi/4 - \exp(b_1 \cdot c_{const}) \quad (6)$$

with  $c_1 = 0.12$ , and  $b_1 = 1.38$  obtained by a curve fitting algorithm. The rainfall spatial parameter is able to characterize the spatial properties of the rain event in terms of rain cell sizes and rain rate slopes, relating to their impact on the point-to-multipoint terrestrial system within a given area [5]. It is calculated by normalizing a particular rain rate spatial distribution by its maximum rain rate and then by dividing it into 9 contour levels; then, by averaging areas of the rain cell for each contour threshold and subsequently, by taking the mean value of the average rain cell areas for all contour levels [5].

## III. STATISTICS AND MODELING FOR HAP SYSTEMS

An analysis of a hypothetical HAP system was performed based on meteoradar scans for the Czech Republic for the period from 2002–2005 [6]. During simulations, the influence of the outage improvement probability on the rain fade margin constant within the whole system (set from 5 to 30 dB) was tested at a frequency of 48 GHz (chosen in accordance with [1]). Contrary to terrestrial system simulations [5], where a linear polarized electromagnetic wave was

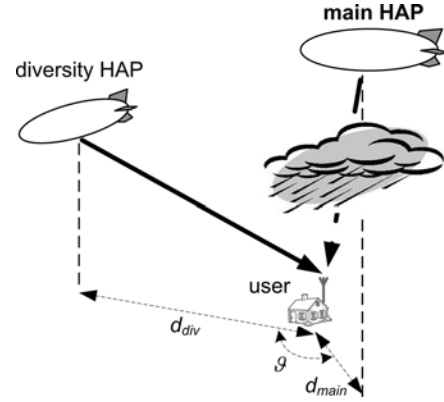


Fig. 1. Scenario of HAP diversity.

considered, a circular polarization was set up in the case of HAP links [2].

The main focus was to derive corresponding relations among rain event parameters and the availability of HAP systems independently of the particular deployment of HAP stations and spatial distribution of users. Therefore for particular rain distribution, the user was moved step-by-step in a 1 km raster and at each position the likelihood that the connection to a HAP station (situated in an altitude of 20 km; land distances from 2 to 20 km and all azimuths) would be significantly affected by rain was investigated. In the case the rain loss exceeded the rain fade margin, an additional diversity link with a second HAP station (having lengths of up to 20 km) was tested for all angular separations. See the diversity scenario considered for HAP systems in Fig. 1.

In the next step, the dependences of the parameters  $a_{const}$ ,  $b_{const}$  and  $c_{const}$  were derived from the obtained set of probabilities of outage reductions within HAP systems by use of genetic algorithms.

Even though simulations of HAP systems again resulted in a linear dependence of  $a_{const}$  on  $R_{MAX}$  and  $P_{MARG}$  as in [5], the relations denoting the influence of the maximum rain rate—especially the slope of this dependence—have to be described differently with respect to the rain fade margins. It was observed that the value of the rain fade margin parameterizes  $a_{const}$  dependence on the maximum rain rate. A new derived relationship valid for HAP systems can be expressed by

$$a_{const} = a_1 + \frac{1}{a_1} \cdot P_{MARG} R_{MAX} + a_2 R_{MAX} - P_{MARG}. \quad (7)$$

The constants  $a_1 = 50.16$  and  $a_2 = -0.454$  were obtained by regressive fitting of the simulated data. Examples demonstrating results from simulations and a fitting by the new relation for rain fade margins of 10 dB and 20 dB can be seen in Fig. 2.

The influence of the rain spatial distribution on the outage improvement probability was analyzed for HAP systems with a route diversity scheme. From the simulations performed, the resulting dependence of  $c_{const}$  on rain spatial parameter was determined in the form of

$$c_{const} = (c_2 \cdot S)^{c_1} - c_2^{-1}. \quad (8)$$

The parameters  $c_1$  and  $c_2$  in (8) were optimized using genetic algorithms to the values of  $c_1 = 0.309$  and  $c_2 = 0.520$ , respectively.

The dependence of the last empirical parameter,  $b_{const}$ , on the parameter  $c_{const}$  obtained from the simulation of HAP systems is depicted in Fig. 3.

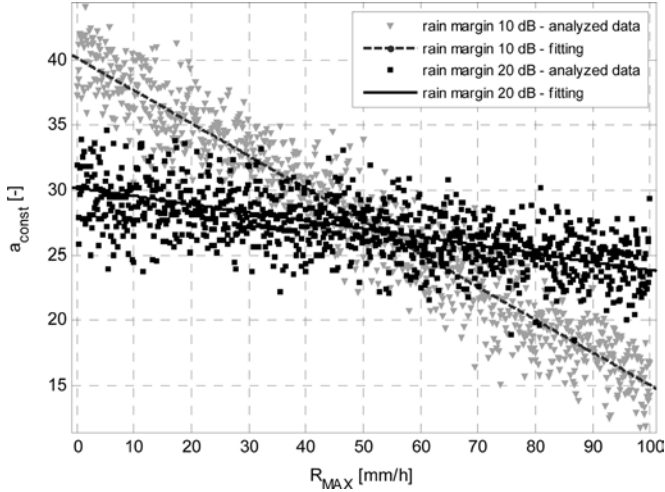


Fig. 2. The dependence of the parameter  $a_{\text{const}}$  on the maximum rain rate within the particular area and on rain fade margins of 10 dB and 20 dB.

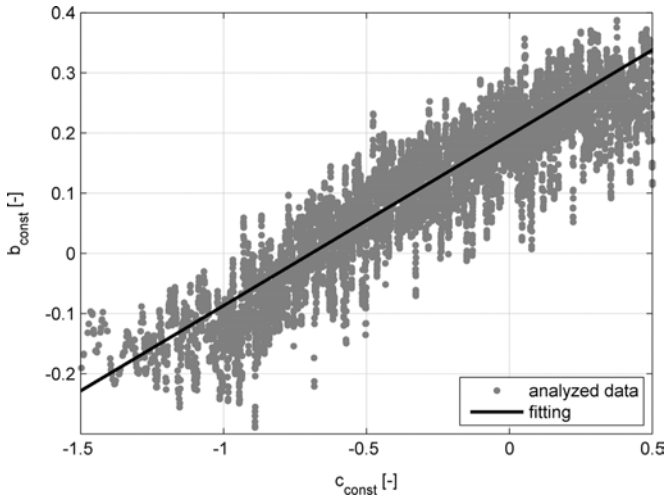


Fig. 3. The dependence of the parameter  $b_{\text{const}}$  on parameter  $c_{\text{const}}$  for HAP systems.

The derived dependence for HAP systems has a linear increase and can be expressed as

$$b_{\text{const}} = b_1 \cdot c_{\text{const}} + b_2 \quad (9)$$

where  $b_1 = 0.283$  and  $b_2 = \pi/16$ . It should be mentioned that these statistics were generated for the region of the Czech Republic. The rainfall spatial parameter can be applied in general to any climatic regions but its definition would have to be based on appropriate experimental data using the same methodology.

#### IV. COMPARISON OF HAP AND TERRESTRIAL SYSTEM PERFORMANCES

In this point, it is useful to demonstrate the similarities and differences between HAP and terrestrial systems based on the simulation results. Knowledge of two basic types of rainfall is essential for a detailed understanding of the simulation results. The first type, stratiform rain, is usually spread over large areas and can be characterized by the slow decay of the low rain rate from its maximum (which is usually less than 10 mm/h). The second type, convective rain, represents smaller heavy

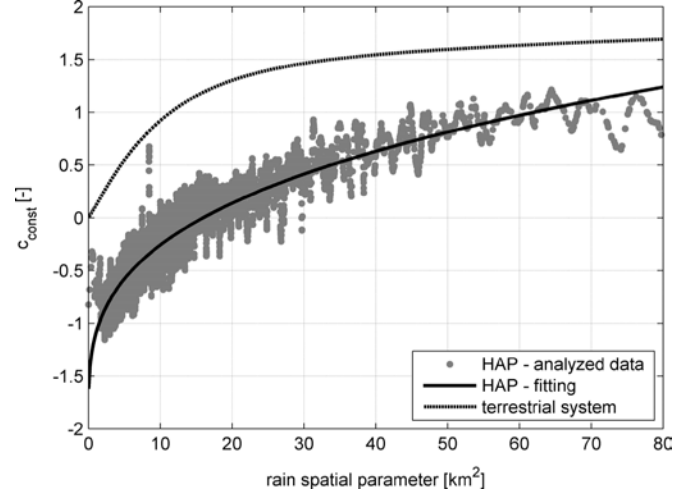


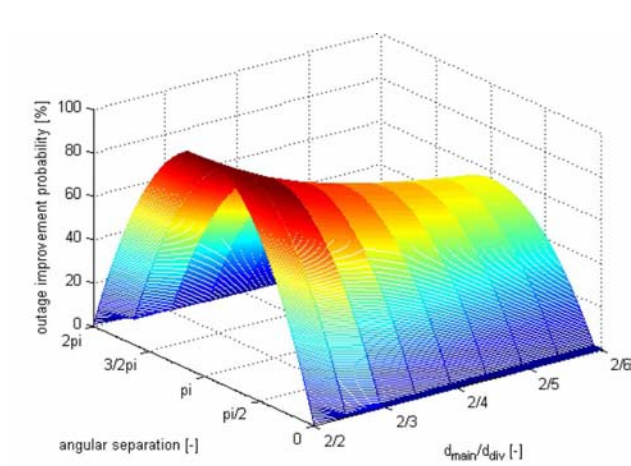
Fig. 4. A comparison of dependences of the parameter  $c_{\text{const}}$  on the rain spatial parameter derived for HAP and terrestrial systems.

rain cells with high rain intensity. From a physical point of view, wide spread stratiform rainfalls result in a lower number of millimeter link drops, unlike convective rains which cause high numbers of system outages. Nevertheless, since convective rains are spread over a smaller area, they can be over-traced by HAP links. Note that, according to [7], the mean height of the rain is equal to 3.36 km above mean sea level (figures valid for central Europe). In the case of terrestrial systems, a higher percentage of links can cross the rainy area even in the cases when the diversity base station is not directly affected by rain and therefore different outage improvement probabilities can be observed.

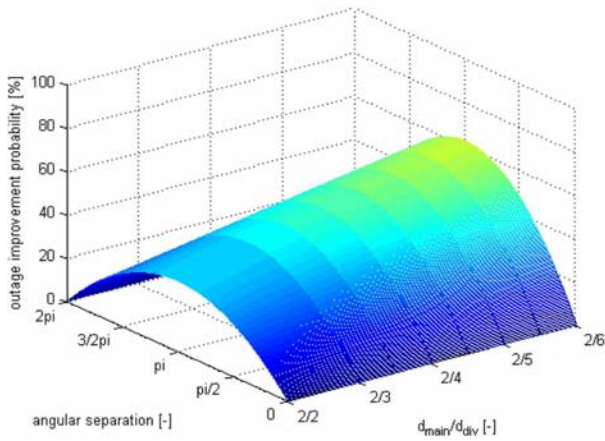
A remarkable difference in the utilization of route diversity within both systems can be observed when changing the main to diversity link length ratio. A constant length of the main link and an increasing length of the diversity link lead to a decrease in the outage improvement probability in the case of terrestrial systems, unlike HAP systems, where the outage improvement probability increases under specific conditions. The parameter  $c_{\text{const}}$ , determining a value of the power of the main and diversity link lengths ratio in (3) is a vital measure, particularly in this case. A comparison of dependences of the parameter  $c_{\text{const}}$  on the rain spatial parameter for HAP systems and for terrestrial point-to-multipoint systems is illustrated in Fig. 4.

In the case of both systems, the parameter  $c_{\text{const}}$  increases with the increasing rain spatial parameter. Note that for HAP systems, the  $c_{\text{const}}$  parameter reaches negative values for the low rain spatial parameter. Therefore, in the case of the rain spatial parameter below  $15.8 \text{ km}^2$ , with an increasing length of the diversity HAP link an increase of the outage improvement probability, caused by the negative value of the parameter  $c_{\text{const}}$ , can be observed. This distinction can be explained by a difference between link configurations, when majority parts of terrestrial links are affected by the rain event and the lengthening of diversity links does not significantly improve rain losses. HAP links are, on the other side, only influenced below rain heights, which leads to better system performance in the case of a low rain spatial parameter.

The mentioned features of both systems are demonstrated in Figs. 5 and 6. Two rain distributions with the maximum rain rate of 30 mm/h were chosen as an example to show differences between terrestrial and HAP systems. First a rain distribution with the rain spatial parameter less than the mentioned threshold of  $15.8 \text{ km}^2$  ( $S = 5 \text{ km}^2$ )—see the outage improvement probabilities in Fig. 5—and the second rain distribution with  $S = 40 \text{ km}^2$ —demonstrated in Fig. 6. Rain fade margins of 10 dB were considered during the simulations.



a)

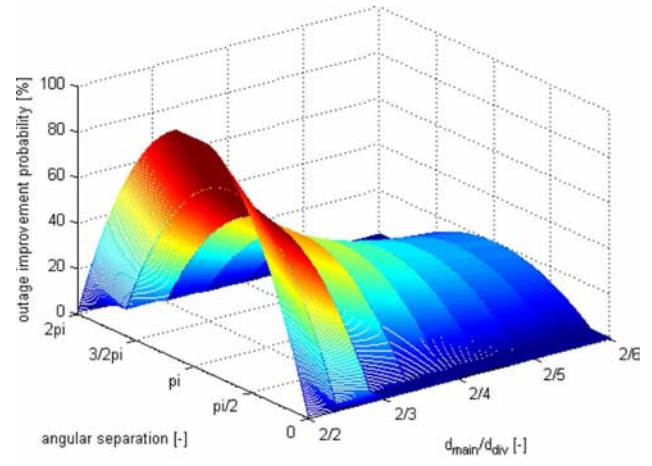


b)

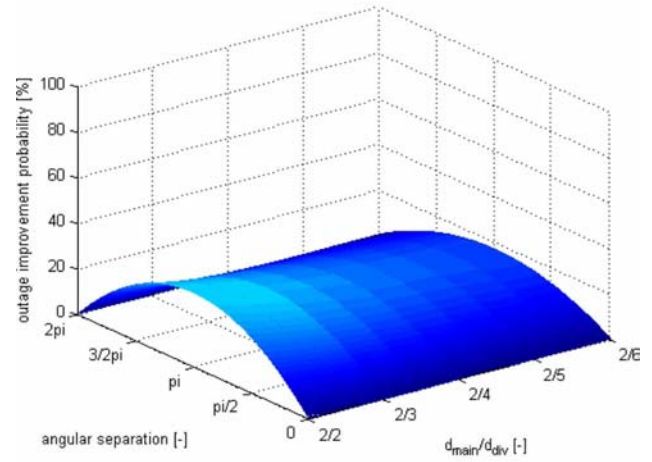
Fig. 5. A dependence of the outage improvement probability for rain distribution with  $S = 5 \text{ km}^2$ ,  $R_{\text{MAX}} = 30 \text{ mm/h}$  for (a) a terrestrial system, (b) a HAP system, both with  $P_{\text{MARG}} = 10 \text{ dB}$ .

The rain spatial parameter has also a different influence through the parameter  $c_{\text{const}}$  on the angular separation dependence of the outage improvement probabilities in the case of HAP systems than was observed in the case of terrestrial systems [5]. From a physical point of view this can be explained by the section of link crossing a rainy area. For angular separations between links of up to 57 degrees, rain distributions along HAP link sections of the main and diversity links are highly correlated (note, the angular limit was empirically derived for correlation coefficients exceeding 0.7), having close maximum rain rates. This means, that utilization of route diversity is not as efficient for the same link angular separations as in the case of terrestrial systems, where such a high correlation between rain distributions along paths was not determined. Therefore essentially higher changes in the outage improvement probability can be observed for these systems.

An overall decrease in the dependence of the outage improvement probability on the maximum rain rate was observed in HAP systems for users employing the route diversity when compared to terrestrial systems [5]. For instance for users with similar lengths of main and diversity links and a particular rain fade margins set, the utilization of route diversity in a HAP network reaches approximately one-third of the values determined in the case of terrestrial systems [5]. This can be explained by the fact that the path affected by rain is generally shorter in the case of HAP links at high elevation angles.



a)



b)

Fig. 6. The dependence of the outage improvement probability for rain distribution with  $S = 40 \text{ km}^2$ ,  $R_{\text{MAX}} = 30 \text{ mm/h}$  for (a) a terrestrial system and (b) a HAP system, both with  $P_{\text{MARG}} = 10 \text{ dB}$ .

From the analyses performed, it can nevertheless be concluded that the rain spatial parameter concept can be very well adapted for use on HAP systems. The resulting equation for the outage improvement probability in the case of a HAP system with route diversity has to be expressed in the new form

$$P = a_{\text{const}} \cdot \left( 1 - \left( \frac{\vartheta - \pi}{\pi - \left( \frac{\pi + 4.5 \cdot c_{\text{const}}}{16} \right) \sqrt{1 - \frac{d_{\text{main}}}{d_{\text{div}}}}} \right)^2 \right) \cdot \left( \frac{d_{\text{main}}}{d_{\text{div}}} \right)^{c_{\text{const}}} \quad (10)$$

## V. CONCLUSION

Based on the results of the analyses presented in the communication, it can be concluded that the method of rain spatial classification for the evaluation of rain influences on terrestrial systems can also be adapted for HAP systems. It was derived that both approaches are quite distinctively dependent on the rain spatial parameter. This can be explained by different link geometries and system deployments.

Furthermore, different dependences of HAP system performances on the variability of maximum rain rates within the areas served and

on the rain fade margins set in systems compared to terrestrial systems were observed and discussed in the communication.

#### REFERENCES

- [1] "Preferred Characteristics of Systems in the Fixed Service Using High-Altitude Platform Stations Operating in the Bands 47.2–47.5 GHz an 47.9–48.2 GHz," 2000, ITU-R Recommendation F.1500.
- [2] C. Spillard, E. Falletti, J. D. Penin, J. L. Ruíz-Cuevas, and M. Mondin, "Mobile Link Propagation Aspects, Channel Model and Impairment Mitigation Techniques," FP6 IST-2003-506745 CAPANINA, 2004 [Online]. Available: <http://www.capanina.org/deliverables.php>, Deliverable D14
- [3] "Propagation Data and Prediction Methods Required for the Design of Earth-Space Telecommunication Systems," 2009, International Telecommunications Union, ITU-R Recommendation P.618-10.
- [4] A. D. Panagopoulos, E. M. Georgiadou, and J. D. Kanellopoulos, "Selection combining site diversity performance in high altitude platform networks," *IEEE Commun. Lett.*, vol. 11, no. 10, pp. 787–789, 2007.
- [5] S. Zvanovec and P. Pechac, "Rain spatial classification for availability studies of point-to-multipoint systems," *IEEE Trans. Antennas Propag.*, vol. 54, no. 12, pp. 3789–3796, 2006.
- [6] Z. Sokol, "The use of radar and gauge measurements to estimate areal precipitation for several Czech river basins," *Stud. Geophys. Geod.*, no. 47, pp. 587–604, 2003.
- [7] "Rain Height Model for Prediction Methods," 2001, International Telecommunications Union, ITU-R Recommendation P.839-3.

**TABLE 2 Features and Performances of the Push-Push DROs**

Refereces	[1]	[2]	[3]	[4]	This Work
Features	SiGe HBT, Hybrid	HEMT, LTCC	FET, Hybrid	FET, Hybrid	SiGe HBT, Hybrid
Frequency (GHz)	58	16	12	22	12.4
Power (dBm)	-14	0.5	>10	6	9.5
Phase noise (dBc/Hz) @at 100 kHz	-86	-103	-110	-114	-120.2
$f_0$ suppression (dBc)	17	30	27	>30	32.5

signal injection condition. As the temperature coefficient of the DR is about 2 ppm/°C, the maximum frequency drift during 0–50°C temperature range will be 1.24 MHz, corresponding to 2.48 MHz at the second harmonic. According to Figure 11, an injection power of 6 dBm is high enough for most common applications.

Figure 12 shows the output power characteristics near 12.4 GHz with an injection power of 10 dBm. It can be seen that the output power is flat in the locking range, and the upper and the lower locking range is symmetry. Table 1 shows the fundamental suppressions of the in-phase and the out-of-phase methods. Obviously, the fundamental suppression for out-of-phase method is higher than its in-phase counterpart. This result also validates the analysis presented in Section 3.

Table 2 summarizes the features and performances of several free running push–push DROs reported in recent years. It can be seen that this design exhibits high fundamental suppression and low phase noise. If very low phase noise signal is injected, the phase noise of the oscillator can be further improved.

## 5. CONCLUSIONS

An X-band push–push DRO with injection locking capability is implemented. The oscillator works near 12.4 GHz with 9.5 dBm output power. The fundamental suppression is about 32.5 dBc without using bandpass filter. The phase noise values of the free running oscillator are -104.4 dBc/Hz, -120.2 dBc/Hz, and -142.6 dBc/Hz at 10 kHz, 100 kHz, and 1 MHz offset frequencies from the carrier frequency, respectively. This phase noise performance is superior or comparable to recently reported results. Two injection locking methods, i.e., the in-phase injection locking and the out-of-phase injection locking are studied. Theoretical analysis and experimental results indicate that the out-of-phase method has higher fundamental suppression and wider locking range than the in-phase method. The proposed design is also applicable to millimeter-wave injection-locked push–push DROs.

## REFERENCES

1. F.X. Sinnesbichler, B. Hautz, and G.R. Olbrich, Si/SiGe HBT dielectric resonator push–push oscillator at 58 GHz, *IEEE Microwave Guided Wave Lett* 10 (2000), 145–147.
2. B. Yom, D.H. Shin, S.H. Oh, and K.K. Ryu, Push–push voltage controlled dielectric resonator oscillator using a LTCC technology, *Microwave Opt Technol Lett* 49 (2001), 1824–1827.
3. J.F. Gravel and J.S. Wight, On the conception and analysis of a 12-GHz push–push phase-locked DRO, *IEEE Trans Microwave Theory Tech* 54 (2006), 153–159.
4. H.Y. Chang, H. Wang, Y.C. Wang, P.C. Chao, and C.H. Chen, A 22-GHz ultra low phase noise push–push dielectric resonator oscillator using MMICs, *Proceedings of the 12th GaAs Symposium*, vol. 10, 2004, pp. 33–36.

5. U.L. Rohde, A.K. Poddar, and G. Böck, *The design of modern microwave oscillators for wireless application—Theory and optimization*, Wiley, New York, 2005.
6. K. Kawahata, T. Tanaka, and M. Aikawa, K-Band subharmonic injection-locked push–push oscillator using double-sided MIC, *Electron Commun Jpn* 88 (2005), 1–9.
7. T.P. Wang, Z.M. Tsai, K.J. Sun, and H. Wang, Phase-noise reduction of X-band push–push oscillator with second-harmonic self-injection techniques, *IEEE Trans Microwave Theory Tech* 55 (2007), 66–77.
8. G. Gonzalez, *Foundations of oscillator circuit design*, Artech House, Boston, 2007.

© 2010 Wiley Periodicals, Inc.

## SINGLE-SHOT ALL-OPTICAL SAMPLING OSCILLOSCOPE USING A POLARIZATION-MAINTAINING RESONATOR FOR PULSE REPLICATION

Komanec Matěj,<sup>1</sup> Honzátko Pavel,<sup>2</sup> and Zvánovec Stanislav<sup>1</sup>

<sup>1</sup>Faculty of Electrical Engineering, Department of Electromagnetic Field, Czech Technical University in Prague, Technická 2, 166 27 Prague 6, Czech Republic; Corresponding author: komanmat@fel.cvut.cz

<sup>2</sup>Institute of Photonics and Electronics, Chaberská 57, 182 51 Prague, Czech Republic

Received 5 February 2010

**ABSTRACT:** An all-optical single-shot sampling oscilloscope with a picosecond resolution is developed. An innovative approach for data pulse replication using a polarization-maintaining resonator is used. Pulses are sampled in a highly nonlinear fiber. Acquired data are used for pulse shape reconstruction. Proposed setup eliminates the need of a delay line. © 2010 Wiley Periodicals, Inc. *Microwave Opt Technol Lett* 52:2452–2456, 2010; View this article online at [wileyonlinelibrary.com](http://wileyonlinelibrary.com). DOI 10.1002/mop.25509

**Key words:** optical sampling oscilloscope; four-wave mixing; highly nonlinear fiber; fiber pulse replicator

## 1. INTRODUCTION

All-optical sampling introduces a method of eye diagram monitoring that provides a valuable signal quality measurement [1]. More specifically, optical sampling enables measuring of high bit rate signals, in the case where optoelectronic sampling devices have already reached their limits, e.g., 320 Gbit/s, 640 Gbit/s in experimental optical networks.

A typical all-optical sampling oscilloscope consists of a resonator or a delay line and a sampler [2]. The purpose of including the resonator (delay line) into the oscilloscope is to replicate incoming data pulses to allow sampling and detection at lower frequencies. Using this approach, replicated pulses can be afterwards better processed by subsequent photonic detectors and optoelectronic circuits. The sampler is in most cases based on a nonlinear phenomenon, such as cross-phase modulation (XPM) or four-wave mixing (FWM).

Main difference can be found in processing of random pulses or periodic signals. For repetitive (periodic) signals, the need of a delay line (resonator) is redundant, because it is possible to sample the data at low frequency in this case. After acquiring sufficient amount of samples, the reconstruction of the incoming signal is possible. Various methods for repetitive optical signals (waveforms) analysis have been proposed. Sampling of return-to-zero data stream at 640 Gbit/s was demonstrated by Westlund

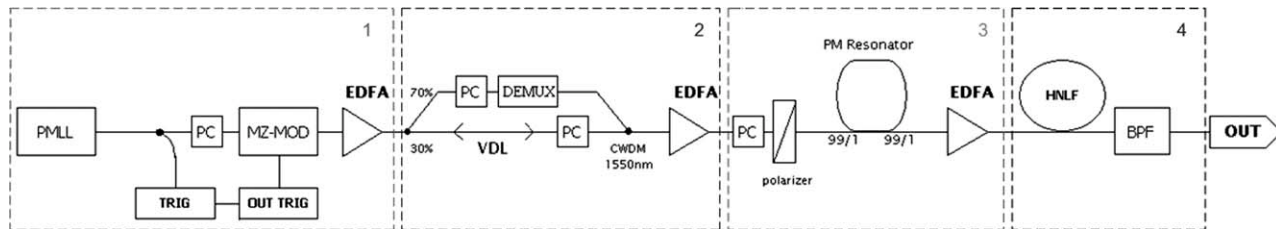


**Figure 1** Experimental setup for data sampling a pulse replicator and highly nonlinear fiber

and coworker [3], who also presented the software-synchronized all-optical technique that does not require clock recovery [4].

When a nonrepetitive signal is measured, a single-shot technique should be used. This approach still brings many challenges even though the first single-shot sampling based on time domain multiplexing was presented as early as 1998 by Deng et al. [2]. A high-dynamic-range single-shot cross-correlator based on pulse replicator was proposed by Dorrer et al. [5].

In this article, a development of a single-shot all-optical sampling oscilloscope using a fiber pulse replicator and a sampler based on FWM is introduced. The paper is organized using the following pattern: at first an experimental setup is demonstrated, where partial components and their functionality are discussed more in detail. In the following subsection, examples of reached results and their processing are demonstrated. The article concludes with a brief summary including main features and suggestions of additional improvement.

## 2. EXPERIMENTAL SETUP AND DATA PROCESSING

The proposed experimental setup (presented in Fig. 1) can be divided into four main parts. A femto second passively-mode locked laser in the first part serves as a signal source. The externally triggered Mach-Zender modulator allows to “pick” desired pulses from the generated pulse train. A polarization controller (PC) is used to properly set the state of polarization at the input of the modulator. The erbium-doped fiber amplifier (EDFA) is placed before the second part to ensure desired signal level.

The second part of the proposed experimental setup serves for signal pair creation. Here the real situation, where the sampling signal has to be derived from the incoming data signal, is replaced by direct generation by an optical filter. The signal pair is created by a coarse wavelength demultiplexer (CWDM) and a demultiplexer. An adjustable air gap, i.e., a variable delay line

(VDL) is an essential component of this part, used for adjusting an initial time delay between the sampling signal and the data signal before their input into the resonator. Zero difference in time of the signal-pair should be achieved at the input of the resonator.

Analyzed spectrum of the signal-pair both without and with a CWDM, cutting the spectrum at 1563 nm is presented in Figures 2(a) and 2(b), respectively. From the signal spectrum and autocorrelations of the signal-pair the full-width-at-half-maximum (FWHM) of pulses and consequently the time-bandwidth product are obtained to ensure that pulses are Fourier-transform limited.

A polarizer and a polarization controller ensure polarization along the principal axis of the polarization-maintaining (PM) fiber at the input of the third part. Signal is then led into the resonator, which is accounted the vital part of the single-shot sampling oscilloscope. The resonator is made of two PM Y-couplers with a coupling ratio of 99/1. The high coupling ratio was chosen due to the fact that maximum power should be preserved in the loop to acquire as many data pulse replicas as possible. Y-couplers also prove to be extremely efficient at splicing light with a small loss.

They provide a higher round-trip loss, but on the other hand they ensure almost the same magnitude of the sampling and the replicated pulse from the pulse-pair sent into the resonator. Measured attenuation of the loop is demonstrated in Figure 3. An amplifier is added at the output to compensate high losses induced by the two couplers.

The main advantage of the resonator is its capability to replicate data signal pulses together with sampling pulses while inserting a walk-off between the pulse-pair. The data pulse and the sampling pulse walk-off in the resonator is governed by

$$\Delta T = DL_R \Delta \lambda, \quad (1)$$

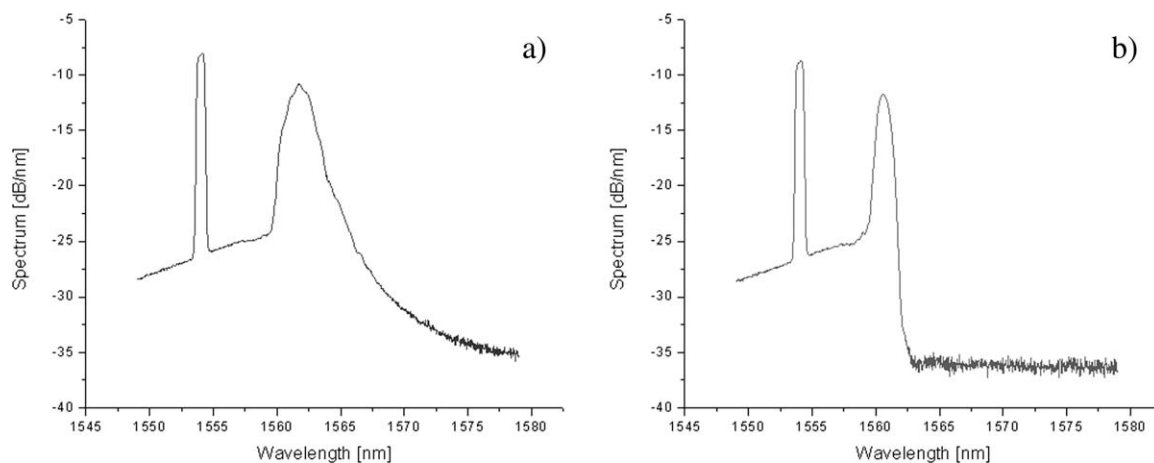


**Figure 2** Measured spectrum of the sampling and data signal, (a) without; (b) with a CWDM cutting the spectrum at 1563 nm

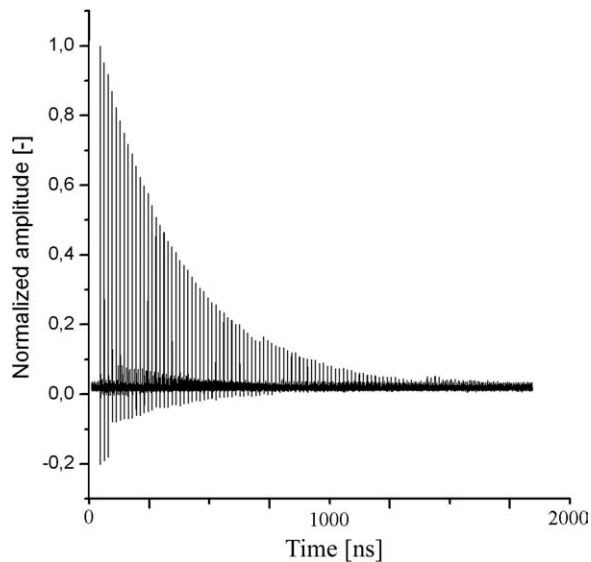


**Figure 3** Measured data pulses at the output of the PM resonator

where  $D$  introduces dispersion coefficient,  $L_R$  stands for resonator length of the loop and  $\Delta\lambda$  is the wavelength difference between the data and the sampling pulse. From this equation stems the fact, that by tuning the wavelength, it is possible to achieve the desired round-trip walk-off. The sampling pulse

must have its FWHM significantly lower than FWHM of the data pulse to acquire enough samples for further signal reconstruction. Thanks to different wavelengths of the pulse pair, each pulse experiences different chromatic dispersion and the sampling pulse travels continuously in time with each loop through the data pulse.

Finally the sampling takes place in a highly nonlinear fiber (HNLF) via the FWM effect and by a set of filters the sampled signal is obtained.

The acquired samples can be mathematically determined as

$$|A_{\text{sampled}(i)}(L)|^2 = \left| \frac{i\gamma P_{\text{sampling}(i)}}{g \sinh(gL)} \right|^2 |A_{\text{data}(i)}(0)|^2, \quad (2)$$

where  $A_{\text{sampled}(i)}$  stands for the amplitude of the  $i$ th pulse sample,  $P_{\text{sampling}(i)}$  is the power of the  $i$ th sampling pulse,  $A_{\text{data}(i)}$  introduces the amplitude of the  $i$ th data pulse,  $\gamma$  is the nonlinear coefficient of the fiber and the gain coefficient  $g$  can be defined in accordance with [6] as:

$$g^2 = (\gamma P_{\text{sampling}(i)})^2 - \left(\frac{\kappa}{2}\right)^2, \quad (3)$$

$$\kappa = 2\gamma P_{\text{sampling}(i)} - \Delta\beta, \quad (4)$$

where  $\Delta\beta$  is the propagation phase mismatch. From the attenuation of the resonator (e.g., from Fig. 3) an attenuation factor  $a_f$  can be calculated as follows:

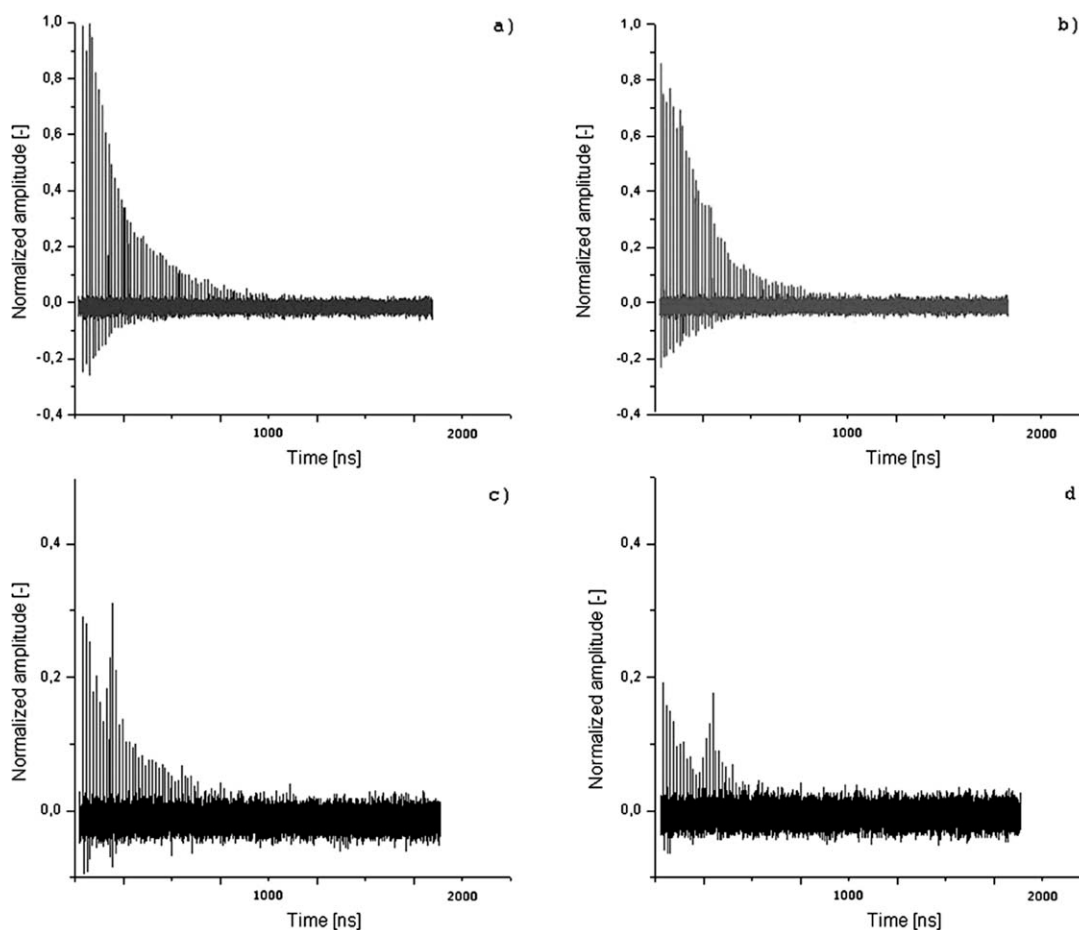


**Figure 4** Output pulses for different setting of variable delay line (VDL), (a) VDL = 33 mm, (b) VDL = 29 mm, (c) VDL = 27 mm, (d) VDL = 25 mm

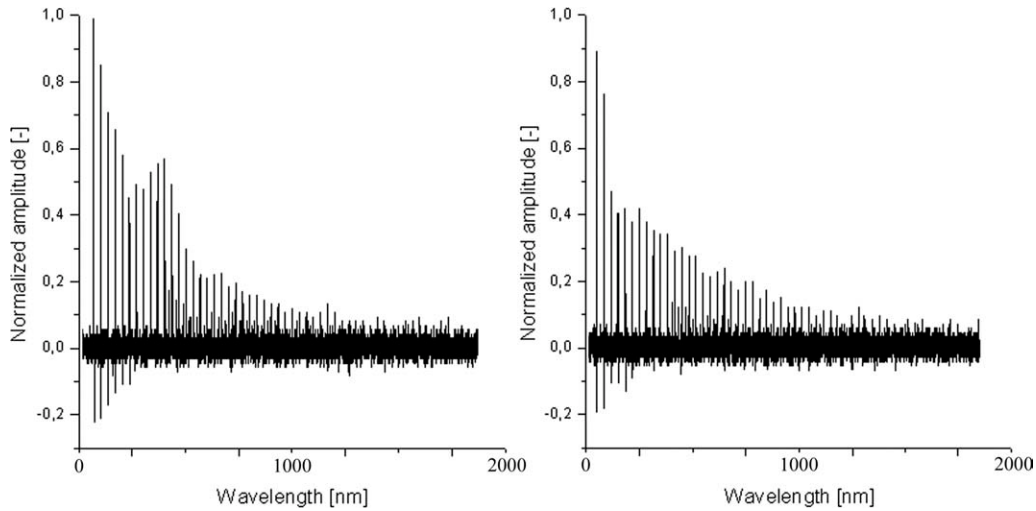


**Figure 5** Sampled pulses (left) and reference pulses (right) data sets

$$a_f = \sqrt[n-1]{\frac{A_n}{A_1}}, \quad (5)$$

where  $A_1$  is the amplitude of the first pulse and  $A_n$  represents the  $n$ th pulse at the output of the resonator. The reconstructed pulse can be expressed utilizing the measured pulse amplitudes and attenuation factor as:

$$A_{R(i)} = \frac{A_{FWM(i)} - A_{ref(i)}}{a_f^3}, \quad (6)$$

where  $A_{R(i)}$ ,  $A_{FWM(i)}$ , and  $A_{ref(i)}$  are the  $i$ th amplitudes of the reconstructed ( $R$ ), sampled FWM, and reference (ref) data sets.

### 3. RESULTS AND DATA ANALYSIS

The final experimental setup includes a resonator with the following parameters:  $L_R = 3.386$  m,  $\Delta\lambda = 7.6$  nm,  $\Delta T \sim 1.2$  ps, which give the round trip value of 16.592 ns and dispersion  $D = 46.6$  ps/nm·km. Highly nonlinear fiber with zero-dispersion wavelength of 1560 nm,  $L = 1500$  m,  $S = 0.016$  ps/nm<sup>2</sup>·km,  $\gamma = 11$  W<sup>-1</sup>·km<sup>-1</sup>, and  $\alpha = 0.86$  dB/km was used.

Output data were measured by a very fast photodiode with a bandwidth of 12.5 GHz and by a sampling oscilloscope capable of 20 Gsa/s attached to a PC.

Measured output data sets for different time matching, i.e., for different VDL length, are illustrated in Figure 4(a) represents VDL = 33 mm. In this case no FWM process can be observed and the output curve envelope shape after the HNLFF equals the output curve of the resonator. Contrary to that, the time dependence of amplitude for setting of VDL = 29 mm [Fig. 4(b)] shows slight signs of FWM. In the case of VDL = 27 mm the FWM process is clear but the amplitude of pulses has decreased [see Fig. 4(c)]. Finally, for VDL = 25 mm [Fig. 4(d)] the FWM signal can still be distinguished, but its amplitude is close to noise level, therefore it was not utilized for pulse reconstruction.

For the reconstruction of the data pulse, i.e., pulse shape, two sets of data were needed, because cross-talks to the idler region were present and it was not possible to detune the signals farther from each other (the walk-off would be influenced). The attenuation factor was obtained by analyzing data at the output of the resonator itself. Data set depicted in Figure 5 represents the FWM output [Fig. 5(a)] and reference data not experiencing any FWM [Fig. 5(b)].

The pulse mathematical reconstruction in accordance with (6) is demonstrated in Figure 6. It can be stated that the experimental results match the theory, i.e., the sinc-pulse fitting. Small deviations are caused by insufficiently sensitive photodetector and by amplifier added noise. Polarization mode dispersion was insignificant for this experiment.

### 4. CONCLUSION

A single-shot sampling oscilloscope was developed and investigated. The resonator made of two PM couplers proved to be a simple and sufficient device for pulse replication, though the attenuation of the loop limits number of usable samples for further sampling. For reduction of the round-trip attenuation the PM coupler pigtailed were spliced, which decreased the losses by a significant amount, but on the other hand eliminated the possibility of tunable walk-off by adjusting the length of the resonator. The implementation of direct amplification in the loop to compensate the losses is encouraged, but attention must be paid to prevent the loop from lasing. Significant problems were caused by the IN-OUT losses of the resonator, which in this experiment reached 40 dB. This drawback had to be compensated by an additional amplifier (EDFA), thus unfortunately adding additional noise to the signal pair.

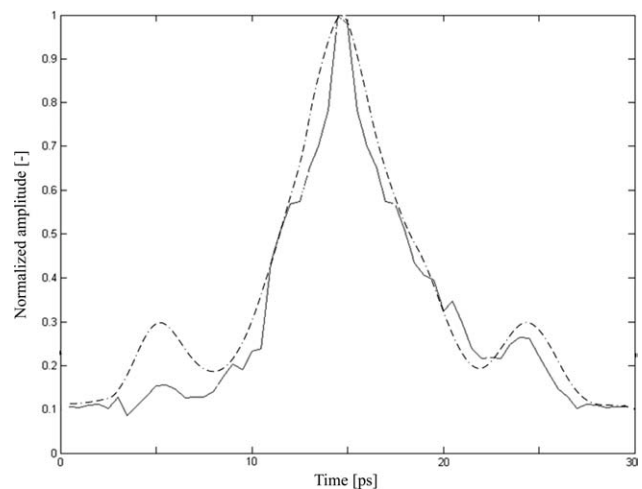


**Figure 6** Reconstructed pulse-shape (line) and sinc-fitting (dashed)

The FWM process showed good results and its main advantage is that it introduces a simple sampling method using only a highly nonlinear fiber, whereas other methods like nonlinear optical mirror require much more complicated setup. Its drawback, strong polarization dependence was suppressed by using PM fibers, couplers, and polarization controllers.

It has to be emphasized, the pulse shape reconstruction matches the theory well, when neglecting small inaccuracies caused by detection and signal distortion due to added noise.

A variant with classic SM fiber in the resonator setup together with a nonlinear optical loop mirror sampler was tested, using the XPM sampling method, for better method comparison. This approach showed insufficient results for pulse shape reconstruction and is therefore not presented in this article.

## ACKNOWLEDGMENTS

This work was supported through grants obtained from the Academy of Sciences of the Czech Republic (IST 300670502) and from the Ministry of Education, Youth, and Sports of the Czech Republic (MSM 6840770014).

## REFERENCES

1. J. Li, J. Hansryd, P.O. Hedekvist, P.A. Andrekson, and S.N. Knudsen, 300-gb/s eye-diagram measurement by optical sampling using fiber-based parametric amplification, *IEEE Photon Technol Lett* 13 (2001), 987–989.
2. K.-L. Deng, R.J. Runser, I. Glesk, and P.R. Prucnal, Single-shot optical sampling oscilloscope for ultrafast optical waveforms, *IEEE Photon Technol Lett* 10 (1998), 397–399.
3. P.A. Andrekson and M. Westlund, Nonlinear optical fiber based high resolution all-optical waveform sampling, *Laser Photon Rev* 1 (2007), 231–248.
4. M. Westlund, H. Sunnerud, M. Karlsson, and P.A. Andrekson, Software synchronized all-optical sampling for fiber communication systems, *J Lightwave Technol* 23 (2005), 1088–1099.
5. C. Dorrer, J. Bromage, and J.D. Zuegel, High-dynamic-range single-shot cross correlator based on an optical pulse replicator, *Opt Express* 16 (2008), 13534–13544.
6. T. Torounidis, Fiber optic parametric amplifiers in single and multi wavelength applications, Photonics Laboratory, Department of Microtechnology and Nanoscience, Chalmers University of Technology, Goteborg, 2006, p. 94.
7. G.P. Agrawal, *Nonlinear fiber optics*, Academic Press, San Francisco, 2001.

© 2010 Wiley Periodicals, Inc.

## TUNABLE FREQUENCY EQUALIZATION USING VARIABLE OPTICAL TILT FILTER IN RADIO-OVER-FIBER LINKS

Lan Liu,<sup>1</sup> Shilie Zheng,<sup>1</sup> Jun Ji,<sup>1</sup> Minghui Guo,<sup>1</sup> Xianmin Zhang,<sup>1</sup> Xiaofeng Jin,<sup>1</sup> Hao Chi,<sup>1</sup> and Yingyin Kevin Zou<sup>2</sup>

<sup>1</sup>Department of Information Science & Electronic Engineering, Zhejiang University, Hangzhou 310027, China; Corresponding author: zhengsl@zju.edu.cn

<sup>2</sup>Boston Applied Technologies, Inc., 6F Gill Street, Woburn, MA 01801

Received 9 February 2010

**ABSTRACT:** Frequency equalization is essential for radio-over-fiber (RoF) applications due to the degraded performance at higher frequencies. In this article, an easily implemented scheme for tunable frequency equalization in RoF link is proposed. A tunable and reconfigurable

microwave photonic filter is used in this method, which is realized through variable optical tilt filter. © 2010 Wiley Periodicals, Inc. *Microwave Opt Technol Lett* 52:2456–2459, 2010; View this article online at [wileyonlinelibrary.com](http://wileyonlinelibrary.com). DOI 10.1002/mop.25505

**Key words:** frequency equalization; microwave photonic filter; variable optical tilt filter; tunability; reconfigurability

## 1. INTRODUCTION

In the last 2 decades, radio-over-fiber (RoF) technique has been considered as a promising technology in many applications, such as broadband wireless access, antenna remoting of cellular/personal communication system signals, photonic beam forming, and cable television distribution systems [1] due to its unique advantages of light weight, low loss, high capacity, and high immunity to electromagnetic interferences [2]. In RoF systems, one important issue that needs to be addressed for the link performance is the uneven frequency response over wide band, which may be caused by the fiber dispersion or the photonic components' degraded performance at higher frequencies [3], as in many applications the RoF link is required to operate over a wide bandwidth with high linearity [4]. Thus great efforts have been made to equalize the frequency response of RoF link. Expensive components, such as high-speed photodetector (PD) are generally used to improve the frequency response at higher frequencies. Fiber Bragg Gratings (FBG) is also used to remove the dispersion effects and get uniform response over wideband simultaneously [5–7]. Another method using diffraction filter to equalize the frequency response of RoF link is recently reported [8]. However, these mentioned methods can not realize tunable frequency equalization as their configuration is usually fixed. In this article, a new method is proposed to equalize the frequency response of RoF link with the help of microwave photonic filter (MWPF). It not only gets rid of expensive high-speed PD and complicated technique to manufacture FBG, but also has tunability and reconfigurability without complicating the system configuration. Moreover, this method underplays the importance of cooperation between transmitter and receiver.

## 2. SYSTEM DESCRIPTION

A novel component named variable optical tilt filter (VOTF), which is made of transparent electro-optic ceramic material, is the key component to realize the tunable frequency equalization of RoF link. It is a sinusoidal optical filter with transmission characteristics decided by an amplitude-tuning element and a phase-tuning element, both of which are made of OptoCeramic<sup>®</sup> materials [9] and can be controlled by separate bias voltages of electronic circuit ( $V_a$  for the amplitude element and  $V_p$  for the phase element). Figure 1 demonstrated the experimental responses of VOTF with different amplitude and phase realized by adjusting the bias voltages of  $V_a$  and  $V_p$ .

The configuration of the RoF link with tunable equalized frequency response is illustrated in Figure 2. Two tunable laser sources, which can be substituted by a tunable dual-wavelength laser source, are used to provide optical carriers. RF signal from the transmitter port is modulated upon the light waves with different wavelengths through the electro-optic modulator (EOM), converting the RF signal into optical signal. The modulated optical signals are transmitted through a coil of fiber with length  $L$  and then go through the VOTF. The output of the VOTF is finally beaten in PD, whose output can feedback into the control system to further adjust the bias voltages of VOTF.

The laser sources with two different wavelengths and long distance fiber form a MWPF, the frequency response of which is described as:

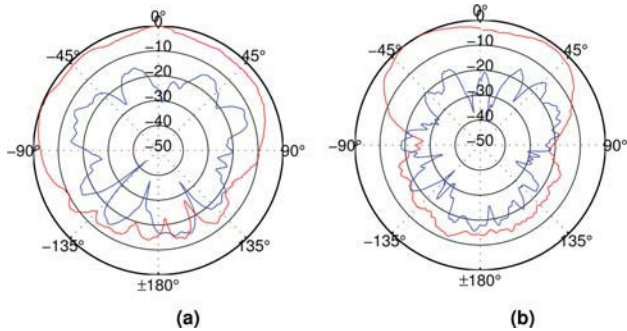


**Figure 8** Measured radiation patterns of hi-lo stacked patch antenna with 0.5-mm Rohacell foam at 21 GHz. (a) E-plane copolar and cross-polar and (b) H-plane copolar and cross-polar. [Color figure can be viewed in the online issue, which is available at [wileyonlinelibrary.com](http://www.wileyonlinelibrary.com)]

centered at 21 GHz. Also, the simulation result, which predicted result of 19%, with a slight shift lower in frequency for the measured results is shown in Figure 5. At frequencies above the impedance bandwidth, all results show significant undulation because of the generation of surface waves outside the active region of the antenna. This is a common trait for antennas built on a high dielectric substrate.

The predicted radiation patterns for the hi-lo stacked patch antenna at 21 GHz is shown in Figure 6. The measured radiation patterns of the antennas with the ECCOSTOCK FPH layer and Rohacell foam layer at 21 GHz are shown in Figures 7 and 8, respectively. It is evident from Figures 7 and 8 that the E- and H-plane copolar patterns have a similar contour to the simulated radiation pattern result in Figure 6. Measured cross-polarized patterns were higher than simulation; however, they still were around  $-20$  dB at broadside and typically below  $-15$  dB in the forward hemisphere. The minor rippling in the measured patterns can be attributed to the measurement frequency being above the preferred upper limit of the available antenna test facility.

The gain of the two fabricated antennas was measured and compared with the simulated gain. Both antennas produced  $\sim 5$  dBi gain at 21 GHz (mid-band), and had a variation across the bandwidth of around 2 dB. Simulated results were slightly higher on average than the measured gain, indicating that some loss of efficiency due to fabrication and alignment tolerances.

## 5. CONCLUSIONS

In this paper, the fabrication techniques to create ECCOSTOCK FPH substrate layer to an accurate thickness were presented. It has been shown that from the dielectric substrate point of view, this material proved to be a very good candidate to replace a Rohacell foam or air layer in high frequency stacked patch antennas, as thicknesses less than 1 mm can be achieved. A 0.5-mm-thick layer of ECCOSTOCK FPH was fabricated and tested as part of a 21-GHz hi-lo stacked patch antenna, achieving a bandwidth of 18.2% with  $\sim 5$  dBi gain. The results are comparable to the same antenna structure with a 0.5-mm Rohacell foam layer, allowing for a minor change in layer permittivity.

## REFERENCES

1. X. Liang, S. Zhong, and W. Wang, Design of a high isolation dual-polarized slot-coupled microstrip antenna, *Microwave Opt Technol Lett* 47 (2005), 212–215.
2. E.C. Kohls, Multi-layer flat plate antenna with low-cost material and high-conductivity processing, International Patent No WO 02/080302, October 10, 2002.

3. K.L. Lau, K.M. Luk, and K.F. Lee, Wideband U-slot microstrip patch antenna array, *IEE Proc Microwave Antennas Propag* 148 (2001), 41–44.
4. P.M. Haskins and J.S. Dahele, Low-cost linear arrays using polystyrene foam substrate, *IEE Colloquium Low-cost Antenna Technol* (1998), 1/1–1/5.
5. J. Xia, S.H. Tan, and K.A. Arichandran, Dual aperture-coupled microstrip patch antenna with two superstrate layers for use in microsatellite systems, *Microwave Opt Technol Lett* 20 (1999), 282–284.
6. C.-W. Su and J.-S. Row, Slot-coupled microstrip antenna for broadband circular polarisation, *Electron Lett* 42 (2006), 318–319.
7. R.B. Waterhouse, D. Novak, A. Nirmalathas, and C. Lim, Broadband printed sectorized coverage antennas for millimetre-wave wireless applications, *IEEE Trans Antennas Propag* 50 (2002), 12–16.
8. R.B. Waterhouse, Stacked patches using high and low dielectric constant material combination, *IEEE Trans Antennas Propag* 47 (1999), 1767–1771.
9. ECCOSTOCK FPH, Emerson and Cuming, available online at <http://www.eccosorb.com/file/172/fph.pdf> (accessed Jan 2011).
10. A.S. Elmezgghi and W.S.T. Rowe, Realization of MMIC integratable antennas with liquid foam dielectrics, In: *Proceedings of Asia Pacific microwave conference*, Hong Kong, J6–07, 2008.

© 2011 Wiley Periodicals, Inc.

## IMPROVED AXIAL FEEDING OF FABRY-PEROT RESONATOR FOR HIGH-RESOLUTION SPECTROSCOPY APPLICATIONS

Petr Černý, Petr Piksa, Stanislav Zvánovec, Tomáš Kořínek, and Václav Kabourek

Faculty of Electrical Engineering, Department of Electromagnetic Field, Czech Technical University in Prague, Technická 2, 166 27 Prague 6, Czech Republic; Corresponding author: [petr.cerny@fel.cvut.cz](mailto:petr.cerny@fel.cvut.cz)

Received 21 January 2011

**ABSTRACT:** This article presents the methods of broadband axial feeding of a Fabry–Perot resonator. The resonator was originally designed with the radial excitation for the absorption measurement in the frequency band ranging from 18 to 80 GHz. If the frequency stays below  $\sim 26.4$  GHz, the excitation of resonator is less satisfactory, since at the frequency in question, the value of Fresnel number of resonator drops to one. For the broadband measurement of gaseous samples' emission spectra, the excitations for frequencies lower than 26.4 GHz were analyzed using the capacitive coupling and two newly proposed couplings. © 2011 Wiley Periodicals, Inc. *Microwave Opt Technol Lett* 53:2456–2462, 2011; View this article online at [wileyonlinelibrary.com](http://wileyonlinelibrary.com). DOI 10.1002/mop.26344

**Key words:** Fabry–Perot resonator; axial excitation; absorption spectrum; emission spectrum; Fourier-transform microwave spectroscopy

## 1. INTRODUCTION

Owing to its vital quality parameters, the Fabry–Perot resonator (hereinafter referred to as FP resonator or resonator) is frequently used in both spectroscopy applications—absorption and emission measurements [1–3]. In the high-resolution microwave spectroscopy, a usual absorption experiment is handicapped, for the low pressure of sample gas hinders collision relaxation processes. Furthermore, the probability of relaxation processes

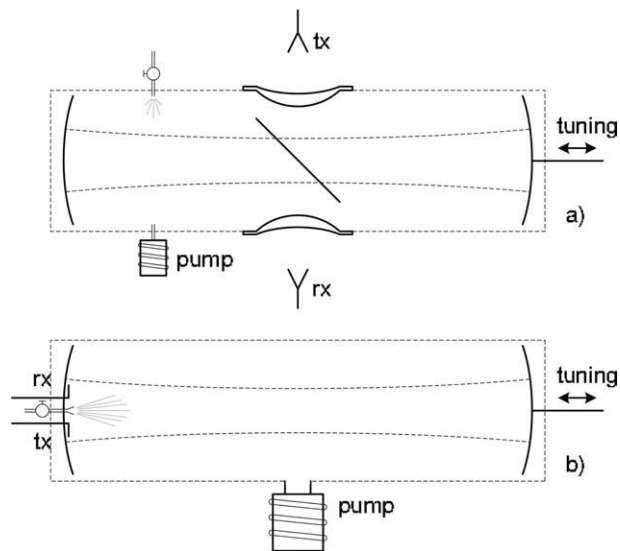


**Figure 1** FP resonator arrangement: (a) radial feeding and (b) axial feeding

caused by spontaneous emission falls with the third power of the frequency [1–7]. This means that the saturation transitions (i.e., equalization of level populations) represent the main restriction to the high-resolution absorption spectroscopy used at the lowest frequencies (from the spectroscopic point of view, this refers to the frequencies of up to 80 GHz).

The current research activities are targeted at the suppression of spectral lines broadening, which results from collisions of molecules. Indeed, the Fourier-transform microwave (FTMW) spectroscopy represents one of the most sensitive tools within the high-resolution microwave spectroscopy in the lowest measured frequency bands [1, 2].

In FTMW spectroscopy, the measured sample gas is excited by short pulses and, subsequently, the emission spectra can be measured [1, 3]. Moreover, it is possible to inject the gas into the resonator in the direction of resonator axis by a high pressure [i.e., the supersonic gas expansion preventing collisions of molecule [6]; Fig. 1(b)]. Indeed, owing to the supersonic gas expansion, the spectral lines are narrowed and the sensitivity of spectra measurement is enhanced. Provided that the resonator shows a high quality factor, the field decay in the resonator is extended and the intensity sensitivity accordingly attains higher levels. However, at higher frequencies, a very short emission is observed, whereas at lower frequencies, it lasts for significantly longer time. Consequently, to ensure an emission measurement that is accurate and sensitive enough, it is necessary to determine the optimum loaded quality factor of resonator.

This article substantially extends the formerly published preliminary results. In the previous work [8], three types of axial excitation (namely the capacitive as well as inductive excitations and the proposed type of coupling) were under consideration and subjected to comparison, on the basis of the measurement in the frequency band from 18 to 40 GHz. Nevertheless, as the feeding of coupling elements was equipped with SMA connectors, the published results were unreliable for frequencies over 26.5 GHz, because of the frequency cut-off of SMA connectors. This article discusses the improved characteristics of two previously presented axial excitations—the capacitive excitation on one hand and the proposed coupling on the other.

The Fresnel number of the discussed FP resonator is equal to one on condition that the frequency ranges from 26.37 to 27.17

GHz for different mirror distances. If the frequency stays below this value, the quality parameters and functionality of the resonator tend to fall rapidly as long as the frequency decreases. This is due to the diffraction loss [9, 10]. If the Fresnel number exceeds one, the diffraction loss is negligible (Fig. 4). In addition, the coupling of the resonator declines as the frequency drops. The effect in question cannot be compensated by any of the aforementioned resonator feeding types. As a result, the new type of resonator excitation was designed. Its main features are presented in this article. It was developed to ensure a suitable value of resonator coupling and to extend the bottom frequency limit of the FP resonator, where the Fresnel number is lower than one.

## 2. FABRY-PÉROT RESONATOR

The FP resonator [Fig. 1(a)] is deemed a remarkable tool. As for monochromatic radiation, the FP resonator can be tuned to a resonance, at which the constructive interference of the multiple-reflections provides the accumulation of energy emitted by the measured sample gas. The improvement in the sensitivity of the FP resonator is then linked to its high quality factor.

The FP resonator, developed at the Department of Electromagnetic Field of the Czech Technical University in Prague, was equipped with the radial feeding (i.e., perpendicular to the resonator cavity) via thin dielectric coupling foil located in the middle of the resonator [Fig. 1(a)] [9]. The FP resonator is composed of two spherical mirrors for setting of particular resonance. In fact, one mirror is in a fixed position, while the other one can be positioned with a 0.05- $\mu\text{m}$  step. The diameter of spherical mirrors equals 150 mm, the curvature radius of spherical mirrors accounts for 455 mm, and the adjustable mirror distance ranges from 495 to 510 mm.

However, the dielectric foil can act as an obstacle, if the intended pulsed molecular beam is injecting the measured sample gas into the main axis of resonator. Therefore, it was beneficial to use the axial excitation of the resonator, because it enabled the application of pulsed molecular beam.

## 3. AXIAL FEEDING OF RESONATOR

In axial excitation of the FP resonator, there were no obstructions to the pulsed molecular beam of the injected sample gas. So, a substantial advancement in the measured spectra resolution could be achieved. The best position of the gas nozzle is in the center of the fixed mirror of the FP resonator. Thus, positions of excitation elements have to be shifted off the resonator axis [Fig. 1(b)]. Their most suitable localization can be derived as a compromise among the following conditions. First, the direct transmission between the transmitting and receiving coupling elements should be minimized by extending their mutual distance. Second, the best coupling can be obtained as long as the positions of coupling elements correspond to the locations, where the dominant mode  $\text{TE}_{00q}$  and, at the same time, the non-dominant modes attain their maximum and minima, respectively. It means that they are situated on the mirror axis, where the dominant mode (commonly with some nondominant modes) reaches a maximum and some other nondominant modes attain their minima. Third, the impulse valve should be located between coupling elements. The second and third conditions are of a higher significance. Thus, the position of coupling elements was designed to be as close as possible to the impulse valve. In our case, the best mutual distance of excitation elements was determined to be equal to 31.3 mm. The beam radius of the dominant mode  $\text{TE}_{00q}$  on the mirrors amounts to 35.1 mm

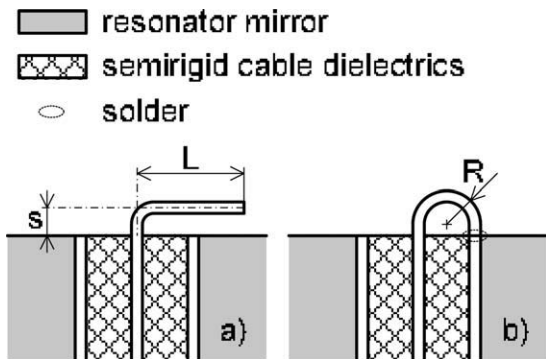


**Figure 2** Common coupling types: (a) capacitive coupling and (b) inductive coupling

(computed using equations in Ref. 10 for the upper frequency 40 GHz). Thus, it can be stated that the coupling elements are still located in the area, where the sweeping majority (more than 90%) of the energy is accumulated.

Instead of the radial electromagnetic coupling provided by the dielectric coupling foil and situated outside the antennas, both the capacitive and inductive couplings are commonly used [Figs. 2(a) and 2(b), respectively]. For the spectroscopic purposes, the arrangement with two coupling elements is used. The first one is used for the resonator excitation by the microwave impulse, whereas the second port is used for the purpose of reception of signal emitted by the excited sample gas (spontaneous emission). Both coupling elements (transmitting and receiving units) are aligned in the axis, having their parts parallel with mirror pointing themselves to opposite directions.

For the feeding of coupling elements, two holes were manufactured in the fixed resonator mirror. As it is illustrated in Figure 13, two semirigid cables were inserted hermetically into these holes. The inner diameter of the cable accounts for 0.46 mm, whereas the outer is worth 1.65 mm. The vacuum-tightness of semirigid cables and their passing through mirror were investigated as well. The semirigid cables are equipped with the 2.92-mm connectors. The transmission coefficient between the aforementioned connectors (ports) was measured using the vector network analyzer Agilent E8364A in the frequency band

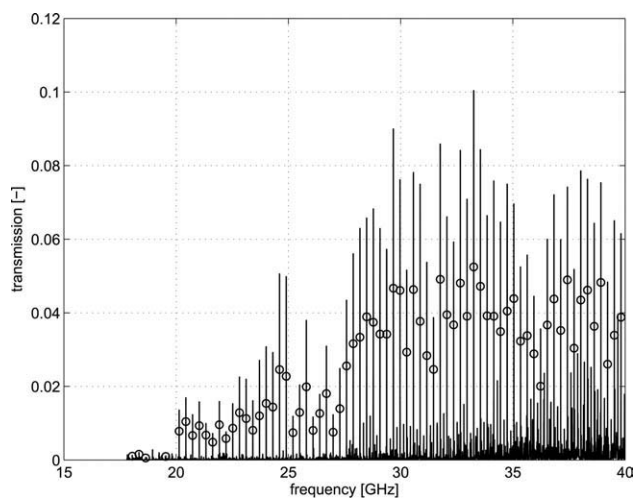


**Figure 3** Transmission of the weak capacitive coupling,  $L = 4$  mm

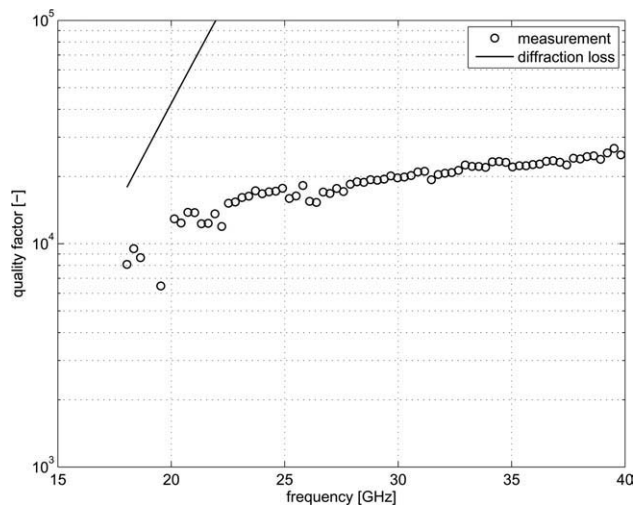


**Figure 4** Quality factor of the weak capacitive coupling,  $L = 4$  mm

ranging from 17.8 to 40 GHz with the step of 250 kHz. The simple correction on transmission coefficient  $S_{21}$  was provided (neither of the full two-port methods were used). The correction in question is based on the through calibrator. The error of the used correction methods was tested and is less than 0.1 dB. The reference planes were chosen at the planes of connectors. The loaded quality factor (hereinafter referred to as quality factor) is consequently evaluated on the basis of the measured transmission coefficient. The losses of semirigid cables were not subjected to correction. They are included in the measured transmission coefficient.

It should be emphasized that in this article, the strength of the coupling was not evaluated in classical terms of couplings (i.e., critical, undercritical, and abovecritical [11, 12]). It was necessary to categorize the couplings according to the transmission coefficient value of resonance maxima. A coupling can be classified as a small one, provided that the resonances reach their maxima at values lower than 0.1 of the transmission coefficient. If the aforementioned level is higher than 0.1, it is possible to classify the coupling as a middle coupling. As it is demonstrated in Figure 2, the coupling strength can be set up by the change of the spacing  $s$  of coupling elements. Because of its large spacing and transmission remaining unchanged or starting

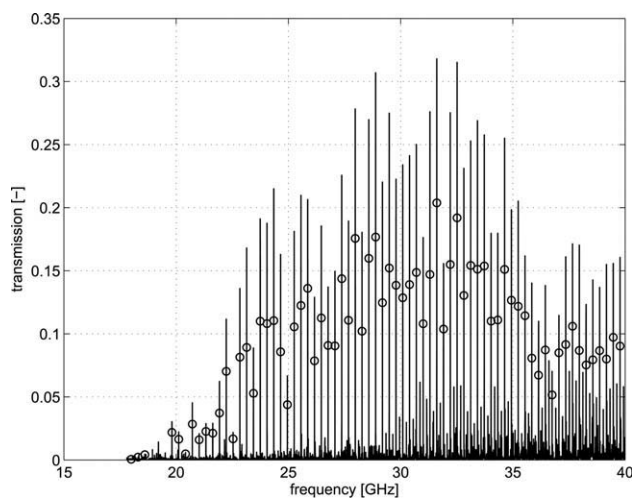


**Figure 5** Transmission of the middle capacitive coupling,  $L = 4$  mm

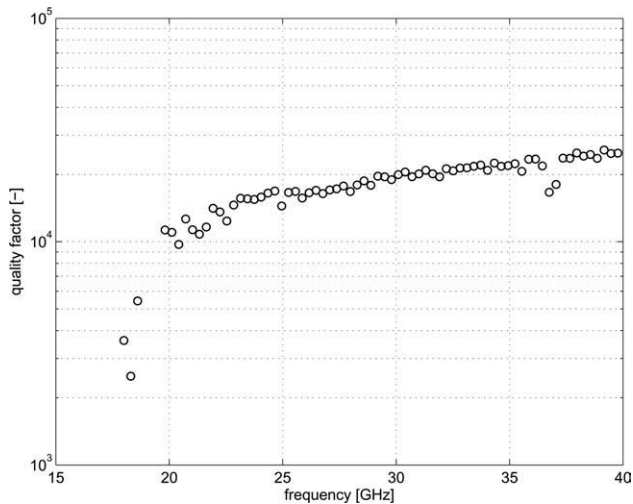


**Figure 6** Quality factor of the middle capacitive coupling,  $L = 4$  mm

to slightly drop, the coupling could be classified as a strong one. The spacing will be indicated later in the article individually for each coupling.

Moreover, the transmissions and quality factors were evaluated all over the measured frequency range. During the transmission evaluation, the particular resonance was marked if the frequency of measured peaks met the resonance condition of the FP resonator (in the following figures, such frequencies are going to be highlighted by a red circle) [9]. In these resonance frequencies, the quality factor of each particular resonance was assessed (Figs. 3–7 and 9–12).

#### 4. FEEDING BY CAPACITIVE COUPLING

The capacitive coupling is frequently used for the axial excitation of resonators [5, 7, 11, 12]. The radiating element of capacitive coupling is parallel to the resonator mirror (i.e., to the ground plane). In this point, it differs from a standard monopole antenna. However, as for requirements (mainly the sensitive and high-resolution spectroscopy) applying to both, the coupling and antenna, it is essential to set up the radiating element length and the distance from the ground plane (i.e., resonator mirror) for each frequency.

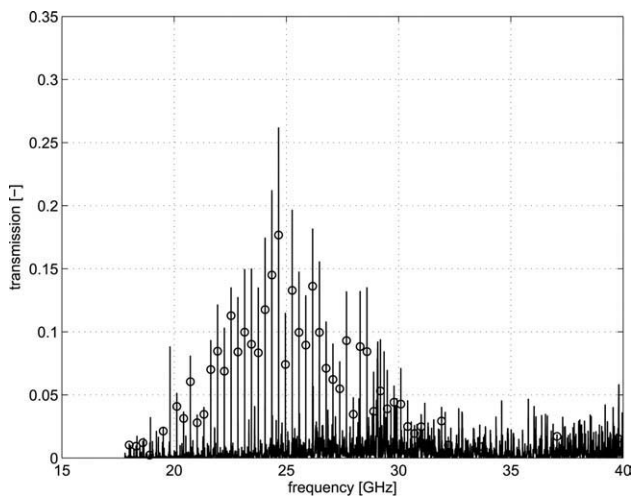


**Figure 7** Transmission of the strong capacitive coupling,  $L = 7$  mm

The capacitive coupling can be manufactured by perpendicular bending of the inner conductor of a semirigid cable [Fig. 2(a)]. In air environment, for the lowest supposed working frequency of the FP resonator, the length,  $L$ , of the radiating element of the capacitive coupling was designed as a quarter of wavelength (i.e., similar to the design of a monopole above the ground plane). In this case, it achieves 4.1667 mm for the frequency of 18 GHz. Because of the close vicinity of the bended inner conductor to the mirror, the lower working frequency of capacitive coupling is shifted toward the higher frequencies. The reflections out of the resonances tend to approach the total reflection. In addition, the reflections involve shallow drops corresponding to resonances. Results for the weak coupling indicated in Figures 3 and 4 were obtained for the spacing  $s = 0.02$  mm, whereas those for the middle coupling mentioned in Figures 5 and 6 were attained for the case where the spacing,  $s$ , was equal to 0.1 mm.

The weak coupling can be characterized by a very low transmission coefficient (up to 0.1; see Fig. 3) and also by a flat and high value of the quality factor. The latter reaches a level in the vicinity of 20,000 at the frequency of 30 GHz (Fig. 4). It is obvious that it slightly rises as the frequency advances. The middle coupling can be characterized by a transmission coefficient surpassing 0.1 (Fig. 5). As it is indicated in Figure 6, the quality factor shows a similar tendency and reaches the level of 20,000 at the frequency of 30 GHz. The strong coupling can be then characterized by a longer distance between the coupling element and the resonator mirror. It gives rise to a slight decrease in the quality factor, although it did not significantly affect its tendency. The quality factor remains below the value of 20,000. In addition, the transmission slightly decreases (for instance if the distance,  $s$ , equal to 1 mm, it drops by  $\sim 5\%$ ), unlike the parasitic transmissions and nondominant resonances that move upward. With respect to the differences among the reached values of quality factors, the couplings under consideration thereafter show similar behaviors in terms of coupling strength and spacing distance between the coupling element and mirror.

If the length of bended part is equal to 4 mm then the capacitive coupling provides a very broadband coupling with a very good performance. However, the coupling proposed in Ref. 8 showed better performance in the low-frequency band with an extended length  $L$  (7 mm). Accordingly, the capacitive coupling was also tested with the same length  $L = 7$  mm (Fig. 7). The best results were obtained in the case of strong coupling, where the spacing,  $s$ , accounts for 0.6 mm.

As it is clear from the transmission indicated in Figure 7, the capacitive coupling with longer coupling elements belongs to the narrowband coupling. So, it means that the transmission exceeds 0.1 within the frequency band of  $\sim 22$ –28 GHz. Outside this band, the transmission tends to fall steeply. The quality factor is not flat within this frequency band. It has a tendency to rise from the value of 10,000 up to 18,000 within the frequency range 20–30 GHz. The resonances were not recognized for the frequencies higher than 30 GHz. Thus, this coupling is unsuitable either for the broadband axial excitation of the FP resonator or for the excitation within a low-frequency band.

#### 5. FEEDING BY PROPOSED COUPLINGS

In this section, two types of the coupling (the improved version of the type proposed in Ref. 8 and the new one) are going to be under scrutiny. To excite the resonator, the coupling elements should be similar to the capacitive coupling—especially in terms

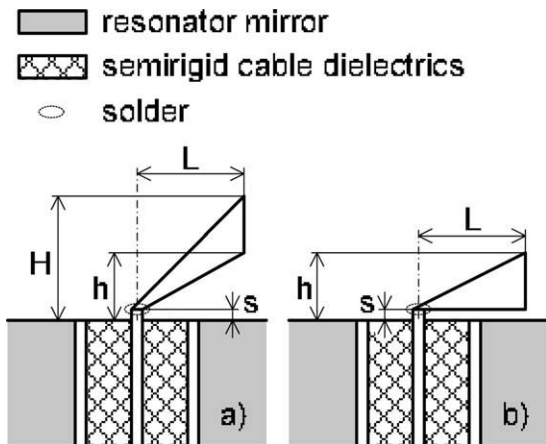


**Figure 8** Proposed coupling types: (a) coupling proposed in Ref. 8 and (b) new coupling

of the coupling elements' orientation. The formerly proposed coupling element shape [8] was derived from the shapes of ultra wideband monopoles [13] (e.g., elliptic, triangular, fat/rectangular, etc.).

Hence, the coupling element shape was designed as a linearly tapered element (within the interval from 0.3 to 2.3 mm), having the following dimensions: length of elements,  $L$ , accounts for 7 mm and the dimensions of the element are  $h = 1.7$  mm and  $H = 4$  mm. The spacing issues are going to be discussed later on.

In comparison to the radiation of dipoles above the ground plane, in the case of the radiation in the normal direction to the mirror, the perfect broadband (ultra wideband) parameters degrade. This phenomenon originates from the short distance between the radiating (or coupling) elements and the resonator mirror. Thus, the first proposed coupling element was originally designed and presented with a linearly tapered gap between the bottom edge of the coupling element and the resonator mirror [8] [Fig. 8(c)]. This element was tested with the middle coupling, where the spacing,  $s$ , equals 0.1 mm (Figs. 9 and 10).

The simulation and optimization of the proposed axial excitation were performed in the CST MWS simulation software. The structure was excited by the basic Gaussian impulse for the frequency range of 0–40 GHz. It was determined that the energy

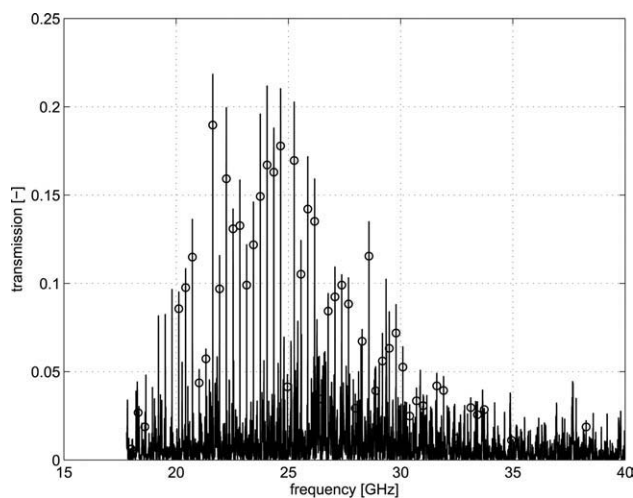


**Figure 9** Transmission of previously proposed the coupling

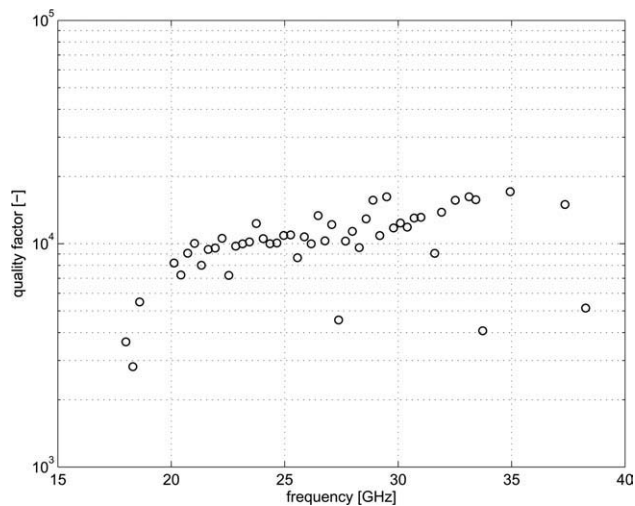


**Figure 10** Quality factor of previously proposed the coupling

was mostly radiated within the frequency band ranging roughly from 18 to 28 GHz and reached its maximum at the frequency in the vicinity of 25 GHz [8].

The measured transmission corresponds to the frequency response of the radiated energy very well [8]. Nevertheless, it was observed that the coupling was weaker than that in case of the capacitive coupling. The transmission characteristic comprises several drops in resonance peak values, mainly in the lower frequency band. It also contains many parasitic transmissions reaching levels up to 0.05. It was observed that the quality factor was lower than that in case of the capacitive coupling and not as flat as needed.

Given these uncomplimentary results, the new capacitive coupling was designed, based on the prior capacitive and previously proposed couplings. The new coupling also has the shape of a linearly tapered element. Contrary to the previously proposed coupling described above, the distance between the bottom edge of the coupling element and the resonator mirror is not linearly tapered, yet it has a constant value [identically to the capacitive coupling; Fig. 8(d)].

The optimized dimensions of the new coupling are given below: length of elements,  $L$ , accounts for 7 mm and the height of the element,  $h$ , amounts to 2.2 mm. The dimensions were

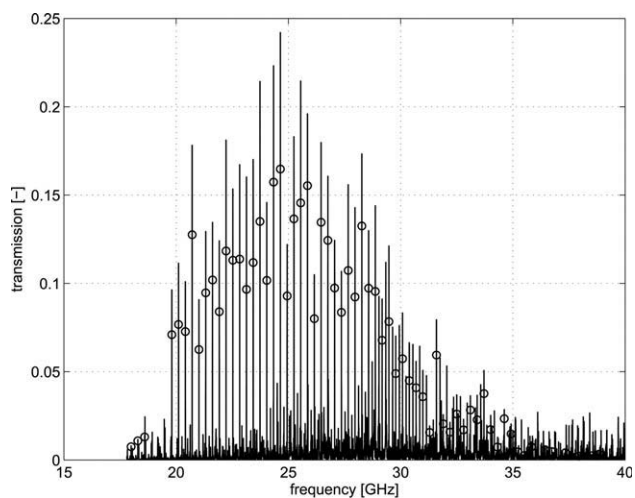


**Figure 11** Transmission of the new coupling

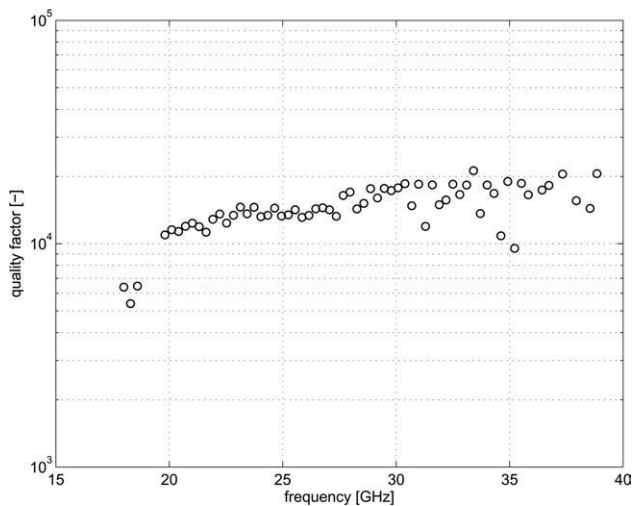


**Figure 12** Quality factor of the new coupling

optimized by the step-by-step optimization method based on parametric analyses. The main factors of the optimization consisted in the magnitude of radiated energy and its flatness in the required frequency band (20–30 GHz). The new coupling was tested for the middle coupling obtained with the spacing,  $s$ , equal to 0.1 mm (results indicated in Figs. 11 and 12).

The new coupling elements provide a better performance than the previously tested types of coupling. It can be summarized that the transmission contains fewer parasitic components that even attain substantially lower levels. The coupling is stronger and provides good parameters within the frequency range of  $\sim 20$ –29 GHz. However, there are some drops in the low-frequency band. The frequency dependence of the quality factor



(a)



(b)

**Figure 13** Photographs of (a) the new axial excitation and (b) the pulse valve for the pulse molecular beam. [Color figure can be viewed in the online issue, which is available at [wileyonlinelibrary.com](http://wileyonlinelibrary.com)]

proves to be relatively flat. In addition, higher values of quality factor were reached.

Photographs of the new manufactured excitation and the pulse valve for the pulse molecular beam are depicted in Figures 13(a) and 13(b), respectively.

## 6. CONCLUSIONS

Four types of axial excitation of the FP resonator were investigated and discussed: the capacitive coupling of two different lengths, the enhanced version of the previously proposed coupling [8], and the new type of coupling. The capacitive coupling, having the length of coupling element equal to 4 mm, provides a very good broadband performance. This type of coupling shows the broadest frequency range (23–40 GHz). In addition, its quality factor proves to achieve the highest values and the flattest character. Owing to these parameters, it is commonly used for the resonator excitation. Nonetheless, this kind of excitation suffers from drops at lower frequencies, where the Fresnel number of resonator stays significantly below one. To enlarge the working frequency range of the FP resonator toward the lower frequencies, other types of axial excitation were investigated.

The capacitive coupling with a length  $L = 7$  mm and the coupling proposed in Ref. 8 do not offer suitable parameters. When compared with the capacitive coupling of the length  $L = 4$  mm in the higher frequency band, the employment of the new type of coupling leads to a satisfactory performance. Moreover, it provides very good parameters even for the frequency band, in which the Fresnel number of the FP resonator does not surpass one. The new coupling has the transmission exceeding 0.1 within the broad frequency range (20–30 GHz). Because of its utilization, the resonator reaches a relatively flat quality factor. As in the case of the aforementioned coupling types, the quality factor shows a slightly progressive tendency (from 20 GHz upward).

## ACKNOWLEDGMENTS

The research was undertaken at the Department of Electromagnetic Field of the Czech Technical University in Prague within the research project of the Ministry of Education, Youth and Sports of the Czech Republic LC06071 and the research project of the Czech Science Foundation P206/10/2182.

## REFERENCES

1. J.-U. Grabow and W. Caminati, Microwave spectroscopy: Experimental techniques, In: J. Laane (Ed.), *Frontiers of molecular spectroscopy*, Elsevier, 2009, pp. 383–454.
2. W. Caminati and J.-U. Grabow, Microwave spectroscopy: Molecular systems, In: J. Laane (Ed.), *Frontiers of molecular spectroscopy*, Elsevier B.V., 2009, pp. 455–552.
3. S. Zvanovec, P. Cerny, P. Piksa, T. Korinek, P. Pechac, M. Mazanek, J. Varga, J. Koubek, and S. Urban, The use of the Fabry–Perot interferometer for high resolution microwave spectroscopy, *J Mol Spectrosc* 256 (2009), 141–145.
4. U. Andresen, H. Dreizler, J.U. Grabow, and W. Stahl, An automatic molecular beam microwave Fourier transform spectrometer, *Rev Sci Instrum* 61 (1990), 3694–3699.
5. J.-U. Grabow, W. Stahl, and H. Dreizler, A multioctave coaxially oriented beam-resonator arrangement Fourier-transform microwave spectrometer, *Rev Sci Instrum* 67 (1996), 4072–4084.
6. M. Schnell, D. Banser, and J.-U. Grabow, Coaxially aligned electrodes for Stark-effect applied in resonators using a supersonic jet Fourier transform microwave spectrometer, *Rev Sci Instrum* 75 (2004), 2111–2115.

7. J.-U. Grabow, E.S. Palmer, M.C. McCarthy, and P. Thaddeus, Supersonic-jet cryogenic-resonator coaxially oriented beam-resonator arrangement Fourier transform microwave spectrometer, *Rev Sci Instrum* 76 (2005), 093106–093111.
8. P. Cerny, P. Piksa, T. Korinek, S. Zvanovec, and M. Mazanek, Broadband axial excitation of Fabry–Perot resonator, In: *Antennas and propagation (EuCAP)*, 2010 proceedings of the fourth European conference, 2010, pp. 1–4.
9. P. Piksa, S. Zvanovec, and P. Cerny, Specific millimeter-wave features of Fabry–Perot resonator for spectroscopic measurements, In: I. Minin (Ed.), *Microwave and millimeter wave technologies from photonic bandgap devices to antenna and applications*, InTech, 2010, pp. 451–468.
10. H. Kogelnik and T. Li, *Laser beams and resonators*, Proc IEEE, 54 (1966), 1312–1329.
11. G. Goubau, *Electromagnetic waveguides and cavities*, Pergamon Press, New York, 1961.
12. D.M. Pozar, *Microwave engineering*, John Wiley & Sons, Inc., New York, NY, 1998.
13. P. Cerny, Optimization of UWB dipole feeding circuits, In: *Antennas and propagation (EuCAP)*, 2010 proceedings of the fourth European conference, 2010, pp. 1–4.

© 2011 Wiley Periodicals, Inc.

## VERTICAL-CAVITY SURFACE-EMITTING LASER BASED DIGITAL COHERENT DETECTION FOR MULTIGIGABIT LONG REACH PASSIVE OPTICAL LINKS

Roberto Rodes,<sup>1</sup> Jesper Bevensee Jensen,<sup>1</sup> Darko Zibar,<sup>1</sup> Christian Neumeyr,<sup>2</sup> Enno Rönneberg,<sup>2</sup> Juergen Roskopf,<sup>2</sup> Markus Ortsiefer,<sup>2</sup> and Idelfonso Tafur Monroy<sup>1</sup>

<sup>1</sup>DTU Fotonik, Department of Photonics Engineering, Technical University of Denmark, DK-2800 Kgs. Lyngby, Denmark; Corresponding author: rrl@fotonik.dtu.dk

<sup>2</sup>VERTILAS GmbH, Lichtenbergstr. 8, Garching D-85748, Germany

Received 27 January 2011

**ABSTRACT:** We report on experimental demonstration of digital coherent detection based on a directly modulated vertical-cavity surface-emitting laser with bit rate up to 10 Gbps. This system allows a cooler-less, free running, and unamplified transmission without optical dispersion compensation up to 105 km at 5 Gbps long reach passive optical links. © 2011 Wiley Periodicals, Inc. *Microwave Opt Technol Lett* 53:2462–2464, 2011; View this article online at [wileyonlinelibrary.com](http://wileyonlinelibrary.com). DOI 10.1002/mop.26331

**Key words:** VCSEL; coherent detection; optical communications

### 1. INTRODUCTION

Emerging high bandwidth demanding services, such as high definition television (HDTV), are calling for capacity upgrade of existing and to be deployed fiber-to-the-customer (FTTC) networks [1]. Another challenge for FTTC networks is the need to support a growing number of end-users while keeping low the overall cost of delivered unit of bandwidth. Therefore, in FTTC architectures such as passive optical network (PON) architectures, it is important to reduce the cost of the optical network unit and concentrate complex signal processing at the central office, where complexity and cost can be shared among all users. Vertical-cavity surface-emitting lasers (VCSELs) are promising candidates for light sources at the customer premise because of their cost-effective production and capability for chip integration with low threshold and driving current operation.

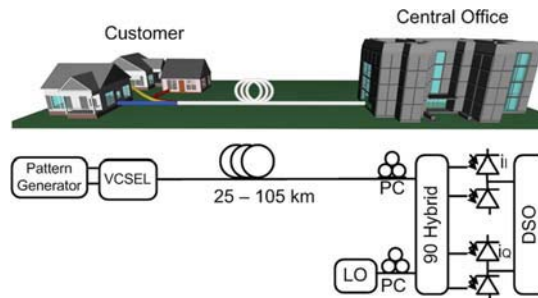


**Figure 1** Experimental setup. Local oscillator (LO), polarization controller (PC), and digital sampling oscilloscope (DSO). [Color figure can be viewed in the online issue, which is available at [wileyonlinelibrary.com](http://wileyonlinelibrary.com)]

Compared with DFB-lasers, the main challenge for VCSELs so far is the smaller optical power coupled into the optical fiber, which restricts the coverage range for application in PON links with a large splitting ratio and long transmission distance. A common solution for this power budget limitation would be to include optical amplifiers [2] that drastically would undermine the cost advantage of VCSELs. Until now, fiber transmission systems using VCSELs employ direct detection.

In this article, for the first time to our best knowledge, we experimentally demonstrate the use of digital coherent detection of a 10 Gbps amplitude shift keying system using a VCSEL as light source. Commonly, the typical large linewidth value of VCSELs has made them not suitable for coherent detection [3].

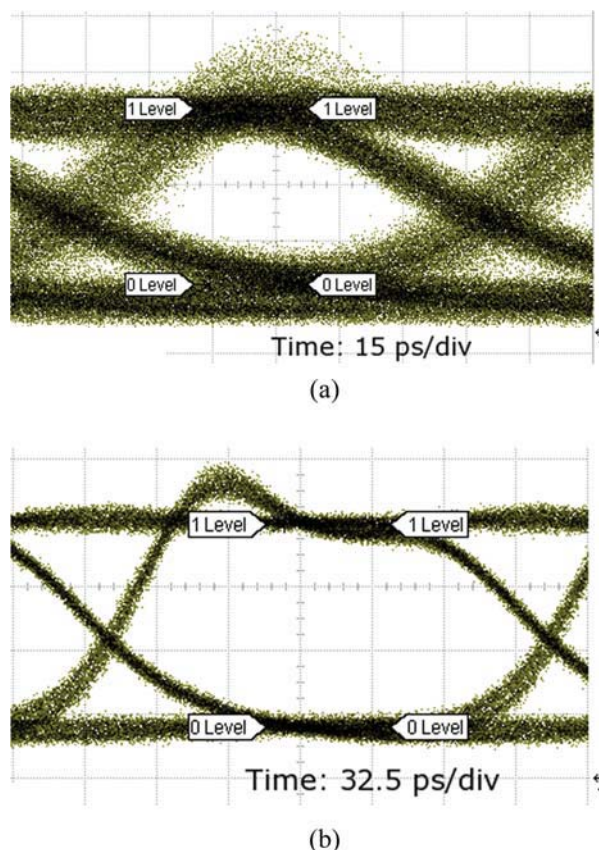


**Figure 2** Optical back-to-back direct detected eye diagrams for (a) 10 Gbps and (b) 5 Gbps. [Color figure can be viewed in the online issue, which is available at [wileyonlinelibrary.com](http://wileyonlinelibrary.com)]

# Rain Spatial Classification for Availability Studies of Point-to-Multipoint Systems

Stanislav Zvanovec, *Member, IEEE*, and Pavel Pechac, *Senior Member, IEEE*

**Abstract**—Signal propagation at frequencies above 10 GHz suffers from significant attenuation due to precipitation. This has to be taken into account when planning point-to-multipoint (PMP) wireless systems operating in the millimeter wave band. Given the nonuniform spatial distribution of the rain rate, the site diversity concept emerges as one of the mitigation techniques. For propagation studies of PMP systems during rain events, rain spatial properties and their corresponding impact on system behavior has to be investigated. An extensive database of rainfall radar data for various types of rain events has been established. System outage improvement was studied using space-time simulations of PMP systems under specific rain conditions. A new approach to rain spatial classification according to its impact on system performance is proposed, using a single rainfall spatial parameter. Examples of its calculation are presented.

**Index Terms**—Diversity methods, millimeter wave propagation, rain.

## I. INTRODUCTION

THE increasing demand for much faster broadband connections has led to increased pressure to employ the higher frequencies that currently remain unused in the radio spectrum. Point-to-multipoint (PMP) wireless systems such as fixed wireless access (FWA) [1], local multipoint distribution systems (LMDS), multimedia wireless systems (MWS) etc. operate in millimeter wave bands throughout the world. However, frequencies above 10 GHz suffer from significant attenuation due to rain, which means that, for a proper understanding of the behavior of PMP systems during rain events, rain properties and their impact on the system have to be studied.

An important characteristic of a rain event for propagation studies in millimeter wave bands is its nonuniform spatial and temporal distribution. Site diversity can be used in PMP networks as one of the more powerful mitigation techniques as a user can potentially be linked to two or more base stations (BSs) at the same time. Links with an angle and/or distance separation usually result in considerable improvements to system performance during rain events, since the attenuation statistics for a single path and two diversity paths are very likely different, as can be observed from the two links in [2].

Comprehending the spatial properties of rainfall and their consequent effects on PMP system performance is a complex

problem and it would be beneficial to devise a simple way of classifying rain rate spatial distribution. To enable us to produce a comprehensive description of the influence of rainstorms on PMP systems, the site diversity statistics of a system as a whole have been investigated in this paper. Based on outage statistics, a new classification of rain spatial characteristics has been proposed and a new rainfall spatial parameter has been derived.

The paper is organized using the following pattern. The basic features of PMP system simulations are briefly described in Section II and the key input parameter of our model, a radar rainfall database, is also introduced. Subsequently, an overview of site diversity investigations, including results obtained from the simulations, is provided. In the following subsection, system outage improvement probability is derived from the radar data as a function of the rain parameters, the rain fade margin, the angle separation and the distances of the base stations. Section III proposes a new classification method for rain spatial characteristics, based on PMP system outages as well as depicting rain statistics and spatial properties that are typical for the Czech Republic. Section III also gives examples of the utilization of a newly defined rainfall spatial parameter, enabling us to derive the outage improvement probability in PMP systems based on rainfall radar images. A discussion follows on the validity of the classification method. The paper concludes with a brief summary.

## II. PMP SYSTEM SIMULATIONS

### A. Simulation Tool

A propagation simulation tool to study the performance of PMP systems under different signal propagation conditions and in various configurations has been developed [3]. The PMP system is formed by a network of base stations and terminal stations (TSs). The positions of the BSs are provided by a user or generated randomly over a selected area. TSs are randomly generated, based on user-defined rules (evenly distributed or with several centers denoting higher user density in city centers) or loaded from a file. The digital terrain model can be read from a realistic GIS input. The building database can also be read as an input or generated randomly using a statistical model [4].

For detailed time-space modeling of PMP system performance, rain data are required as the input parameter for the simulation tool. The input rain rate distributions in space and time can either be chosen from a predefined rain cell model or from meteoradar data. The rain event is defined as a time sequence of rain rates set out in a grid over a selected area.

Each link between the BS and the TS is then simulated separately in each time step. Only the path loss calculation was used

Manuscript received January 26, 2006; revised June 30, 2006. This work was supported in part by the Czech Ministry of Education, Youth and Sports within the framework of the MSM 6840770014 project and in part by the Czech Science Foundation under Grant 102/04/2153.

The authors are with the Department of Electromagnetic Field, Czech Technical University in Prague, Prague CZ-16627, Czech Republic (e-mail: zvanove@fel.cvut.cz; pechac@fel.cvut.cz).

Digital Object Identifier 10.1109/TAP.2006.886529

for the simulation results presented in this paper. The rain attenuation was the only time variant component of the power balance. The rain attenuation  $A$  of each link within the area with a given rain rate distribution  $R(x)$  along the path is determined as

$$A = \int_0^L kR(x)^\alpha dx \quad (1)$$

where  $L$  is the path length and  $k, \alpha$  are coefficients given by ITU-R P.530 [5].

When a rain event is simulated as a time series of rain rate distribution in space, various system characteristics can be modeled: coverage, interference and site diversity improvements in complex PMP system deployment. The specific output can then be generated as a function of time or in the form of overall statistics. In this way, system performance can be studied against different rain events, system parameters, network topology, etc.

### B. Radar Rainfall Database

Radar-based rain rate data [6] were utilized as the input for the PMP system simulations. Data were taken from a modern weather radar network (CZRAD) consisting of two state-of-the-art Doppler C-band weather radars, which cover the entire area of the Czech Republic with volume scans of up to 256 km in range [7]. Radar images for areas with dimensions of  $50 \times 50$  km were adopted. Most of the significant rain events as well as the typical city build-up area were smaller than 50 km in extent. Stratiform rains exceeding this range could be observed, although few of them had a maximum rain rate of more than 3 mm/h [8].

Every radar rain scan can be described using the spatial structure of reflectivity  $Z$  or as recalculated rain rate levels  $R$ . There are several methods of obtaining the rain rate from the reflectivity, all of which give different results [9], especially in millimeter wave band. The method from [6], based on Marshal–Palmer relationship [10]

$$Z = 10 \log(200 \cdot R^{1.6}) \quad (2)$$

was adopted for converting reflectivity  $Z$  (dBZ) to rain rate values  $R$  (mm/h).

A large rain event database, containing over 1.5 million radar images for the Czech Republic for the period 2002–2004, was created for the simulations. Each rain event was represented by a sequence of radar images over a  $50 \text{ km} \times 50 \text{ km}$  area with a 1 km grid resolution in 1-minute steps. Since several aspects of the rain can be analyzed, the rain data was sorted according to two criteria.

- Rain database A — significant rain events (rainstorms) were identified in radar data from the whole region throughout the entire period. Each event was defined as a time sequence of radar images where the maximum rain rate within the  $50 \times 50$  km area was continuously higher than 0.1 mm/h and reached a value of at least 50 mm/h in a single time step. As each event has its own spatial and time evolution, the database was used to develop and test rain spatial classification methods on various rainstorm types.

- Rain database B—for selected locations the data were collected for the whole of 2002. Annual as well as monthly statistics of various rain parameters can be derived from these datasets.

### C. Rain Cell Models

The representation of the temporal and spatial variability of a rain event is a complex problem. Where the rainfall radar data are not available, rain cell models can be utilized as an alternative. Various approaches have been developed and tested. Rain cell models, valid in a given climatic area, are usually derived from long-term rain attenuation measurements and radar data observations. Authors usually divide the rain cell population into two groups: stratiform cells, characterized by a slow decay of the rain rate from its maximum (where a rate of less than 10 mm/h is usually selected), and convective cells, generating an area of heavy rain with rain rates higher than 10 mm/h.

A convective cell is usually surrounded by a stratiform area where the rain rate is weaker and the simplest models only simulate a single rain cell. More frequently, convective cells alone are modeled with cylindrical [11], Gaussian [12] or exponential [13] rain rate distribution using rotational symmetry. The Assis-Einflot model [14] describes rain utilizing stratiform and convective areas with two constant rain rate levels. More sophisticated rain cell modeling using the HYCELL model [15] depicts rain structure descending from the surrounding, exponentially stratiform area to a Gaussian convective rain center with an elliptical horizontal rain cell shape.

Almost all of the models listed above can only be utilized for simulations within a limited area. For simulations in a mid scale area (up to  $50 \text{ km} \times 50 \text{ km}$ ) knowledge of the simple rain cell statistics is inconvenient since it is likely that more than one rain cell will occur. Only sophisticated rain cell models [15] are able to generate several moving rain cells over a wide area.

### D. Site Diversity

The object of this paper was to classify the spatial properties of rainfalls in terms of their impact on PMP system performance. That is why site diversity, which exploits the nonuniform spatial distribution of rain rates, was selected as a system aspect to investigate the influence of rain spatial properties on PMP systems. Typically, the site diversity configuration utilizes two BSs: the main BS (the BS nearest to a TS) and a diversity BS. In general, the angular separation between the links to the BSs can range from 0 to 360 degrees; the maximum distance to a BS from a TS in a millimeter wave system can be up to about 6 km [16].

The diversity gain concept is generally used for diversity evaluations. It is defined as the attenuation difference between the main and diversity links. Many research activities have been carried out into earth-space diversity [17], [18] but there have been noticeably fewer works dealing with site diversity in terrestrial millimeter wave systems. The angular and distant dependant characteristics of the diversity gain were measured and studied in [19], [2], [4], [20]. Nevertheless, only two links with a single TS (i.e., the common point of the links) having a variable angle separation and distance to this hypothetical TS were studied.

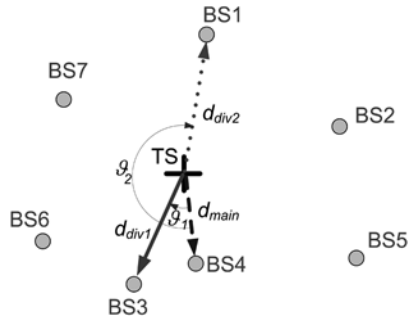


Fig. 1. Selection of diversity base station (dashed line - main link, solid line—the shortest diversity link, dotted line—link with maximum angular separation); TS—terminal station, BS—base stations.

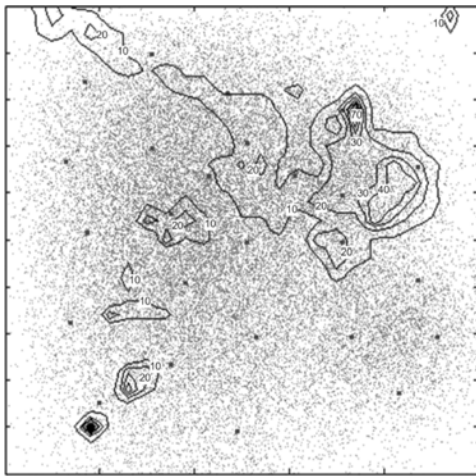


Fig. 2. Specific system deployment in a 50 km  $\times$  50 km area (small points—terminal stations, bold points — base stations) and rain rate spatial distribution during a rain event (rain rate contours from 10 to 70 mm/h in 10 mm/h steps).

A different approach is presented in this paper. Rather than only analyzing two links, the PMP system performance (many simultaneous diversity links) was simulated as a whole under specific conditions, both in time and space, within a defined area [21]. In this way, the rain spatial influence could be properly considered for the whole area. As an example, simulation of a specific PMP network (deployed in a 50 km  $\times$  50 km area) during a selected strong convective rainfall event from Rain database A is illustrated in Figs. 2 and 3. Network topology in the middle of the rain event is demonstrated in Fig. 2. Three very simple site diversity schemes were then tested: D1—no diversity link (TS without the site diversity— $d_{main}$  in Fig. 1). D2 (distance)—a diversity link selected based on the shortest distance ( $d_{div1}$  in Fig. 1). D2 (angle)—a diversity link selected based on the maximum angular separation ( $d_{div2}$  in Fig. 1).

The system outages (percentage of TSs throughout the network having a received power level below the threshold due to rain attenuation) as a function of time are shown in Fig. 3. The system parameters were set as follows [16]: frequency 42 GHz, transmitter power 15 dBm, base station antenna gain 24 dBi, terminal station antenna gain 36 dBi, receiver threshold  $-73$  dBm for 16-QAM with a bit error rate (BER) of  $10^{-6}$ .

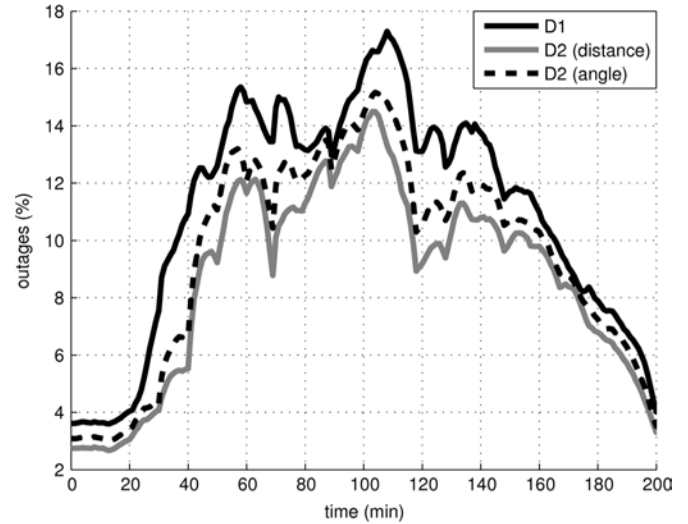


Fig. 3. System outages during a rain event; D1—no site diversity used; D2 (distance)—the nearest available BS is selected for the site diversity; D2 (angle)—the diversity BS is selected according to the maximum angular separation in azimuth.

### E. Outage Improvements

During the next stage a single parameter — the outage improvement probability—was defined to examine the influence of rainfall on the whole PMP system in given area. The outage improvement probability is defined as the percentage of TSs with a successfully established diversity link out of the total number of TSs receiving a level of power input from the nearest BS falling below the threshold due to rainfall. To obtain the outage improvement statistics, simulations of system performance during rain events were performed [21].

As was proved during site diversity simulations [3], when analyzing the site diversity techniques under various network topologies, the rainfall spatial influence is very sensitive to both the density of BS deployment and the particular BS location during a rain event. To study the rain spatial influence on the PMP system independently of the specific network deployment, the following method was used to obtain site diversity for specific spatial distributions. For each rainfall radar scan, the position of a hypothetical TS was changed on 1 km step grid throughout the whole area. The position of the main BS was changed to create a circle around the TS with a fixed radius. The received signal strength was calculated for every azimuth of the hypothetical main link. If the signal strength dropped below the chosen threshold, the diversity links to hypothetical diversity BSs for angular separations ranging from 1 to 359 degrees and diversity link lengths ranging from 1 to 6 kilometers were investigated. As a result of these simulations, a dataset representing the dependence of the outage improvement probability on angle separation and a ratio of the main and diversity link lengths were derived for each radar image.

During the next stage we tried to find a closed analytical expression for outage improvement probability as a function of the angular separation and the link length ratio. Initially we tried to use and modify the Usman–Willis–Watson empirical model [20]. However, this was unsuccessful because the model was

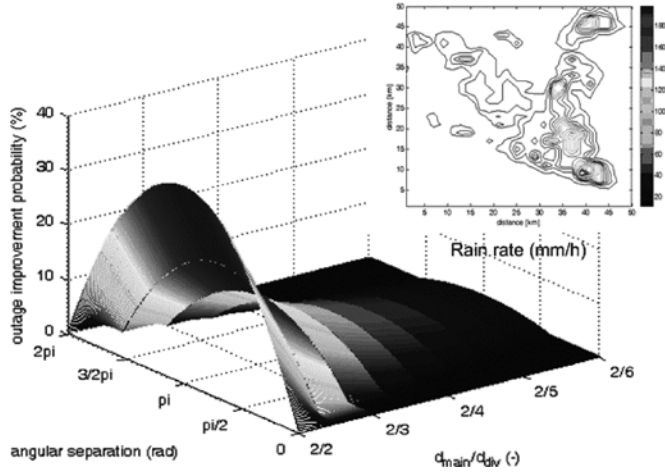


Fig. 4. Calculated outage improvement probability for a rain fade margin of 17 dB using (3).

developed for a diversity gain of two links while our outage improvement probability involved the whole area. That is why a new expression was derived using both intuition and Matlab fitting algorithms. The outage improvement probability  $P(\%)$  is a function of angle separation  $\vartheta$  (rad) (oriented clockwise between the main and diversity link from 0 to  $2\pi$ ) and the ratio of the main and diversity link lengths  $d_{\text{main}}/d_{\text{div}}$  (see Fig. 1)

$$P = a_{\text{const}} \cdot \left( 1 - \left( \frac{\vartheta - \pi}{\pi - b_{\text{const}} \sqrt{1 - \frac{d_{\text{main}}}{d_{\text{div}}}}} \right)^2 \right) \cdot \left( \frac{d_{\text{main}}}{d_{\text{div}}} \right)^{c_{\text{const}}} \quad (3)$$

Specific values for empirical parameters  $a_{\text{const}}$ ,  $b_{\text{const}}$ ,  $c_{\text{const}}$ , were obtained for every radar scan as the best fit of (3) to simulation results using genetic algorithms [21]. The outage improvement probability statistics calculated by (3) using a fade margin of 17 dB for a particular rain rate spatial distribution is demonstrated in Fig. 4.

In the next stage, the specific relationships between the three empirical parameters of (3) and the corresponding radar image were investigated. The parameter  $a_{\text{const}}$  was determined to be particularly dependent on the maximum rain rate  $R_{\text{MAX}}$  taken from the whole rainfall radar scan and, moreover, on the rain fade margin  $P_{\text{MARG}}$  set in the system. This is obvious from Fig. 5, where the dependence of parameter  $a_{\text{const}}$  on the maximum rain rate and the fade margin is depicted. The relationship can be expressed by the following:

$$a_{\text{const}} = a_1 + a_2 \cdot P_{\text{MARG}} - R_{\text{MAX}} \quad (4)$$

where  $a_1 = 110.64$  and  $a_2 = 2.14$  were derived from the radar and simulated data. The constants in (4) and similarly in the following sections are due to their empirical derivation (fitting the analyzed data) given without physical units.

Parameters  $b_{\text{const}}$ ,  $c_{\text{const}}$  are rain rate spatial distribution-dependent. The influence of the rainfall spatial distribution on

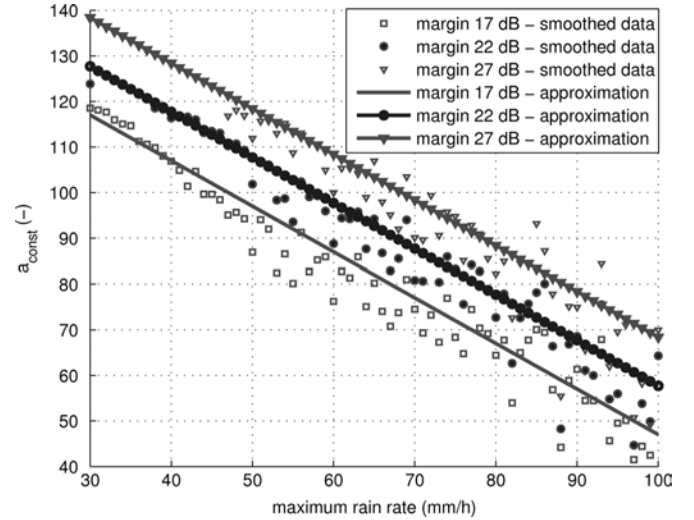


Fig. 5. Dependence of parameter  $a_{\text{const}}$  on the maximum rain rate and fade margins.

these two parameters and consequently the rain spatial classification are dealt with in the following sections.

### III. RAIN SPATIAL CLASSIFICATION

#### A. Rainfall Spatial Parameter

The main aim of this work was to describe rain spatial distribution using a limited number of parameters. Moreover, the classification should be related to PMP system performance utilizing site diversity. Therefore, the dependence of the empirical parameters from (3) on the spatial variation of the rain rate over time was analyzed.

Since the first parameter in (3)  $a_{\text{const}}$  is dependent on the maximum rain rate, during the first stage every radar scan was normalized by dividing the rain rates by the maximum rain rate value of the scan. The cumulative distribution functions (CDFs) of the maximum rain rate calculated over the total (rainy and nonrainy) period from three different locations in the Czech Republic — location A, location B (100 km west and 100 km south of A), and location C (50 km east and 50 km south of A) — during 2002 are depicted in Fig. 6.

After eliminating the maximum rain rate influence, an efficient way of describing the rain rate spatial distribution was sought. Rainfall spatial models seem to be either too simple to characterize mid scale areas or, on the contrary, too complex, with numerous input parameters.

Initially, an approach based on the Fourier transformation applied to space variations of the rain rate [8] was investigated. The spatial spectrum of the rain rate and particularly the dominant power low segments (slopes) in the power spectrum are used to describe the parameters of the rainfall in [8]. The slope determines whether the rain distribution is larger or smaller than the energy input scale. Unfortunately, an analysis of this approach showed that simply dividing the rain scans into two slope types does not fully cover all changes in system outages during a rain event. The influence of rainfalls with higher peak rain rates on the PMP system has also been found to be dependent on the rain

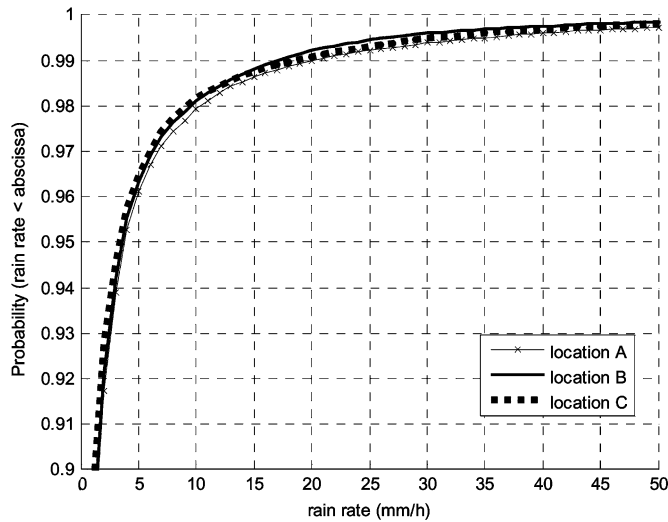


Fig. 6. Cumulative distribution function of maximum rain rate during 2002.

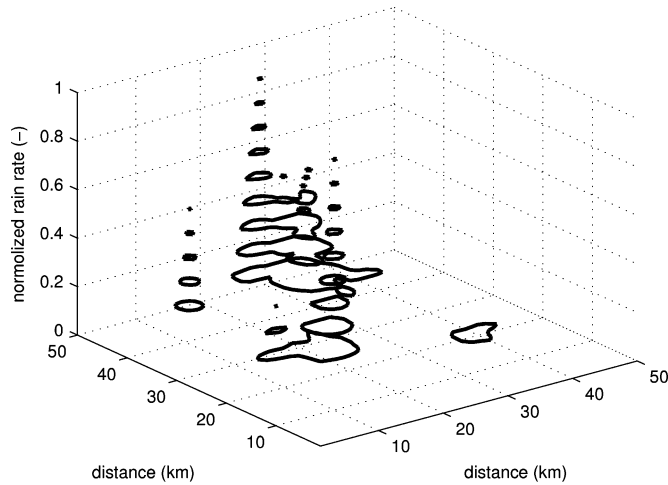


Fig. 7. Normalized rain rate—decomposition to contour levels from 0.1 to 0.9.

cell areas; however, this cannot be fully spanned by enumerating the rain spectra slope.

Another tested approach was to describe the spatial rain rate distribution via the area-averaged rain rate according to ITU-R P.1410 [4]. It was observed that the variation of parameter  $c_{\text{const}}$  cannot be unambiguously expressed as a function of the area-averaged rain rate as some of the spatial features of rainfalls influencing the PMP system performance within the defined area are suppressed by averaging them. Sometimes spatially small rain cells with high rain rates (convective rain storms) can scarcely be distinguished from widely spread low rain rates (stratiform rainfalls).

Finally, a new concept was introduced. To maintain the spatial description, three-dimensional contours of every normalized rain rate scan were determined for levels ranging from 0.1 to 0.9 (Fig. 7). Subsequently, the dependencies of parameter  $c_{\text{const}}$  on several features of the normalized rain rate contours were investigated.

The result of the analyses is as follows: only a single parameter that fully describes rain rate spatial distribution is sufficient

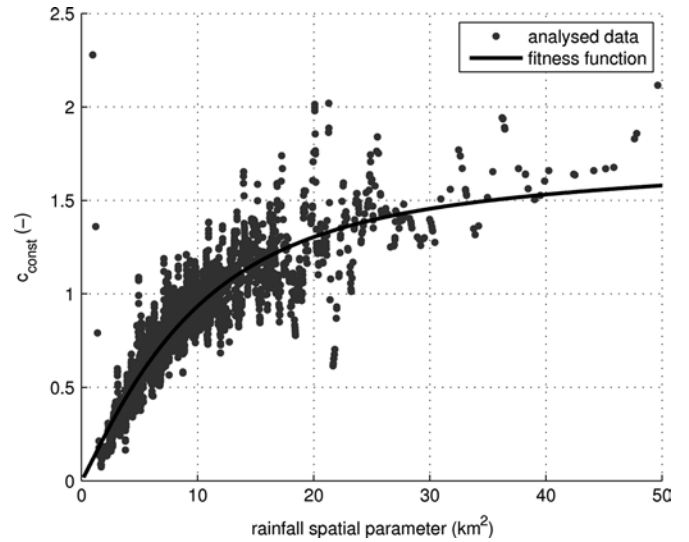


Fig. 8. Dependence of parameter  $c_{\text{const}}$  on the rainfall spatial parameter.

to derive parameter  $c_{\text{const}}$ . The new rainfall spatial parameter is expressed as the average area of the rain cell, taking into consideration all 9 contour levels (ranging from 0.1 to 0.9 of normalized rain rate). To assess its value for a particular rain scan, the average areas of the rain cell have first to be derived for each contour threshold by dividing the total rain-occupied area by the number of rain cells. Thereafter, the resulting value of the rainfall spatial parameter can be obtained as the mean value of the average rain cell areas for all contour levels. Simulations proved that even so the rainfall spatial parameter does not exhaustively describe the distribution of rain cells in a specific region, it does, however, sufficiently characterize rain spatial distribution for site diversity improvement planning issues in the case of PMP systems. Both the rain cell sizes as well as the rain rate slopes are considered.

The number of contour levels was selected on the basis of a trade-off between the simplicity of the procedure and its ability to encompass the rain rate spatial distribution. For cells situated on border of the specified area, the border forms part of the contour misshaping the cell. Provided the area is large enough, this error is negligible (this will be discussed further below).

Dependence of parameter  $c_{\text{const}}$  on the rainfall spatial parameter is depicted in Fig. 8. As can be clearly seen, the parameter  $c_{\text{const}}$  rapidly increases with smaller rainfall spatial parameters and then (around  $20 \text{ km}^2$ ) begins to converge. This behavior can be expressed by

$$c_{\text{const}} = S^{c_1} \cdot (1 - \exp(-c_1 \cdot S)) \quad (5)$$

where  $S \text{ (km}^2\text{)}$  is the rainfall spatial parameter describing the rain rate spatial distribution. The constant  $c_1 = 0.12$  was obtained by a curve fitting algorithm using genetic optimization algorithms. The last spatial dependent parameter in (3)  $b_{\text{const}}$  has been derived as a function of  $c_{\text{const}}$

$$b_{\text{const}} = \pi/4 - \exp(b_1 \cdot c_{\text{const}}) \quad (6)$$

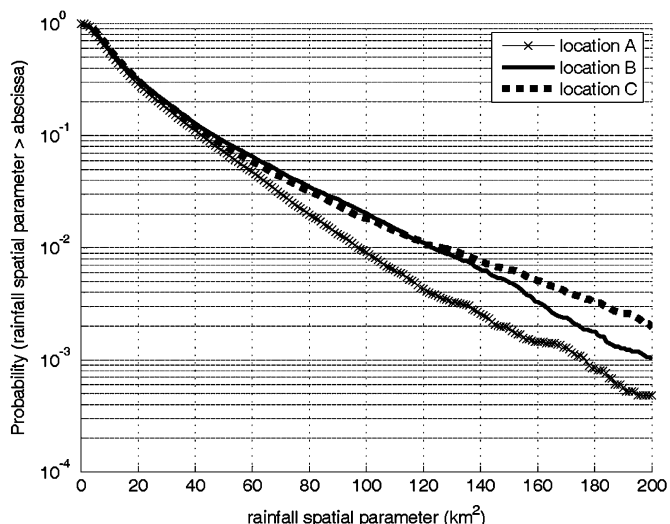


Fig. 9. CDFs of the rainfall spatial parameter conditioned to the rainy time.

where constant  $b_1 = 1.38$  was also obtained by a curve fitting algorithm.

Fig. 9 shows CDFs of the rainfall spatial parameter conditioned to the rainy time (when the maximum rain rate within the area is higher than 3 mm/h). Rain database B was utilized to derive the results for three different locations in the Czech Republic. The rainfall spatial parameter has a lognormal distribution in each of the locations. It was observed that there is no significant difference between cumulative distributions of the rainfall spatial parameter taken from different locations inside this particular climatic area. In the same way, the maximum rain rate statistics in Fig. 6 have similar cumulative distributions. The discrepancies arising in the lower percentages of time are probably caused by the fact that the dataset is statistically limited to a single year. Moreover, the maximum rain rate in a given area is almost independent of the rainfall spatial parameter. The correlation coefficient between the maximum rain rate and the rainfall spatial parameter was enumerated as 0.2, which proves the effectiveness of determining the rain rate spatial distribution using these two independent parameters.

### B. Example

The following example will clearly illustrate the usage of the rainfall spatial parameter to determine improvements in outages of the PMP system.

Let us assume that we would like to compare the system performance during two different typical rain events, R1 and R2 (the rain rate spatial distributions in Fig. 10). Rain fade margins of 10 dB are considered in the virtual PMP system. Maximum rain rates of 60 mm/h and 56 mm/h can be derived from the rain rate distributions R1 and R2, respectively. After normalization of the radar scans by the maximum rain rates and disassembling into nine rain rate levels, the rainfall spatial parameters of 23.4 km<sup>2</sup> and 8.2 km<sup>2</sup> respectively are obtained. Based on these two rain characteristics and on the given system parameter (the rain fade margin), the outage improvement probabilities can be further enumerated by utilizing (3). Provided that the angular separation of 180 degrees and the main to diversity link length ratio

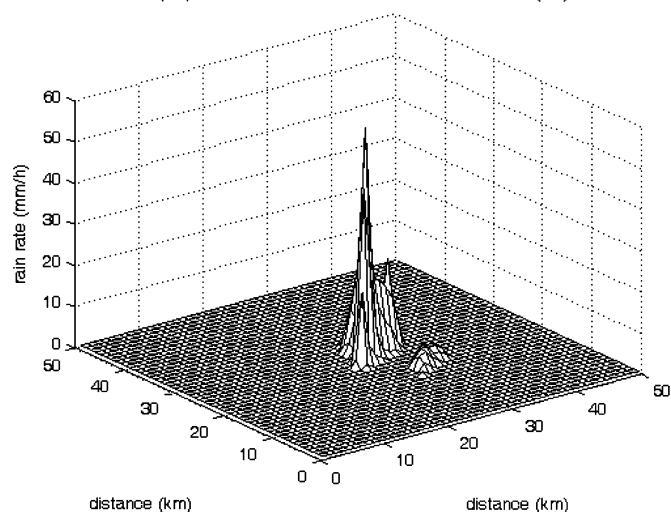
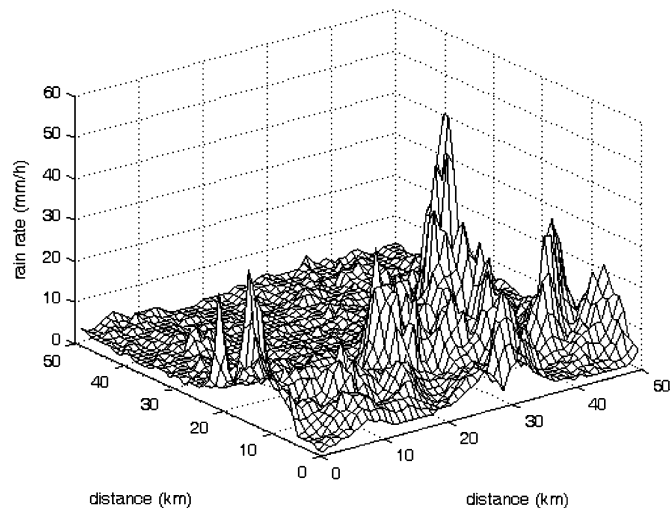


Fig. 10. Analyzed rain rate distributions R1 and R2.

of 2/4 is included in our system, outage improvements of 27.9% and 43.2% respectively can be attained using the site diversity in the PMP systems affected by R1 and R2.

As expected, it can be clearly concluded that the PMP system utilizing site diversity copes better with rain events that are described by the smaller rainfall spatial parameter. This appears more straightforward in the example since both rain distributions have similar maximum rain rates. It is different when compared to classical rain attenuation models for point-to-point links, which only consider a single rain rate value (usually the only one distinguishable parameter from the rain gauge measurements [22]). These models would incorrectly predict that the PMP system accomplishes the same performance during two spatially dissimilar rain events.

Finally, to further develop the example slightly, the influence of stratiform rain on the system will be discussed. For this, the radar scan R3 with the rainfall spatial parameter  $S = 287.7$  km<sup>2</sup> and a maximum rain rate of 32 mm/h was selected (Fig. 11). Assuming the same system settings (a rain fade margin of 10 dB), the outage improvement probability is 26.0% (180 degrees and a 2/4 main to diversity link length ratio). This outage improvement probability is not as low as might be expected when compared to R1. The reason is that the link ranges (up to 6 km)

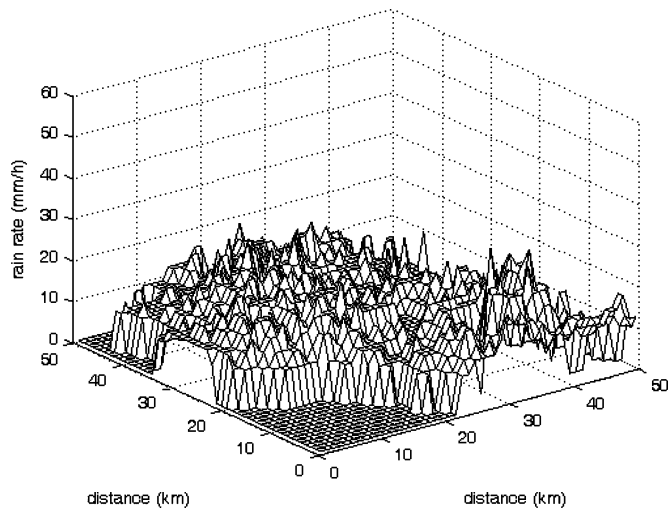


Fig. 11. Analyzed rain rate distributions R3.

are too short when compared to rain cell extent and therefore the site diversity employment cannot be as efficient. Above a certain value of the rainfall spatial parameter, the outage improvement probability starts to converge. This phenomenon can also be clearly distinguished in Fig. 8. The utilization of the site diversity in PMP millimeter wave systems is most efficient for rains having a rainfall spatial parameter of up to  $50 \text{ km}^2$ . From the CDF of the rainfall spatial parameter in Fig. 9 it can be derived that there is a probability of about 92% that these rainfalls will occur during rainy time.

### C. Discussion

It should be emphasized that the results presented introduced a methodology to classify spatial properties of rain events rather than to state fixed figures based on long-term statistics. Let us discuss several points regarding the applicability of the proposed classification method to different contexts and applications.

The method implies that a certain area be under study. As it was mentioned above,  $50 \times 50 \text{ km}$  dimensions were selected on the basis of the proportions of typical rainstorms and urban areas. The dependence of the results on the chosen area dimensions has been analyzed. It was observed that the curve of annual CDF of the rainfall spatial parameter does not change when the area is enlarged beyond a certain limit. The area should be larger than  $30 \times 30 \text{ km}$  in order to negate the influence of area dimensions.

The processing of meteoradar data presented in Section II-B might not necessarily represent the best solution for other regions or radars. In addition, the data should be spatially interpolated to finer resolution from quite coarse radar resolution before deriving the rainfall spatial parameter. If the radar data are not available, sophisticated statistical rain cell models such as the HYCELL model [15] can be utilized, with the help of rain gauge measurements, to generate spatial distributions of rain rates for a particular area.

The annual CDFs for the rainfall spatial parameter in Fig. 9 were obtained for a single region using one-year's data. Statistics for other climatic regions over a longer period of time should

be investigated when the radar data become available. The rainfall spatial parameter can then be used as an effective way to study the differences and scaling of spatial distribution of rainfalls between different regions.

## IV. CONCLUSION

A rain spatial classification method relevant to rainfall influence on PMP radio systems was proposed. Site diversity was utilized to quantify the system performance during rainfalls. A single parameter — the rainfall spatial parameter — is able to characterize the spatial properties of the rain event, in terms of rain cell sizes and rain rate slopes, relating to their impact on the PMP system within a given area. Annual statistics were generated for a typical region in the Czech Republic. If the CDF of the rainfall spatial parameter is added to classical rain rate statistics the individual rain regions can be newly classified. The rainfall spatial parameter offers an effective way to characterize the spatial features of rainfalls for various applications in the field of radiowave propagation.

## REFERENCES

- [1] H. R. Anderson, *Fixed Broadband Wireless System Design*. London, U.K.: Wiley, 2003.
- [2] *Propagation Planning Procedures for LMDS*, 1999, Report from ACTS Project 215—Cellular Radio Access for Broadband Services (CRABS).
- [3] S. Zvanovec and P. Pechac, "Site Diversity Time-Space Simulations for LMDS," presented at the IEEE 60th Vehicular Technology Conf., VTC2004-Fall, Los Angeles, CA, 2004.
- [4] "Propagation data and prediction methods required for design of terrestrial broadband millimetric radio access systems operating in a frequency range about 20–50 GHz," Recommendation ITU-R P.1410 2000, ITU.
- [5] "Propagation data and prediction methods required for the design of terrestrial line-of-sight systems," Recommendation ITU-R P. 530-9 2001, ITU.
- [6] Z. Sokol, "The use of radar and gauge measurements to estimate areal precipitation for several Czech river basins," *Stud. Geophys. Geod.*, vol. 47, pp. 587–604, 2003.
- [7] P. Novak and J. Kracmar, "New data processing in the Czech weather radar network," in *Proc. Eur. Conf. Radar in Meteorology (ERAD)*, 2002, vol. 1, of ERAD Publication Series 328–330.
- [8] R. K. Crane, *Electromagnetic Wave Propagation Through Rain*. London, U.K.: Wiley, 1996.
- [9] S. Yuter, J. Holton, J. Pyle, and J. Curry, "Precipitation radar," in *Encyclopedia of Atmospheric Sciences*. London, U.K.: Academic Press, 2002, pp. 1833–1852.
- [10] J. S. Marshall and W. McK. Palmer, "The distribution of raindrops with size," *J. Meteorology*, vol. 5, pp. 165–166, 1948.
- [11] "Prediction procedure for the evaluation of microwave interference between stations on the surface of the earth at frequencies above about 0.7 GHz," Recommendation ITU-R P.452-11 2003, ITU.
- [12] R. K. Crane, "A local model for the prediction of rain-rate statistics for rain-attenuation models," *IEEE Trans. Antennas Propag.*, vol. 51, no. 9, Sep. 2003.
- [13] C. Capsoni, F. Fedi, and A. Paraboni, "A comprehensive meteorologically oriented methodology for the prediction of wave propagation parameters in telecommunication applications beyond 10 GHz," *Radio Sci.*, vol. 22, pp. 387–292, 1987.
- [14] M. S. Assis and C. M. Einloft, "A simple method for estimating rain attenuation distribution," in *URSI Open Symp.*, La Baule, 1977, p. 301.
- [15] L. Feral, H. Sauvageot, L. Castanet, and J. Lemorton, "Hycell—A new hybrid model of the rain horizontal distribution for propagation studies: 1. Modeling of the rain cell," *Radio Sci.*, vol. 38, no. 3, 2003.
- [16] Broadband Radio Access Networks (BRAN); HIPERACCESS; PHY Protocol Specification 2002–04, ETSI TS 101 999 v1.1.1 Technical Specification.
- [17] Radiowave Propagation Modelling for New Satellite Communication Services at Ku-Band and above — final report COST 255, 2002 [Online]. Available: <http://www.cost255.rl.ac.uk/>

- [18] O. Fiser, "Site diversity gain estimated from rain rate records," *Radio-engineering*, vol. 12, no. 1, Apr. 2003.
- [19] S. M. R. Jones and P. A. Watson, "Attenuation and countermeasures in millimetre-wave point-to-multipoint networks," *Radio Sci.*, vol. 28, no. 6, pp. 1057–1069, 1993.
- [20] I. S. Usman, M. J. Willis, and R. J. Watson, "Route diversity analysis and modelling for millimetre wave point to multi-point systems," presented at the 1st Int. Workshop of COST Action 280, Jul. 2002.
- [21] S. Zvanovec and P. Pechac, "Simulations of site diversity based outage improvements for point-to-multipoint systems in millimeter-wave band," presented at the Wireless Telecommunications Symposium (WTS) 2005, Pomona, 2005.
- [22] V. Kvicera, M. Grabner, and M. Hlavaty, "Rain intensity statistical processing and comparison with ITU-R recommendations," *Radioengineering*, vol. 13, no. 2, pp. 1–2, 2004.



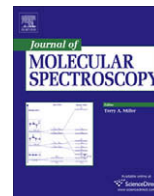
**Stanislav Zvanovec** (M'04) received the M.Sc. degree in electrical engineering and the Ph.D. degree from the Czech Technical University in Prague, Czech Republic, in 2002 and 2006, respectively.

He is now employed by the Department of Electromagnetic Field, Czech Technical University in Prague as a Researcher. His current research interests include electromagnetic wave propagation issues for millimeter wave band systems and a mobile radio propagation channel.



**Pavel Pechac** (M'94–SM'03) received the M.Sc. degree and the Ph.D. degree in radio electronics from the Czech Technical University in Prague, Czech Republic, in 1993 and 1999 respectively.

He is currently an Associate Professor in the Department of Electromagnetic Field at the Czech Technical University in Prague. His research interests are in the field of radiowave propagation and wireless systems.



## The use of the Fabry–Perot interferometer for high resolution microwave spectroscopy

Stanislav Zvánovec<sup>a,\*</sup>, Petr Černý<sup>a</sup>, Petr Piksa<sup>a</sup>, Tomáš Kořínek<sup>a</sup>, Pavel Pechač<sup>a</sup>, Miloš Mazánek<sup>a</sup>, Juraj Varga<sup>b</sup>, Jindřich Koubek<sup>b</sup>, Štěpán Urban<sup>b</sup>

<sup>a</sup> Czech Technical University in Prague, Department of Electromagnetic Field, Technická 2, 166 27, Prague 6, Czech Republic

<sup>b</sup> Institute of Chemical Technology, Department of Analytical Chemistry, Technická 5, 166 28 Prague 6, Czech Republic

### ARTICLE INFO

#### Article history:

Received 20 January 2009

In revised form 20 March 2009

Available online 10 April 2009

#### Keywords:

Fabry–Perot interferometer

Time domain FTS

Emission microwave spectroscopy

### ABSTRACT

A simple Fabry–Perot interferometer was used for measurements of microwave spectra. Both basic experimental arrangements, absorption and emission, were tested on the rotational spectra of acetone-trile. The interferometric results obtained were compared with the spectra measured using a standard high resolution microwave spectrometer.

© 2009 Elsevier Inc. All rights reserved.

## 1. Introduction

Spectral resolution and intensity sensitivity are crucial quality parameters for any spectrometer. The need for high sensitivity increases especially as the transition frequencies go down in the case of high resolution microwave spectroscopy where the line intensities vanish along with the decreasing difference of the level populations between the lower and upper states of transitions.

The standard experimental conditions of high resolution spectroscopy, such as very low sample pressure, are a hindrance to a standard absorption experiment, because the low pressure reduces the collision relaxation processes and the relaxation by spontaneous emission falls by the third power of frequency [1]. It means that the saturation of the transitions (i.e. the equalizing of level populations) represents the main restrictions for the low frequency ( $\sim \nu < 80$  GHz) high resolution absorption spectroscopy.

The Fabry–Perot interferometer provides an interesting tool enabling an enhancement of the sensitivity of the absorption as well as emission measurements in microwave spectroscopy. For monochromatic radiation, the Fabry–Perot interferometer can be tuned to a resonance at which the constructive interference of the multiple-reflected electromagnetic waves enables to accumulate the radiative energy. From the spectroscopic point of view, the resonator behaves as a cell with a long effective absorption path or a powerful emission source. The enhancement of the sensitivity of the Fabry–Perot resonator corresponds to its high quality factor. The

main purpose of this paper is to present both the absorption and emission measurements based on the Fabry–Perot resonator (see Fig. 1).

The paper describes the simple applications of the Fabry–Perot interferometer in both absorption and emission microwave high resolution spectroscopy. First, the use of the Fabry–Perot resonator for absorption measurements is discussed. The applications of the Fabry–Perot resonator for microwave Fourier transform spectroscopy measurement of molecular emissions after an excitation by an electromagnetic field pulse are also presented. All these interferometric measurements are compared with the analogous spectra measured with the Prague mm-wave high resolution spectrometer [2].

## 2. The Fabry–Perot interferometer setup

The Fabry–Perot interferometer (resonator) used for our measurements comprises a tube-shaped cavity with a length of 0.55 m made from stainless steel with an inner diameter of 0.16 m, especially-designed input and output windows located in the center of the sides of the resonator tube, a pivot coupling dielectric foil placed inside the cavity and two spherical mirrors for setting particular resonances (see Fig. 2). The spherical mirrors have a 0.455 m radius and are made of bronze coated with a  $5 \times 10^{-6}$  m thick golden layer. One of the mirrors is fixed, while the other is movable with a reversible motor, which is suitably geared down in order to provide a fine, automated adjustment of the cavity length with a 0.05- $\mu$ m step. The mirror spacing is tunable from 0.495 to 0.510 m. The resonator setup and electrical field

\* Corresponding author. Fax: +420 233 339 958.

E-mail address: [xzvanove@fel.cvut.cz](mailto:xzvanove@fel.cvut.cz) (S. Zvánovec).

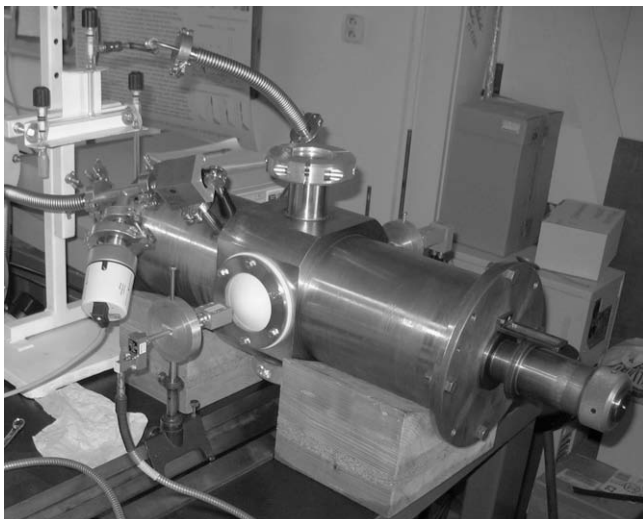


Fig. 1. Fabry-Perot resonator.

intensity distribution inside the resonator cavity are depicted in Fig. 2. A similar setup of the Fabry-Perot resonator with the perpendicular coupling of electromagnetic waves was already introduced by French and Arnold [3] for frequencies around 150 GHz where this setup was used only for absorption measurements. In our paper, we describe potentialities of the Fabry-Perot spectrometer not only for the absorption experiments but above all for the emission measurements in a significantly lower frequency region.

The electromagnetic radiation is pumped into/out of the resonator cavity using a 0.1-mm thick dielectric polyethylene coupling foil from/to the perpendicularly placed feeders and detectors (horn antennas). This pumping is different from the approaches implemented in the common Fabry-Perot resonators, which are usually used for spectroscopic measurements, e.g. [4], where L-shape antennas are mounted in particular positions inside the mirrors. Since the resonator is evacuated, the electromagnetic radiation is coupled into and out of the resonator cavity via special elliptical dielectric lenses placed on the windows. The lenses focus the required radiative energy on/from the coupling foil and form diverging waveforms in the near field region onto the flat uniform far field. Optimization of the parameters of the lenses was inevitable in order to optimize the waveform inside of the resonator and, in this way, to avoid the saturation of the absorbed energy of the gas-

eous sample (resulting from the focusing of the radiative energy). It was necessary to avoid additional undesirable resonances inside of the resonator caused by inner surfaces of lenses (see Ref. [3]), which evokes a dummy increase of the quality factor. The optimal field distribution on the coupling foil and the position of the feeding antenna in front of the lens were also carefully sought [5].

### 3. The absorption arrangement of the Fabry-Perot interferometer

Absorption measurements in the Fabry-Perot interferometer (resonator) are based on the measurement and subsequent evaluation of the quality factors of both the empty as well as the gas-filled resonator. Because we need to reach both as high quality factor of the empty resonator as possible and a suitable coupling to enable this comparison, the other losses inside the resonator cavity have to be minimized. Particularly, the undesirable losses can be caused by the diffraction and reflection of electromagnetic waves at the mirrors and by coupling losses at the coupling foil. The quality factor of the Fabry-Perot resonator is about  $10^5$  throughout the frequency region of our measurements.

The Fabry-Perot interferometer was pumped by the Agilent 8257D microwave synthesizer, whose frequency was doubled using the Wisewave FMP-KF215-01 doubler. The radiation passed through the resonator was detected and analyzed by the Agilent Spectral Analyzer E4440A, whose frequency range was extended up to 50–75 GHz using the external Agilent 11970V harmonic mixer. All of the measurements were automatized by a computer that controlled both the microwave synthesizer as well as the spectrum analyzer via the USB to GPIB interface. The spacing and movement of mirrors were also controlled by means of the USB to RS232 interface. This way, the distance between the mirrors was set precisely for each measured frequency based on the minimal received power of the resonance response curve analyzed by the spectrum analyzer.

The absorption Fabry-Perot setup was tested with acetonitrile spectra. The resolved, partly resolved and unresolved hyperfine structures of the rotational transitions  $J' \leftarrow J'': 3 \leftarrow 2, K = 0, 1, 2$  provide a broad scale of spectral lines from very intense to weak. Acetonitrile is a symmetric top molecule with a large dipole moment ( $\mu = 3.92$  D) and its rotational spectra were studied in details in the Prague laboratory [2]. Fig. 3 involves the comparisons of the acetonitrile spectra measured using the Fabry-Perot resonator as described above and the standard high resolution mw absorption setup with the 5.6 m long optical path with the acetonitrile pres-

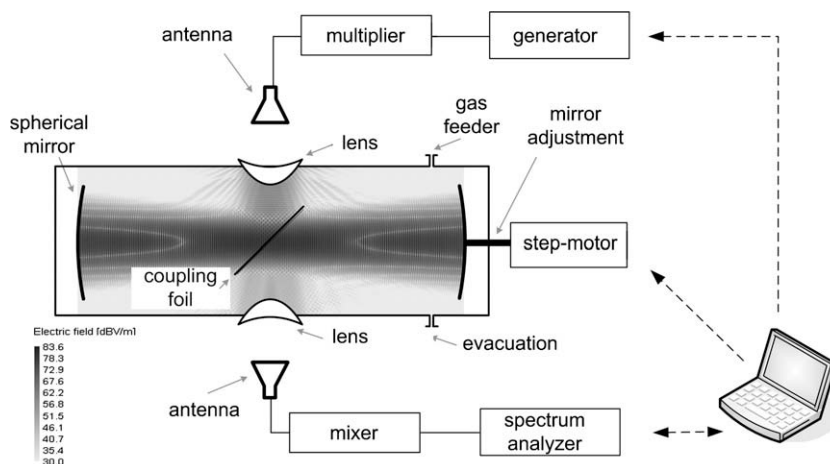


Fig. 2. The Fabry-Perot resonator setup for gas absorption measurements.

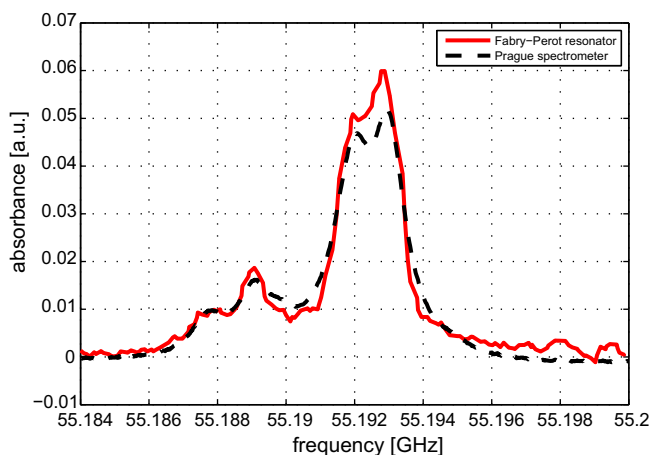


Fig. 3. The measured absorption spectrum of acetonitrile.

sure being roughly 15  $\mu\text{bar}$  [2]. The cavity response width depends on the sample absorption and pressure. In the case of the highly evacuated resonator without a sample absorption, the 0.57 MHz width of the resonance response was measured. On the other hand, the cavity response widths from 0.60 MHz up to 1.23 MHz were observed from weak up to intense absorptions, respectively. It should be mentioned, the method based on the coupling strength [6] was applied to derive the resonator response widths. This approach is different from conventional methods where this parameter is determined according to the 3 dB criterion [3] only.

It is obvious from Fig. 3 that both the measurements provide comparable results within the frequency interval of 50–110 GHz. We believe that the absorption system with the 0.55 m long Fabry–Perot resonator can be used as an alternative to the high resolution spectrometer with the sample cell using a 5.6-m long optical path [2]. It should be emphasized that the measurement of absorption using the Fabry–Perot resonator has its particular advantages as well as disadvantages.

The main advantage of our Fabry–Perot resonator is its relatively higher sensitivity to weak absorptions due to an apparent lengthening of the optical path length by means of multiple reflections. The effective optical path length corresponding to the measured quality factors (according [3]) varies approximately from 40 up to 83 m from the intense absorption up to the evacuated resonator, respectively (see Fig. 3). This holds true especially in cases of standing waves, where the losses caused by destructive interference processes are negligible.

On the other hand, it should be pointed out that this method is time-consuming because each individual point on the frequency scale requires a separate adjustment of the mirrors. It should be also noted that the parameters of the individual parts of the resonator limit the usable frequency range. The main reason for the low frequency cut-off is the diffraction (spilling-over) of electromagnetic waves, which depends, above all, on the size of the mirrors used, their distance and curvature [7], for instance in our case, the low frequency cut-off is about 20 GHz. The coupling losses, which depend on the thickness and quality of the dielectric coupling foil, cause a decrease in the quality factor (i.e. measurement sensitivity) in the direction to higher frequencies.

#### 4. The emission's time domain measurements

As it was mentioned above, very low pressure high resolution absorption spectroscopy collapses at low frequencies because of the transition saturation, which is a consequence of a retardation of the relaxation processes (spontaneous emission, collisions)

causing the equalization of the populations of both levels of the saturated transition. On the other hand, the easy achievement of saturation is an advantage in the time domain emission experiment. In the literature [8–11], there can be found several such experiments, starting with the first time domain emission spectrometer performed by Dicke and Romer [8] in 1950.

Nowadays, probably the best time domain emission microwave Fourier transform (MWFT) spectrometers carry the Grabow signature, e.g. [9], where a spectrometer is constructed for a frequency range 4–18 GHz by using the Fabry–Perot resonator with a perpendicularly-placed pulsed molecular beam. In order to reach an efficient distribution of the standing waves inside this resonator, the pulses of monochromatic electromagnetic radiation are pumped into the cavity through the L-shaped wire hook “antenna” mounted off-axis at one of the mirrors [9]. After the pulse termination, the excited gaseous sample emits microwave radiation that is detected by the same antenna and using a circulator [9] or SPDT PIN diode switch [12,13] led to the down-conversion and processing units. The system has been improved several times [12,13], e.g. by a coaxially-oriented pulsed molecular beam [4] to increase the emission time, by the coaxially-aligned parallel Stark electrodes inside the resonator cavity [10] for dipole moment measurements or by using the cryogenically-cooled (to  $T = 77\text{ K}$ ) resonator [11] to decrease the instrument noise, etc.

Our Fabry–Perot interferometer was analogously used for emission Fourier transform measurements of excited gaseous samples. Obviously, in comparison with the emission experiments mentioned above [12,13], our resonator setup differentiates in several points as listed below. Two horn antennas were used in the system similarly to our absorption measurements. The first antenna pumps radiative energy into the resonator cavity while the other detects the radiative energy emitted from the resonator cavity from the perpendicular direction (see Fig. 4). The measurement setup is significantly simplified in particular in the receiver part. Instead of building a receiver system consisting of several switches (whose time-control has to be very precisely tuned [12,13]) and other components, the source and receiver parts were separated and commercially available instruments (such as the MW synthesizer and the spectrum analyzer with synchronized internal clocks) were used. Rectangular pulses (on-off modulation) for the particular frequency with a definite pulse width were set at the synthesizer with a given repetition rate of 100 Hz. The signal from the synthesizer was doubled by the frequency multiplier. The “zero span” configuration of the spectrum analyzer (the local oscillator of the analyzer does not sweep) was set to measure a time dependence of the received signal. Thus the spectral analyzer was used only as a wideband receiver around the required central frequency. The down-converted signal at the intermediate frequency of 25 MHz was available at the spectrum analyzer output unlike the absorption measurement, and it was consequently amplified and digitized (1024 samples, 100 MSps). For every frequency point, the signal was recorded 1024 times to minimize the undesired noise.

In order to test our emission setup, the acetonitrile spectrum was measured. A typical example of this measurement in the frequency interval between 55.187 and 55.195 GHz with the sample pressure being approximately 6  $\mu\text{bar}$  is presented in this paper, see Figs. 5 and 6. First, it was necessary to determine suitable pulse duration in order to reach the optimal conditions for the excitation of the acetonitrile sample. The time dependences of the received power on the excitation pulse length are depicted in Fig. 5. It was found from detailed analyses of the falling edges of the pulses (see Fig. 5) that the 210 ns durative pulses provide the most appropriate conditions for our emission measurements. Additionally, an analysis of the pulse shape also enabled the optimization of the mirror distance, corresponding to a standing wave at the given fre-

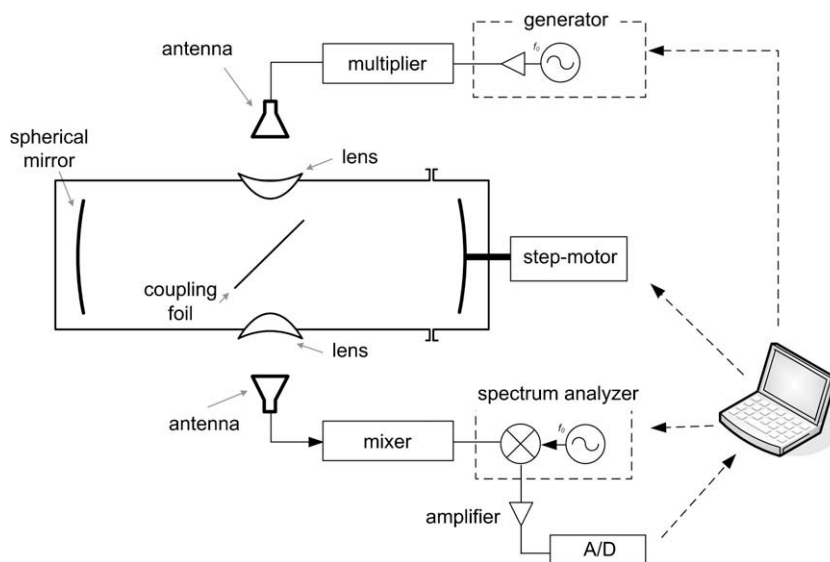


Fig. 4. The setup of the Prague FTMW spectrometer.

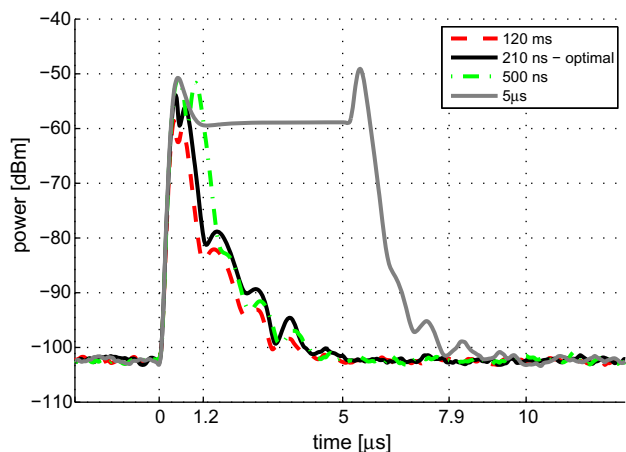


Fig. 5. The measured power for various rectangular excitation impulse lengths.

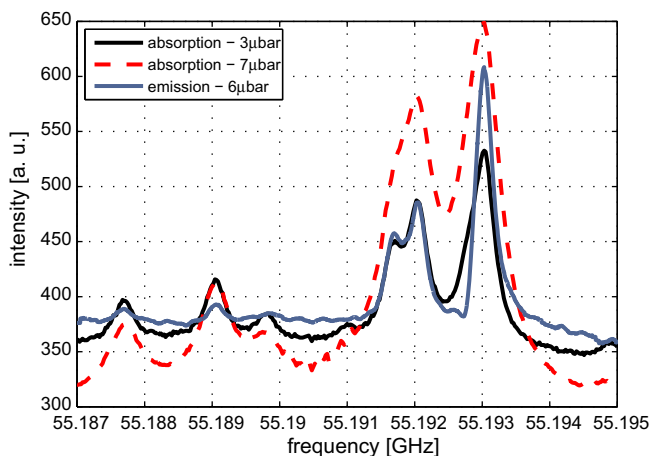


Fig. 6. The emission spectrum of acetonitrile derived from summation of the 2150 kHz wide spectrum intervals as compared with the absorption spectra [2].

in the time dependence of the long duration pulse (e.g. see the time dependence of the 5  $\mu\text{s}$  pulse in Fig. 5).

It was necessary to transform the time domain emission data into the frequency domain. From a detailed analysis of the shapes of the recorded power, it was found that the time interval from 1.2 to 7.9  $\mu\text{s}$  after excitation origin (see Fig. 5) provided the optimal information for the evaluation of the frequency domain spectra. Several approaches to obtain the most appropriate Fourier transformed spectra from the time domain data were tested. For example, the emission can be evaluated either only from the pumping frequency or from an interval around the pumping frequency due to the resonance curve width.

Thus, the spectra were evaluated from the maximum value obtained within the 50 kHz wide frequency intervals around the pumping frequency, as well as from the summation of the entire intervals of the overlapped spectra. The best results were derived from the summation of the spectrum intervals of a width of 2150 kHz (see Fig. 6). The aforementioned results were compared to the spectra measured by the standard high resolution microwave absorption setup with the 5.6 m long optical path [2] at 3 and 7  $\mu\text{bar}$ . It is evident that our emission-measured spectrum in the frequency domain provides a comparable quality with that measured by absorption at a comparable sample pressure (see Fig. 6).

## 5. Conclusions

The above-mentioned examples clearly show that the Fabry-Perot interferometer is an interesting tool with high potential for high resolution microwave spectroscopy. In the absorption setup, the interferometer can be used as a compact cell with a sufficiently long optical path length enabling high-sensitivity measurements. The highest sensitivity is achieved in the resonance arrangements where the interferometer is tuned for each frequency to the constructive interference of the multiple-reflected electromagnetic waves between the mirrors. Such an approach seems to be complicated, but the mirror tuning can easily be computerized. The interferometer absorption system can be considered as an interesting possibility for sensitive, compact analytical instruments for a detection of selected gases with significant absorption in the spectral interval of approximately 50–90 GHz. For lower frequencies, the emission arrangement is obviously more efficient. As was men-

quency. For instance, the optimal mirror distance corresponds to the largest decrease of the plateau between two marginal peaks

tioned above, the near energy levels have very similar populations, which become equal during the absorption experiment under the conditions of high resolution microwave spectroscopy (i.e. very low sample pressure, slow spontaneous emission). We are speaking about the saturation of the absorption transitions which mean another attenuation of the absorption intensities.

The main advantage of emission microwave Fourier time domain spectroscopy is that it utilizes the transition saturation which supports the emission measurements, in contrast to the absorption measurements which collapse due to this saturation.

In this paper, a simplified, very flexible emission experimental arrangement is offered. This simple setup, however, does not as yet make sophisticated measurements in molecular beams or Stark experiments in comparison with the Grabow's complex measurement system possible [10–13]. From the system point of view, the system presented has a huge noise figure and consequently a lower sensitivity due to the very high conversion losses of the harmonic mixer used and due to the absence of a low noise input amplifier. These deficiencies of our setup could be partially neglected in the lower frequency band and partially solved in next step by adding a low noise input amplifier.

Although our simple emission setup does not reach all of the quality parameters of the best time domain spectrometers described in the literature [10–13], our simple setup offers the high compactness and flexibility which can be exploited for the development of simple low frequency microwave instruments for analytical chemistry.

## Acknowledgments

The work was supported through grants from the Ministry of Education, Youth and Sports of the Czech Republic (research programs MSM6046137307 and LC06071), the Grant Agency of the Academy of Sciences of the Czech Republic (IAA400400504), the Czech Science Foundation (GACR 102/08/P346) and the Marie Curie Actions (RTN 512202).

## References

- [1] C.H. Townes, A.L. Schawlow, *Microwave Spectroscopy*, Dover Publications Inc., New York, 1975.
- [2] P. Kania, L. Stříteská, M. Šimečková, Š. Urban, *J. Mol. Struct.* 795 (2006) 209–218.
- [3] I.P. French, T.E. Arnold, *Rev. Sci. Instr.* 38 (1604) (1967) 1604–1607.
- [4] J.U. Grabow, W. Stahl, H. Dreizler, *Rev. Sci. Instrum.* 67 (1996) 4072–4084.
- [5] S. Zvanovec, P. Piksa, P. Cerny, M. Mazanek, P. Pechac, *Second European Conference on Antennas and Propagation EUCAP 2007*, Edinburgh, 2007, pp. 341–342.
- [6] A.P.S. Khanna, *Microwaves & RF* 23 (1984) 81–86.
- [7] A.G. Fox, T. Li, *Bell Syst. Tech. J.* 40 (1961) 453–488.
- [8] R.H. Dicke, R.H. Romer, *Rev. Sci. Instrum.* 26 (1955) 915–928.
- [9] U. Andresen, H. Dreizler, J.U. Grabow, W. Stahl, *Rev. Sci. Instrum.* 61 (1990) 3694–3699.
- [10] M. Schnell, D. Banser, J.U. Grabow, *Rev. Sci. Instrum.* 75 (2004) 2111–2115.
- [11] J.U. Grabow, E.S. Palmer, M.C. McCarthy, P. Thaddeus, *Rev. Sci. Instrum.* 76 (2005) 093106-1–093106-11.
- [12] J.U. Grabow, W. Caminati, in: J. Laane (Ed.), *Frontiers of Molecular Spectroscopy*, Elsevier, 2009, p. 383.
- [13] W. Caminati, J.U. Grabow, in: J. Laane (Ed.), *Frontiers of Molecular Spectroscopy*, Elsevier, 2009.

# UHF RF Identification of People in Indoor and Open Areas

Milan Polívka, *Member, IEEE*, Milan Švanda, *Student Member, IEEE*, Přemysl Hudec, and Stanislav Zvánovec, *Member, IEEE*

**Abstract**—The performance of an ultra-high-frequency RF identification (ID) system operating at 869 MHz, intended for the ID of persons in both indoor and open areas, has been validated using the propagation models, as well as the series of practical measurements. A two-ray propagation model and the 3-D ray-tracing model were used for calculations of all important system parameters in open and indoor areas, respectively. For the application mentioned above, a novel (electrically small and, at the same time, low-profile) wearable TAG antenna was designed. It was used in order to carry out the necessary tests as well. The antenna in question is based on an artificial-like surface. The latter provides an important screening effect and avoids detuning. Another virtue of the surface used is represented by the fact that it ensures the minimum loss of the antenna efficiency (resulting from the presence of a nearby human body). The simulations and measurements show that the optimized system can guarantee a reliable ID at distances up to 9 m in open areas and up to 16 m in corridors.

**Index Terms**—Artificial surface, electrically small antenna, identification (ID) of people, loop antenna, RF identification (RFID) system, TAG antenna.

## I. INTRODUCTION

**T**O DATE, given the growing stress put on security aspects, the identification (ID) systems intended for monitoring of people in both indoor and outdoor areas have become increasingly important. The efficient and reliable tracking of the motion of many people in either large buildings or outdoor areas belongs to the relatively difficult tasks. Standard monitoring-ID systems, working in either low-frequency (LF) or high-frequency (HF) bands (125 kHz, 13.56 MHz), which are based on inductive coupling, suffer from a low read distance (i.e., typically up to 1 m [1]). Therefore, during the ID process, the person has to, more or less, touch the reader or even insert

the ID card into the reader. This requires the installation of relatively narrow gates, where anyone that intends to pass through the gate, is obliged to stop and activate the reader. This kind of ID process is, in general, inconvenient and time consuming. Furthermore, in cases of heavy traffic or multiple accesses, it gives rise to unacceptable time delays.

As a result, RF identification (RFID) systems operating at either ultra-high-frequency (UHF) or microwave frequencies (i.e., at 860–930 MHz or 2.4 GHz) that use electromagnetic wave propagation as a coupling mechanism seem to be more suitable than inductive coupling systems. It is possible to monitor and identify persons at moderate distances, usually over several meters. In addition, the persons that are being monitored are not required to perform any action during the ID process. The monitoring and ID processes do not have any negative repercussions on the fluency of the traffic; in fact, people can even move rather quickly. Such ID systems can be used in manufacturing plants, offices, warehouses, prisons, etc. A specific application of the UHF RFID system, consisting of the ID of sportsmen in mass races, is described in [2].

The performance of any UHF or microwave RFID system is dominantly influenced by the parameters of antennas used and also by the propagation of electromagnetic waves in the intended ID area. This paper is focused on the ID of people in open areas and inside buildings (especially in corridors). The objective is to reach as high a read distance as possible. To handle the RF ID task exactly, the evaluation of the electromagnetic field coverage in the treated area is required.

Usually there is not much space for raising the gain of the reader antennas. High-gain antennas are relatively large and can show too narrow radiation patterns. Due to this, the parameters of TAG antennas are of prime importance. Since their dimensions must be small, while their radiation patterns are required to be wide, it is necessary to optimize their efficiency in order to ensure a long read distance. This is especially important in case of wearable antennas because their parameters can be strongly influenced by the close vicinity of a human body. The new dual-loop antenna designed for the ID of people, presented here, employs a special screening substrate that preserves the acceptable antenna efficiency while guaranteeing a high immunity against the influence of the human body.

The propagation of electromagnetic waves substantially differs in open areas and inside the buildings. In open spaces, it is usually accurate to take into account only the first reflection from the ground. Owing to this, a relatively simple analytical propagation model can be used. On the contrary, in case of indoor applications, the multiple reflections from many walls,

Manuscript received June 09, 2008; revised October 26, 2008. First published April 14, 2009; current version published May 06, 2009. This work was supported in part by the Czech Science Foundation under Project 102/08/1282: “Artificial electromagnetic structures for miniaturization of high-frequency and microwave radiation and circuit elements” and Project 102/08/H018: “Modeling and simulation of fields,” by the Czech Ministry of Education, Youth and Sports under the “Research in the Area of the Prospective Information and Navigation Technologies” MSM 6840770014 and “Research of Methods and Systems for Measurement of Physical Quantities and Measured Data Processing” MSM6840770015 research programs and under COST Project IC0603.

The authors are with the Faculty of Electrical Engineering, Department of Electromagnetic Fields, Czech Technical University, 16627 Prague 6, Czech Republic (e-mail: polivka@fel.cvut.cz; svandm1@fel.cvut.cz; hudecp@fel.cvut.cz; zvanovec@fel.cvut.cz).

Color versions of one or more of the figures in this paper are available online at <http://ieeexplore.ieee.org>.

Digital Object Identifier 10.1109/TMTT.2009.2017305

TABLE I  
Standard UHF RFID System Parameters (From Trolley Scan<sup>1</sup>)

System components	Parameter	Values
Reader	Operating frequency (Europe)	869.5 to 869.7 MHz
	Transmitted power	24.7 dBm to 36.0 dBm
	Receiver sensitivity	-64 dBm (200 pW)
	Identification rate	70 s <sup>-1</sup>
Transponder (TAG)	Reader antenna gain	8.0 dBi
	Chip sensitivity	-6.9 dBm (200 μW)
	Chip impedance (measured value)	76 - j340 Ω
	TAG conversion loss	approx. 20 dB

floors, ceilings, windows, doors, and bigger pieces of furniture must be taken into account. In order to provide a satisfactory agreement between the simulation and the practical measurements carried out in corridors, the ray-tracing methods were used in this paper.

## II. RFID SYSTEM DESCRIPTION

### A. RFID System Parameters

The standard commercial RFID system (see Table I) and Trolley Scan<sup>1</sup> were used for the evaluation of the read distance, as well as the reliability of a person's ID in buildings and open areas.

For the given purposes, it might seem beneficial to use RFID systems operating in the microwave band of 2.45 GHz. This can lead to a considerably easier design of small and efficient antennas. However, the flip side is that the use of the aforementioned frequency results in the propagation loss that is higher by at least 9 dB in both radio paths. The employment of UHF systems for a long-distance ID of people stills represents a very good choice then.

### B. Novel TAG Antenna

The degradation of the TAG antenna performance in the close vicinity of a human body belongs to the problems that are to be solved when considering the UHF or microwave RFID of people. The body can be treated as a high-loss dielectric object with a relative permittivity  $\epsilon_r \sim 50$ –60 and a loss tangent  $\tan\delta \sim 0.5$ –1.2 [3]. In case of the standard dipole-type TAG antennas, the presence of such dielectric objects causes significant detuning of the antenna and also the absorption of the radiated or received energy [4]–[7]. This results in a low radiation efficiency and, consequently, in a short read distance. Thus, the antenna structures that are immune to the influence of a human body turn out to be advantageous for the intended purposes.

In order to obtain the required immunity, it is, in general, necessary to insert a metallic plate (or a similar screening layer) between the radiating element and the human body. The metallic plate can act as an additional screening plane or can become an inherent part of the antenna structure. The former solution is usually represented by dipole- or loop-type antennas, while

the patch antenna and planar inverted F antenna (PIFA) [8], [9] usually represent the latter case. A simple addition of the metallic plane to an antenna structure can lead to a substantial drop in both the antenna impedance and antenna efficiency. In the open literature, several papers, which solve the above-mentioned problem by adding a distance spacer (e.g., [10]–[13]) or by the application of artificial magnetic surfaces (e.g., [14]) have been published.

The application of folded or multiarm-folded dipoles (described in [15]) can be considered as an alternative solution. This approach raises the impedance of the antenna working above the close metallic plane. These structures can provide an extremely low profile (even below the relative wavelength height  $h/\lambda_0 < 0.01$ ) and, at the same time, maintain the radiation efficiency on a reasonable level (over 50%). Nevertheless, the relatively large footprint dimensions (comparable to the half-wavelength) can be unsatisfactory for many RFID applications.

The employment of the patch-type antennas, where a metallic ground plane is an inherent part of the antenna structure, represents other possible approach. Nonetheless, it is necessary to take into account that the radiation efficiency of these antennas decreases significantly in case that the height of the substrate is lower than approximately  $0.02\lambda_0$  [16] (it equals approximately 6–7 mm in the UHF band). For wearable TAG antennas, this height can be unacceptable. The same difficulties can result from the antenna length, which corresponds to a half- or quarter-wavelength (approximately 160–170 or 80–85 mm in the UHF band).

Artificial magnetic surfaces [10] used for constructive summation of the contributions of source and mirror currents to the radiation seem to be suitable for screening carried out near the human body. Nevertheless, due to the necessity to manufacture the shunt inductive components with a height of several millimeters in the UHF band [17], their implementation, to date, does not allow to construct antennas with very low profiles ( $h/\lambda_0 < 0.01$ ).

In order to identify people, a novel flat electrically small dual-loop antenna was designed and manufactured (see Fig. 1). It is loaded by a planar array of four sub-wavelength patches that are placed closely over a grounded dielectric slab. A more detailed description can be found in [18]. The patch array is similar to the structure of high-impedance surfaces and suppresses the radiation of mirror currents. This provides a very high immunity against the influence of a nearby human body while preserving the acceptable antenna efficiency (see Table II).

The measured radiation pattern of the loop antenna, fed by the coaxial cable, shows an approximate 15° tilt that is caused by the nonperfect symmetrization (see Fig. 2). It is not expected that this tilt could be present in case of the TAG antenna-chip connection.

The new antenna is planar; its total size (including the patch array) is equal to  $70 \times 105 \times 1.82$  mm (relative size is  $0.2 \times 0.3 \times 0.005\lambda_0$  at 869 MHz). The RFID TAGs that have the aforementioned dimensions can be used as standard ID badges.

Table III includes the comparison of dimensions as well as of read ranges of the RFID TAG based on the proposed TAG antenna and other commercially available TAGs, applicable for

<sup>1</sup>[Online]. Available: <http://trolleyscan.com/>, Jun. 5, 2006.

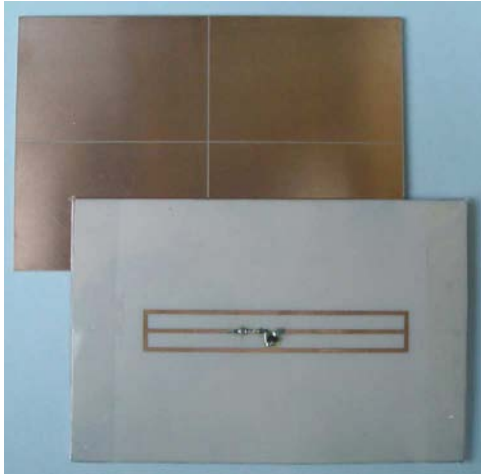


Fig. 1. Photograph of designed prototype of loop antenna closely spaced over patch array surface at distance  $d_1 = 0.24$  mm,  $d_1/\lambda_0 \sim 0.0007$ , which is situated over grounded dielectric slab, with height  $d_2 = 1.58$  mm,  $d_2/\lambda \sim 0.0046$ .

TABLE II  
EFFICIENCY AND GAIN OF LOOP ANTENNA FROM Fig. 1,  
EVALUATED BY WHEELER CAP METHOD [11]

	Radiation efficiency [%]	Antenna efficiency [%]	Directivity [dBi]	Gain [dBi]
Simulated, free space	53	39	5.3	1.3
Measured, free space	68	38	5.0	0.8
Measured, on phantom	70	33	5.4	0.6

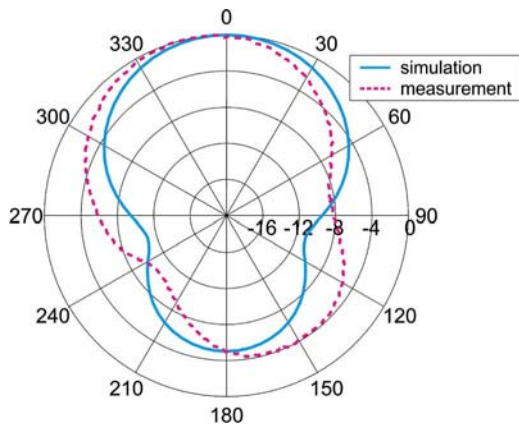


Fig. 2. Radiation pattern of new TAG antenna measured in free space.

the ID of people. Indeed, a majority of them are designed for the operation on metal objects. It is obvious that the new TAG provides the longest read range and the lowest TAG height as well. However, the presented data provide only directory information because in the majority of cases, the transmitted powers and the sensitivities of TAG chips and the readers used are unknown. It can be supposed that the transmitted power is 1 W, which corresponds to U.S. regulation ISO 18000-6. It should be emphasized that the recalculation of the read range of the new

TABLE III  
COMPARISON OF DIMENSIONS AND READ RANGES OF SEVERAL COMMERCIALY AVAILABLE UHF (860 ÷ 930 MHz) RFID TAGS, ABLE TO BE OPERATED ON HUMAN BODY (OR METALLIC OBJECTS)

TAG type	TAG dimensions $W \times L \times h$ [mm]	Maximum read range [m]
CR80 <sup>3)</sup>	---	3.7
WF-SM-12 <sup>3)</sup>	125 × 78.1 × 9.38	1.2
WF-SM-13 <sup>3)</sup>	190.6 × 20.3 × 17.2	1.8
WF-SM-14 <sup>3)</sup>	200 × 162.5 × 4.69	0.6
WF-SM-22 <sup>3)</sup>	112.5 × 28.1 × 4.69	0.9
WF-SM-23 <sup>3)</sup>	50 × 40.6 × 4.69	0.6
WF-SM-25 <sup>3)</sup>	150 × 6.25 × 6.25	2.7
WF-SM-26 <sup>3)</sup>	68.8 × 21.8 × 4.69	0.2
WF-SM-28 <sup>3)</sup>	118.8 × 43.75 × 7.8	0.9
WF-SM-40 <sup>3)</sup>	103 × 31.2 × 3.1	1.2
WF-SM-IN03 <sup>3)</sup>	137.5 × 6.25 × 6.25	2.7
WF-SM-SA <sup>3)</sup>	200 × 175	0.9
WF-SM-UTS <sup>3)</sup>	175 × 68.75 × 18.75	2.4
UHF metal Tag-01 <sup>4)</sup>	55 × 20 × 2	3.0
UHF metal Tag-02 <sup>4)</sup>	100 × 18 × 15	3.0
UHF metal Tag-03 <sup>4)</sup>	50 × 40 × 3	3.0
UHF metal Tag-06 <sup>4)</sup>	150 × 18 × 2	3.0
Proposed TAG	105 × 70 × 1.82 <sup>2)</sup>	4.8 <sup>1)</sup>

- 1) read range measured for  $P_t = 3.5$  W is 9 m (see Table IV)
- 2) height including chip and  $2 \times 0.2$  mm plastic cover is 2.72 mm.
- 3) [Online]. Available: <http://www.fricknet.com>, Jan. 16, 2009
- 4) [Online]. Available: <http://www.rfid-in-china.com>, Jan. 16, 2009

TAG from  $P_t = 3.5$  W (used during tests) to  $P_t = 1$  W results in the decrease of the read range from 9 m (measured in the open area) to 4.8 m. On the other hand, the new TAG used during tests is equipped with a relatively less sensitive chip. When using modern chips with the  $-14$ -dBm sensitivity, the read range can rise up to 10.9 m.

### III. SYSTEM POWER BUDGETS

As already mentioned, the performance and reliability of the ID depends on the reader-TAG and TAG-reader power budgets. The TAG chip input power  $P_{rTAG}$  must exceed the chip sensitivity  $P_{rTAGmin}$  (i.e., in this case,  $-6.9$  dBm)

$$P_{rTAG} \geq P_{rTAGmin}. \quad (1)$$

This condition provides the chip with the energy needed for the modulation of the reflected wave. Accordingly, in order to ensure the correct data processing, the input power  $P_{rREADER}$

of the reader receiver must be higher than the reader sensitivity  $P_{\text{rREADERmin}}$  (i.e., in this case,  $-64$  dBm)

$$P_{\text{rREADER}} \geq P_{\text{rREADERmin}}. \quad (2)$$

The power  $P_{\text{rTAG}}$  in dBm can be expressed as

$$P_{\text{rTAG}} = P_t - L - L_f \quad (3)$$

where  $P_t$  is the RF power transmitted by the reader in dBm,  $L$  denotes the link loss, and  $L_f$  represents the attenuation of the feeder cable in decibels. The peak power of the modulated signal reflected back from the TAG and received by the reader receiver  $P_{\text{rREADER}}$  can be expressed in dBm as follows:

$$P_{\text{rREADER}} = P_{\text{rTAG}} - L - L_f - L_{\text{conv}} \quad (4)$$

where  $L_{\text{conv}}$  is the conversion loss of the chip ( $\sim 20$  dB for the used chip). The maximum read distance  $d_{\text{max}}$  can be defined as the longest distance  $d$ , where conditions (1) and (2) are simultaneously fulfilled. In order to evaluate the conditions of the ID in different environments, it is necessary to calculate the corresponding link loss  $L$ .

#### A. Open Areas

The propagation of the electromagnetic wave from the reader to the TAG in an open space can be described by the modified two-ray model (see Fig. 3) and [2]. The model involves two paths of electromagnetic waves between the reader and TAG. The first one is formed by a direct ray, whereas the second one is formed by a ray reflected from the ground. The resulting radio link loss can be evaluated by means of the following formula:

$$L = -20 \log \left( \left( \frac{\lambda}{4\pi} \right) \sqrt{G_{tV}(\alpha_d) G_{rV}(\beta_d) G_{tH}(\gamma) G_{rH}(\delta)} \cdot \frac{1}{r_1} e^{-j \cdot k \cdot r_1} + \sqrt{G_{tV}(\alpha_r) G_{rV}(\beta_r) G_{tH}(\gamma) G_{rH}(\delta)} \cdot R(\vartheta) \cdot \frac{1}{r_2} \cdot e^{-j \cdot k \cdot r_2} \right) \quad (5)$$

where  $r_1$ ,  $r_2$  are the lengths of the direct and reflected rays,  $G_{rV}(\beta)$  and  $G_{rH}(\delta)$  stand for 3-D approximated angular dependencies of the reader antenna gain in the vertical and horizontal planes.  $G_{tV}(\alpha)$  and  $G_{tH}(\gamma)$  represent angular dependencies of the TAG antenna gain in the vertical and horizontal planes, while  $\bar{R}(\vartheta)$  is a complex reflection coefficient of the ground ( $\epsilon_r = 10$ ,  $\sigma = 10^{-2}$  S/m were considered).

#### B. Indoor Areas

The phenomena, which influence the reader-TAG link loss inside the buildings, are substantially more complicated than in the case of the open spaces. Since the electromagnetic waves interact with many surrounding obstacles, multiple reflections and diffractions must be taken into account. Many models and methods, which are applicable for the calculation of the path loss inside the buildings, can be found in the literature (see [19] and [20]).

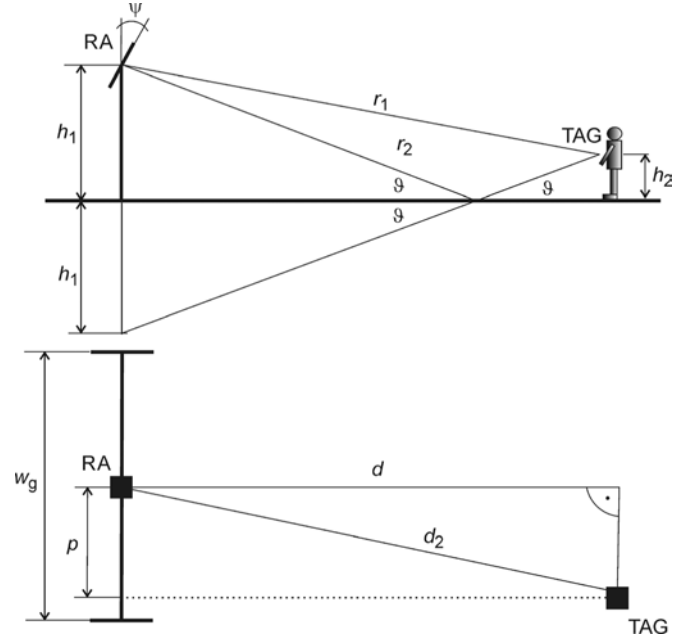


Fig. 3. Configuration of modified two-ray model—side view (upper) top view (bottom) with the following parameters:  $h_1$  height of reader antenna,  $h_2$  height of TAG antenna on person's chest,  $r_1$  direct ray trace,  $r_2$  reflected ray trace,  $d_2$  ground plane distance between reader and TAG antennas,  $w_g$  width of ID area,  $p$  reader, and TAG antenna axis offset.

In the empirical models, approximate mathematical formulas are used for the calculation of the received power. The latter is proportional to the distance from the transmitter  $d$  by the term  $(1/d)^n$ , where  $n$  stands for the path-loss exponent that is affected by the geometry, as well as by the electrical properties of the given environment.

In open areas, the value of the path-loss exponent is close to  $n = 2$ , whereas in corridors, the lower values are reported ( $n = 1.4$  in [19]). Thus, in comparison to the case of open areas, substantially longer read distances can be expected in corridors.

On the other hand, the deterministic or semideterministic models [21] utilizing the ray-tracing or ray-launching methods [20] are based on the geometry of the particular task (see Fig. 4) and can provide more precise results. In order to embrace as many propagation phenomena in corridors (with the given dimensions and material parameters) as possible, the 3-D ray-tracing method, implemented in the WinProp program,<sup>2</sup> was used. The aforementioned approach involves up to six reflections and two diffractions from brick walls ( $\epsilon_r = 4$ ,  $\sigma = 0.005$  S/m), a concrete floor, and ceiling ( $\epsilon_r = 6$ ,  $\sigma = 0.003$  S/m). The diffractions are calculated by the uniform theory of diffraction (UTD). The results of the performed ray-tracing simulations are presented in Section IV.

Since the ray-tracing method is unable to simulate the return path (TAG-reader) by itself, the calculations of these links are based on the reciprocity and were made using the following formula:

$$P_{\text{rREADER}} = 2 \cdot P_{\text{rTAG}} - L_{\text{conv}} - P_v. \quad (6)$$

<sup>2</sup>[Online]. Available: <http://www.ave-communications.com>, Nov. 15, 2008.

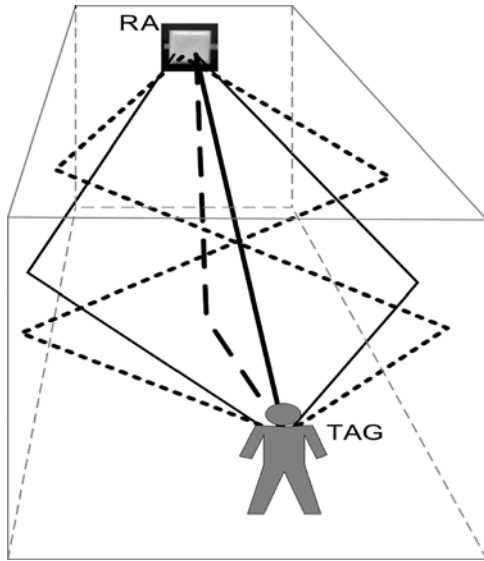


Fig. 4. Example of several rays launched in corridor.

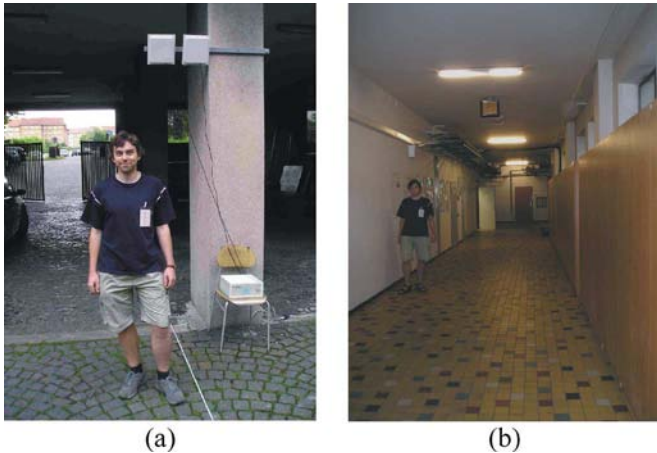
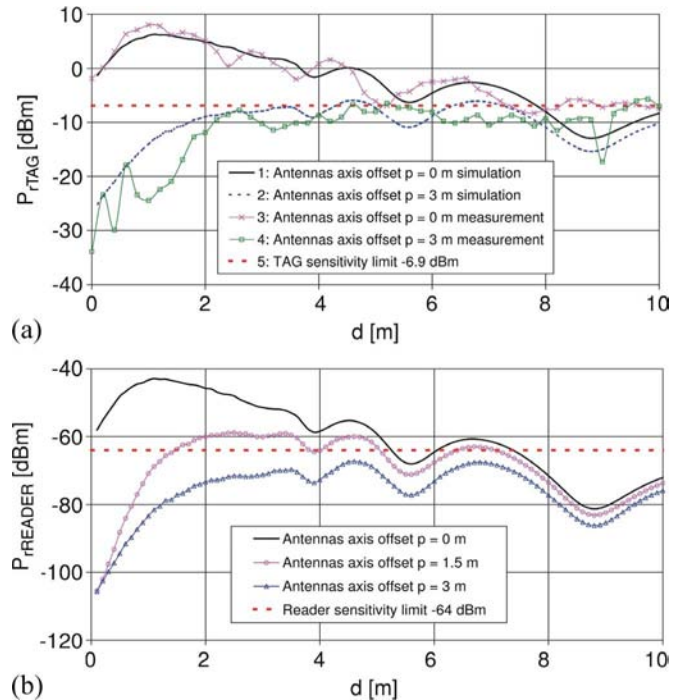
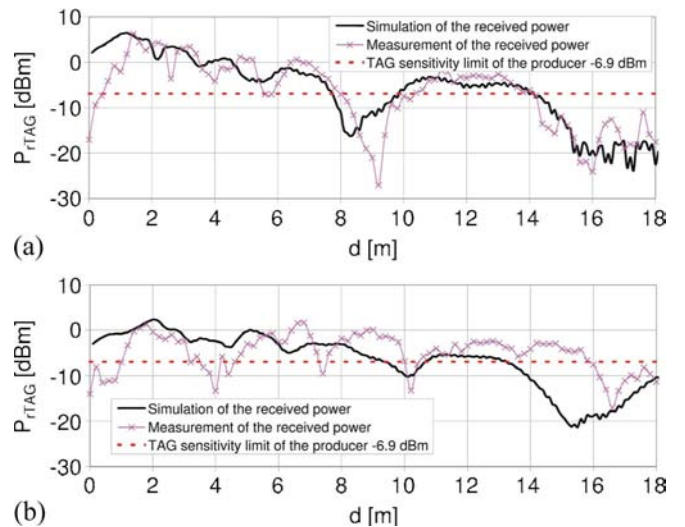


Fig. 5. Photograph of test configurations. (a) Person with chest-fixed TAG in open area. (b) Person with chest-fixed TAG in 4-m-wide corridor.

#### IV. PRACTICAL MEASUREMENTS

In order to verify the performed simulations, the  $P_{rTAG}$  values were measured in several test configurations that correspond to typical scenarios in people ID tasks. Moreover, the values of the maximum read distances  $d_{max}$  were also measured. The RF generator, the test antenna with the same gain as the new TAG antenna, and the spectrum analyzer were used for  $P_{rTAG}$  measurements. The new TAG antennas with the connected chip and reader were used for the  $d_{max}$  measurements. During both of the measurements, these antennas were fixed on a person's chest in the height of 1.25 m (see Fig. 5).

The measurements were performed in narrow and wide corridors (width of 2 and 4 m, respectively) and in an open area in front of the building. The 4-m-wide corridor has the following parameters: height of 3.35 m, length of 29 m, ended by a wall. The parameters of the 2-m-wide corridor are listed below: height of 3 m, length of 45 m, ended by a glass window. In all the configurations, the standard 8-dBi reader antenna was fixed at a height of 2.5 m with a tilt of  $\psi = 30^\circ$ . The TAG was attached on

Fig. 6. Simulated and measured received power: (a)  $P_{rTAG}$  and (b)  $P_{rREADER}$  versus ground plane distance  $d$  from reader antenna in open area.Fig. 7. Simulated and measured received power  $P_{rTAG}$  versus ground plane distance from reader antenna in 4-m-wide corridor. (a) Antennas axis offset  $p = 0$  m. (b) Antennas axis offset  $p = 1.8$  m.

a person's chest at the height of 1.25 m. The transmitted power equaled  $P_t = 35.4$  dBm. All values were measured at the axis of the ID area and also for several off-axis offset  $p$  values.

Since it is very difficult to measure the  $P_{rREADER}$  values (i.e., the peak power of the modulated reflected wave at the output of the receiving reader antenna in the presence of a strong nearby  $P_t$  power), these values were only simulated. As the link loss  $L$  values are identical in (3) and (4) and can be verified from the measurement of  $P_{rTAG}$ , this attitude seems to be acceptable. Since all plots include the corresponding  $P_{rTAGmin}$  and  $P_{rREADERmin}$  sensitivities, the positive ID can be expected in

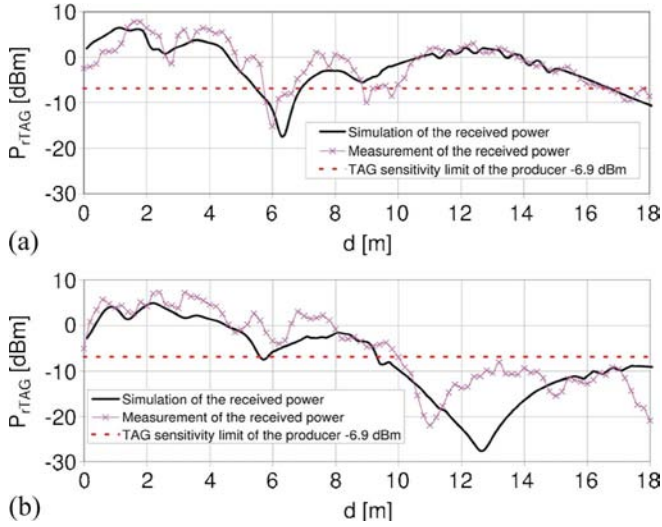


Fig. 8. Simulated and measured received power  $P_{T\text{TAG}}$  versus ground plane distance from reader antenna in 2-m-wide corridor. (a) Antennas axis offset  $p = 0$  m. (b) Antennas axis offset  $p = 0.8$  m.

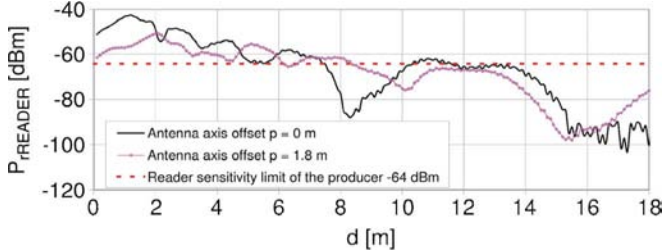


Fig. 9. Simulated received power  $P_{T\text{READER}}$  versus ground plane distance from reader antenna in 4-m-wide corridor.

all regions, where the  $P_{T\text{TAG}}$  and  $P_{T\text{READER}}$  values simultaneously exceed the given sensitivities. The measured  $d_{\text{max}}$  values are presented in Table III.

Fig. 6 expresses the simulated (two-ray model) and measured  $P_{T\text{TAG}}$  values as a function of the distance  $d$  from the reader in an open area. The plots show a very good agreement between the simulated and measured values, especially in the most important 2–8-m range. The maximum ID distance is approximately 9 m on axis; both the  $P_{T\text{TAG}}$  and  $P_{T\text{READER}}$  indicate the difficulties with the reliability of the off-axis ID. For practical implementations, the employment of more suitable reader antennas described in [22] can be recommended.

Fig. 7–10 show the simulated (ray tracing) and measured values of  $P_{T\text{TAG}}$  and  $P_{T\text{READER}}$  in 4- and 2-m-wide corridors. The agreement is acceptable because the majority of differences can be explained only by the estimated parameters of walls, their heterogeneities and reflections from the metal door and window frames, which were not included in the model. Nevertheless, it was observed that these influences had no essential impact on the ID distance of the RFID system. The measured  $d_{\text{max}}$  values are presented in Table IV.

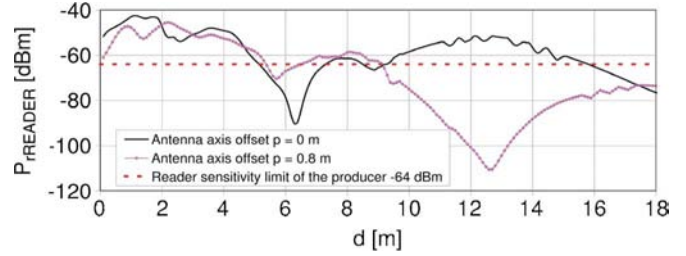


Fig. 10. Simulated received power  $P_{T\text{READER}}$  versus ground plane distance from reader antenna in 2-m-wide corridor.

TABLE IV  
READ RANGES OF TEST CONFIGURATIONS

Test configurations	Reader and TAG antenna axis offset [m]	Read range [m]			Ident. test, $d_{\text{max}}$
		Prediction			
		reader-TAG sim.	reader-TAG meas.	TAG-reader sim.	
Open area	0	8.0	7.2	7.2	9
	1	7.7	6.2	7.0	6.5
	2	7.6	4.0	5.0	4
	3	7 <sup>*)</sup>	unreliable	unreliable	unreliable
Cor. 4 m	0	13.8	13.8	11.0	9
	1.8	13	15.8	8.2	8
Cor. 2 m	0	16.4	16.4	15.8	16
	0.8	9.3	9.8	9.0	9

<sup>\*)</sup> small margin of 0.8 dB over chip sensitivity does not allow the reliable RFID system performance

### V. CONCLUSION

The implementation of every particular UHF RFID system has to be focused on the most sensitive components of the system. In case of the monitoring of people at moderate distances, this principle particularly concerns TAG antennas. The applicable TAG antenna should show small dimensions, exhibit a high immunity against the influence of a nearby human body and also provide a high antenna efficiency. For these purposes, a new dual-loop TAG antenna, loaded by a planar array of four sub-wavelength patches, was designed and manufactured.

The calculations of the read distance in open areas were performed using an analytical two-ray model. Similar calculations for indoor corridors were carried out using a 3-D ray-tracing method. All simulations were verified by a series of practical measurements. The presented plots show very good agreement between the calculated and measured results. The presented UHF RFID system exhibits 9-m read distance in open areas and up to 16 m in the narrower corridor.

A definite number of readers, placed in suitable positions, are able to ensure a reliable monitoring and ID of people moving in a building or the surrounding areas. Such a system can be applicable for various access systems.

## ACKNOWLEDGMENT

This study has been undertaken at the Department of Electromagnetic Field, Czech Technical University, Prague, Czech Republic.

## REFERENCES

- [1] K. Finkenzeller, *RFID Handbook: Fundamentals and Applications in Contactless Smart Cards and Identification*, 2nd ed. New York: Wiley, 2005.
- [2] M. Svanda, M. Polivka, and P. Hudec, "Application of the UHF RFID system for the identification of sportsmen in mass races," in *Proc. Eur. Microw. Assoc.*, Pisa, Italy, Dec. 2007, vol. 3, no. 4, pp. 294–301.
- [3] M. Gautherie, *Biological Basis of Oncologic Thermotherapy*. Berlin, Germany: Springer-Verlag, 1990.
- [4] P. R. Foster and R. A. Burberry, "Antenna problems in RFID systems," in *Proc. IEE RFID Technol. Colloq.*, London, U.K., Oct. 1999, pp. 31–35.
- [5] P. Raunonen *et al.*, "Folded dipole antenna near metal plate," in *Proc. IEEE AP-S Int. Symp.*, Jun. 2003, pp. 848–851, 0-7803-7846-6.
- [6] D. M. Dobkin and S. M. Weigand, "Environmental effects on RFID TAG antennas," in *Proc. IEEE AP-S Int. Symp.*, Washington, DC, Jul. 2005, 4 pp.
- [7] J. D. Griffin, G. D. Durgin, A. Haldi, and B. Kippelen, "RF TAG antenna performance on various materials using radio link budgets," *IEEE Antennas Wireless Propag. Lett.*, vol. 5, pp. 247–250, 2006.
- [8] L. Ukkonen, D. Engles, L. Sydänheimo, and M. Kivikoski, "Planar wire-type inverted-F RFID TAG antenna mountable on metallic objects," in *Proc. IEEE AP-S Int. Symp.*, Monterey, CA, Jun. 2004, pp. 101–104.
- [9] L. Ukkonen, L. Sydänheimo, and P. R. Kivikoski, "Effects of metallic plate size on the performance of microstrip patch-type TAG antennas for passive RFID," *IEEE Antennas Wireless Propag. Lett.*, vol. 4, pp. 410–413, 2005.
- [10] G. Marrocco, "RFID antennas for the UHF remote monitoring of human subjects," *IEEE Trans. Antennas Propag.*, vol. 55, no. 6, pp. 1862–1870, 2007.
- [11] G. A. Conway and W. G. Scanlon, "Low-profile patch antennas for over-body-surface communication at 2.45 GHz," *IEEE*, Cambridge, U.K., 2007, pp. 416–419.
- [12] D. C. Ranasinghe, D. M. Hall, P. H. Cole, and D. W. Engels, "An embedded UHF RFID label antenna for TAGging metallic objects," in *Proc. Intell. Sens., Sens. Network, Inf. Process. Conf.*, Dec. 2004, pp. 343–347.
- [13] J. Sidén, H.-E. Nilsson, A. Koptyug, and T. Olsson, "A distanced RFID dipole for a metallic supply chain label," in *Proc. IEEE AP-S Int. Symp.*, Albuquerque, NM, Jul. 2006, pp. 3229–3232.
- [14] D. F. Sievenpiper and L. Zhang *et al.*, "High-impedance electromagnetic surfaces with a forbidden frequency band," *IEEE Trans. Antennas Propag.*, vol. 47, no. 11, pp. 2059–2074, Nov. 1999.
- [15] M. Polivka, M. Svanda, and P. Cerny, "The design of multiple-arm folded dipole antenna operating closely spaced to a PEC," *Int. J. Wireless Opt. Commun.*, accepted for publication.
- [16] K. F. Lee and W. Chen, *Advances in Microstrip and Printed Antennas*. New York: Wiley, 1997.
- [17] S. Tretyakov, *Analytical Modeling in Applied Electromagnetics*. Norwood, MA: Artech House, 2003.
- [18] M. Švanda and M. Polívka, "Novel dual-loop antenna placed over patch array surface for UHF RFID of dielectric and metallic objects," *Microw. Opt. Technol. Lett.*, vol. 51, no. 3, pp. 709–713, Mar. 2009.
- [19] "Digital mobile radio towards future generation systems," COST Telecom Secretariat, CEC, Brussels, Belgium, COST 231 Final Rep., 1996.

- [20] M. F. Catedra and J. Perez-Arriaga, *Cell Planning for Wireless Communications*. London, U.K.: Artech House, 1999.
- [21] P. Pechac, M. Klepal, and K. Novotny, "Novel approach to indoor propagation modeling," *Radioengineering*, vol. 9, no. 3, pp. 12–16, 2000.
- [22] M. Polívka, A. Holub, and M. Mazánek, "Collinear microstrip patch antenna," *Radioengineering*, vol. 14, no. 4, pp. 40–42, 2005.



**Milan Polívka** (M'04) received the M.Sc. and Ph.D. degree in radioelectronics from the Czech Technical University, Prague, Czech Republic, in 1996 and 2003, respectively.

He is currently with the Department of Electromagnetic Fields, Czech Technical University, as an Assistant Professor. He has authored or coauthored over 60 scientific publications, including one book chapter and four utility models. He holds two patents. His research interests are focused on the field of the design of planar multibands, electrically small RFID and gain enhanced antennas, and application of artificial electromagnetic materials in the antenna field.

Dr. Polívka is a chair of the Microwave Theory and Techniques (MTT)/Antennas and Propagation (AP)/Electron Device (ED)/Electromagnetic Compatibility (EMC) joint section of the Czech–Slovak Chapter of IEEE since 2007.



**Milan Švanda** (S'08) received the M.Sc. degree from the Czech Technical University, Prague, Czech Republic, in 2007, and is currently working toward the Ph.D. degree in electromagnetic fields at the Czech Technical University.

His main research activities are aimed at the study of new materials in antenna technology. His other research interests are linked to the field of antennas, RFID, and metamaterials.



**Přemysl Hudec** received the M.Sc. and Ph.D. degree in radio electronics from the Czech Technical University, Prague, Czech Republic, in 1982 and 1995, respectively.

In 1982, he joined the Department of Electromagnetic Fields, Czech Technical University. His research activities include the design of microwave circuits and microwave measurement devices. In recent years, he has focused on microwave defense and security systems.



**Stanislav Zvánovec** (S'03–M'05) received the M.Sc. and Ph.D. degrees from the Czech Technical University, Prague, Czech Republic, in 2002 and 2006, respectively.

He is currently an Assistant with the Department of Electromagnetic Fields, Czech Technical University. His current research interests include electromagnetic wave propagation issues for millimeter-wave and quasi-optical and optical systems and UWB radio propagation channels.

## Research Article

# A Study of Gas and Rain Propagation Effects at 48 GHz for HAP Scenarios

S. Zvanovec, P. Piksa, M. Mazanek, and P. Pechac

*Department of Electromagnetic Field, Faculty of Electrical Engineering, Czech Technical University in Prague, Technicka 2, 166 27 Prague 6, Czech Republic*

Correspondence should be addressed to S. Zvanovec, xzvanove@fel.cvut.cz

Received 31 October 2007; Accepted 18 March 2008

Recommended by Marina Mondin

The atmosphere and rainfall significantly limit the performance of millimeter wave links and this has to be taken into account, particularly, during planning of high altitude platform (HAP) networks. This paper presents results from the measurement and simulation of these phenomena. A simulation tool from our previous analyses of terrestrial point-to-multipoint systems has been modified for HAP systems. Based on a rainfall radar database and gas attenuation characteristics as measured by a Fabry-Perot resonator, the performance of a simple link, two-branch diversity links, and more complicated HAP scenarios are discussed.

Copyright © 2008 S. Zvanovec et al. This is an open access article distributed under the Creative Commons Attribution License, which permits unrestricted use, distribution, and reproduction in any medium, provided the original work is properly cited.

## 1. INTRODUCTION

Several features in the atmosphere greatly limit system performance in the millimeter-wave band. This is true mainly for HAP systems working at a frequency of 48 GHz. Rain drops and atmospheric gas influence the propagation of electromagnetic waves in many ways, causing an undesirable decrease in the system's service availability.

The work presented here is partly based on our previous research, which was focused on terrestrial point-to-multipoint systems [1], where a terrestrial point-to-multipoint system outage improvement probability was derived as a function of rainfall and system parameters. A new method was proposed to classify the spatial properties of a rain event. The aim is to validate the applicability of the approach to HAP scenarios, where route diversity is applied. Rather than generating diversity gain statistics, system performance during a rain event is simulated in both time and space.

In order to support system performance analyses with appropriate input parameters, a gas attenuation measurement and a rainfall radar database are utilized.

The paper is organized along the following pattern. In the first part of the paper, the gas attenuation aspects are discussed. Measurement and simulation results together with an enhancement of the Fabry-Perot resonator measurement technique are then introduced. The next section deals with

the utilization of rainfall radar data during simulations of HAP systems. The following part reveals simulation results for a single link, two-branch diversity links, and a HAP system network, when the gas attenuation and the rainfall radar database are introduced. The paper concludes with a brief summary.

## 2. GAS ATTENUATION MEASUREMENTS

The atmosphere limits the performance of millimeter-wave systems. Many papers introducing gaseous attenuation measurements can be found in the literature (e.g., [2–4]). Most of the measurements performed to date are based on the radiometric approach, which uses a radiometer pointed at a satellite. Together with the attenuation, additional atmospheric properties such as temperature, pressure, and gas composition and humidity are collected. The attenuation introduced by atmospheric gases can either be described using an accurate physical model, such as Liebe's model [5] for frequencies ranging from 1 GHz up to 1 THz, or it can be approximated by probabilistic models such as the ITU-R P. 676 [6] or Salonen's models [7]. The ITU-R P.676 includes two models for the calculation of gaseous attenuation:

- (i) a complete line-by-line method, which sums the contributions from 44 oxygen lines and 30 water-vapor lines below 1000 GHz,

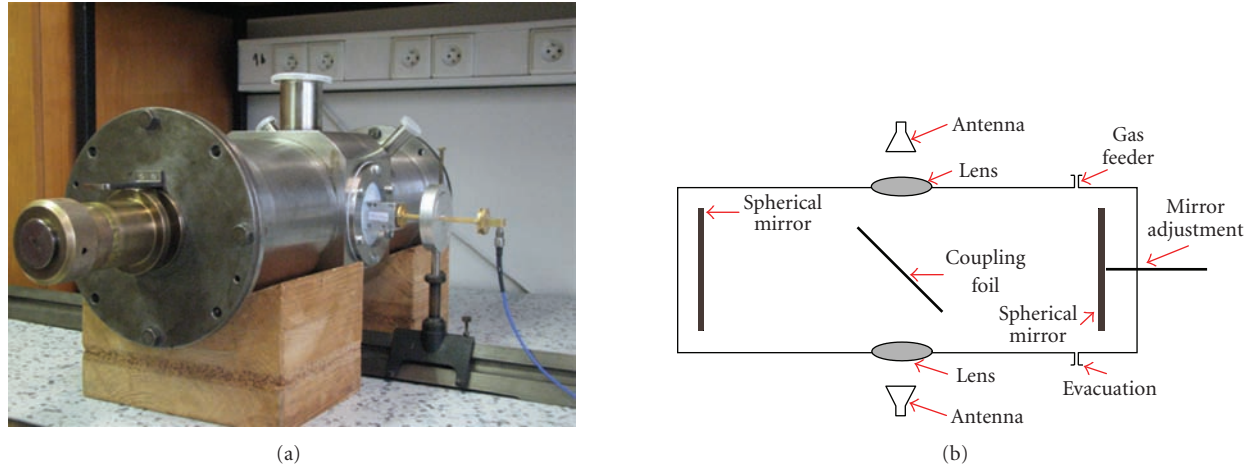


FIGURE 1: Fabry-Perot resonator for gas attenuation measurements: (a) equipment, (b) schematic.

- (ii) simplified algorithms based on a curve-fitting to the line-by-line calculation.

Nevertheless, in the HAP scenario, several different situations can be observed from the gas attenuation point of view. Atmospheric properties are different for inter HAP connections when compared to the classical HAP to ground user links. A support measurement system is advisable for a proper investigation of atmospheric attenuation.

The main aim of this section is to introduce a measurement system with the Fabry-Perot resonator (see Figure 1) and to discuss the results of both simulations and laboratory measurements of gas attenuation. The equipment itself was designed at the Czech Technical University in Prague. Several aspects of the experiments described below supplement the millimeter-wave high resolution spectroscopy measurement campaign [8], which has been accomplished in cooperation with the Institute of Chemical Technology in Prague.

### 2.1. Enhancements of the measurement technique

The principal virtue of laboratory measurements of atmospheric gases lies in the possibility of adjusting the gas medium in terms of the homogeneity of a particular gas composition, and in terms of the proper distribution, temperature, and pressure, a situation which can never be truly achieved in the case of open range measurements. Spectroscopy cavities, Fabry-Perot resonators [9], or very long tubes introducing extremely precise tools compared to the statistically-based measurements in open areas, where the variability of the atmosphere cannot be adequately defined.

A Fabry-Perot resonator (Figure 1(a)) working from 18 GHz up to hundreds of GHz was developed for the gas attenuation measurements. The main layout of the resonator is depicted in Figure 1(b). It comprises a tube-shaped cavity, two spherical mirrors positioned to set particular resonances, and a dielectric foil placed inside a cavity. One mirror is placed in a fixed position, while a second mirror can be adjusted in  $1\ \mu\text{m}$  steps. The foil accomplishes the transition of electromagnetic waves via dielectric lenses into and from the perpendicularly placed feeders.

The sensitivity of the Fabry-Perot resonant cavity is the result of its very high-quality factor. In this case, the absorption measurement is based on the measurement and consequential evaluation of the quality factor of the empty and gas-filled resonator.

The Fabry-Perot resonator was simulated via the FEKO electromagnetic simulator [10] using a method of moments in frequency domain with approximations of the multilevel fast multipole method (MLFMM) on metallic mirrors and the uniform theory of diffraction (UTD) on dielectric foil. The simulated resonator deployment can be seen in Figure 2(a). In order to simplify the simulations, only mirrors (shown squared in the direction of the  $x$ -axis) and a coupling foil were considered. The electromagnetic field is fed toward the  $z$ -axis (in a downwards direction).

The data of the near field obtained from the simulation were thereafter analysed in Matlab. The main objective was to obtain a frequency dependence of the transferred power. Based on these simulations, the parameters of the resonator were derived in order to reach the highest possible quality factor values. Performance of the Fabry-Perot resonator in terms of the radiation pattern (i.e., scattering of energy from the center of the coupling foil in specific directions), as simulated in FEKO, is depicted in Figures 2(b) and 2(c). In the case of an arbitrary nonresonant frequency (see Figure 2(b)), almost all energy is transmitted through the resonator. On the contrary, during the resonance (Figure 2(c)), in this particular graph at the frequency of 30 GHz, part of energy is absorbed into the resonator, and part is reflected back to the transmitter.

Losses observed in the Fabry-Perot resonator comprise the measured attenuation of an inserted medium, an additional undesirable diffraction, reflection losses at the mirrors, and coupling loss due to the dielectric foil. To properly design the measurement equipment, these additional frequency dependent losses have to be eliminated as much as possible. The first of the losses, the reflection loss, was decreased during system tuning by the  $5 \cdot 10^{-5}$  m thick golden layer on the mirrors, which fully met the required depth of penetration for the gold of  $0.59 \cdot 10^{-6}$  m at the lowest working

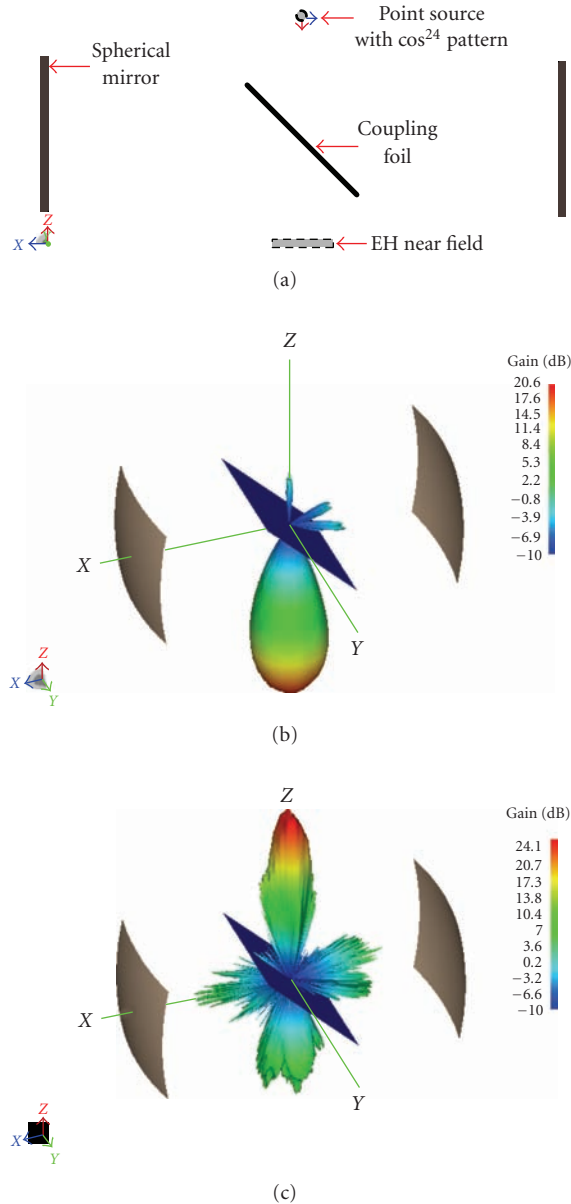


FIGURE 2: Performance of the Fabry-Perot resonator: (a) configuration, (b) results in terms of the radiation pattern as simulated in FEKO for the nonresonant frequency, (c) as simulated for the resonant frequency.

frequency of the resonator (18 GHz). The diffraction loss, introducing a spilling over of electromagnetic wave at the mirrors, was accompanied by a proper relation between the distance and curvature of the mirrors. A stainless steel tube-shaped cavity with a length of 0.555 m and diameter of 0.189 m, and two positioned spherical mirrors with 0.455 m radius of curvature were utilized. The confocal deployment of mirrors was chosen in order to meet a stability criterion for the Fabry-Perot resonator. The last negative loss, introduced by the coupling loss, was found to be dependent on the thickness and material parameters of the dielectric coupling foil. A 0.1 mm thick dielectric polythene coupling foil (see in Figure 2(a)) was inserted inside the resonator cavity in order

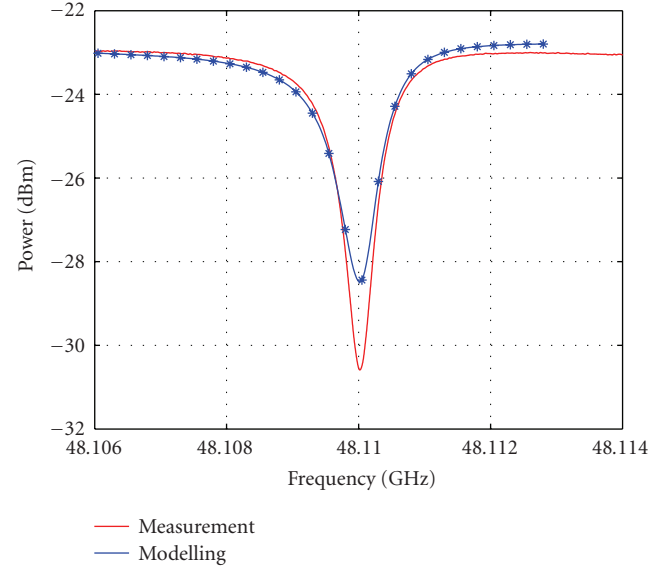


FIGURE 3: Comparison of measured and simulated received signal levels at a resonant frequency of 48 GHz.

to accomplish the transition of electromagnetic waves into and from the perpendicularly placed feeders.

It should be emphasized that the developed Fabry-Perot resonator is suitable for a frequency range from 18 GHz (lower frequencies are limited by diffraction losses at the mirrors) to 400 GHz, where coupling losses at the dielectric foil predominate.

Energy is led into and out of the resonator via dielectric lenses (placed in the two opposite side windows of the resonator; one of these windows can be seen in Figure 1), whose parameters had to be derived using CST microwave studio [11] simulations. It has to be emphasized that this software was used because a horn antenna and dielectric lens can be simulated more effectively in CST in the time domain (only a single simulation needed for the broadband response) than in FEKO in the frequency domain (above discussed simulations). The main demands were to ensure the best Gaussian distribution of the electromagnetic field coupling into the resonator, to keep a uniform waveform inside the resonator, and to avoid saturation of the measured gas due to the improper focusing of the energy. The optimal field distribution on the coupling foil and the position of the feeding antenna in front of the lens were also optimized (in accordance with [12]). Teflon (PTFE) with  $\epsilon_r = 2.02$  and  $tg\delta = 0.003$  was utilized for the lenses. The optimal lens shape, having a spherical inner surface and an elliptical outer surface, was derived.

## 2.2. Gas attenuation measurement results

Measurements of the gas attenuation were accomplished with the Fabry-Perot resonator. The comparison of the measured and simulated received signal levels of Fabry-Perot resonator filled with standard laboratory air at the resonant frequency of 48 GHz is shown in Figure 3. Although both the measured and the simulated resonance have similar

shape and the same resonant frequency, an undesired slight difference in the peaks at the resonant frequency can be observed in the graph. It is caused by the fact that it was impossible to get exact properties of the air medium for the simulation tool in this test measurement.

A comparison of measured gas attenuation and the attenuation derived by ITU-R P.676 [6] for the standard atmosphere at a temperature of 293.15 K, a pressure of 1013 MPa, and a water vapor density of  $7.5 \text{ g/m}^3$  is depicted in Figure 4. In this case, the gas attenuation was measured in the frequency range from 47.9 GHz to the 48.2 GHz assigned for HAP downlink connections (ITU-R E.1550 [13]). Differences between the measured and calculated values can be caused by additional gas molecules in the measured gas medium, which are not considered in ITU (it comprises oxygen and water-vapor lines only). For example, the resonance of an asymmetric molecule of  $\text{H}_2\text{S}$  can be observed near the frequency 48 GHz [14].

### 3. RAINFALL RADAR DATA

Rain events can affect the propagation of electromagnetic waves in the millimeter wave band much more significantly than gas attenuation. For a proper assessment of the rain's influence, it is crucial not to limit oneself only to statistics valid for a single earth station to HAP link. Time and spatial dependences should also be taken into account. Rainfall radar data for a given region [15] were used as input for the simulations. Data were taken from a modern weather radar network (CZRAD) consisting of two state-of-the-art Doppler C-band weather radars, which cover the entire area of the Czech Republic with volume scans of up to 256 km in range [16]. The principle of Doppler radars is based on the transmission of electromagnetic energy into the atmosphere (hundreds of pulses per second) and the reception of backscattered energy. Doppler radars provide measurements not only of the radar reflectivity but also of the frequency change of the backscattered signal, which can be used to determine the radial velocity of atmospheric precipitation. For specific purpose, radar images with dimensions of  $50 \times 50 \text{ km}$ , a 1 km grid, and 1-minute time steps were generated. Areas of up to  $150 \times 150 \text{ km}$  can be analyzed from these rainfall radar scans.

A rain event database containing over 1.5 million radar images for the Czech Republic for the period from 2002–2004 was created for the simulations [1]. One of the rain scans from the middle of the rain event in 2003 is depicted in Figure 5. Three significant intensive rain cells with rain rates higher than 60 mm/hour were observed.

### 4. HAP PERFORMANCE SIMULATION

In order to fully analyze propagation issues for HAP systems at the frequency of 48 GHz, a propagation simulation tool was developed. The core of the tool was incorporated from our previous work [1] dealing with terrestrial point-to-multipoint networks. Several modifications had to be made in order to adapt the computation models to HAP scenarios. The possibility of specifying the positions and distributions

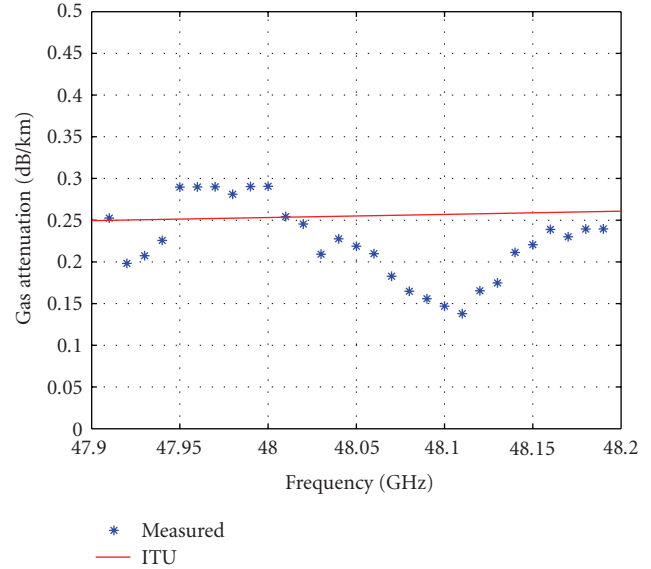


FIGURE 4: Comparison of the measured gas attenuation to [6].

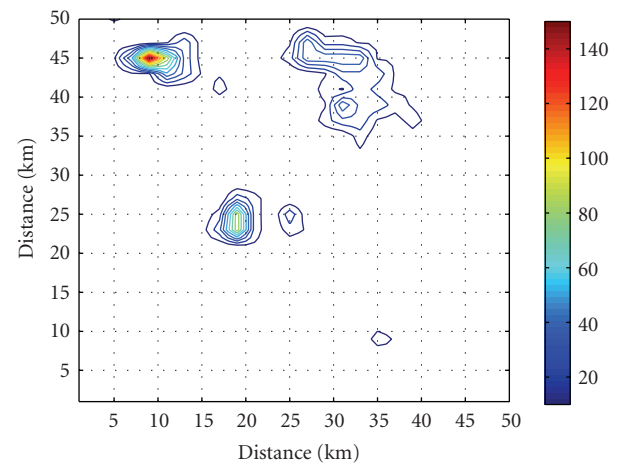


FIGURE 5: Rain distribution (contours) in mm/hour during a rain event.

of both ground users and HAP stations, respectively, can be emphasized as the main feature from a scenario deployment point of view. This tool includes the essential parameters for investigation of wave propagation in the millimeter-wave band:

- (i) rain characteristics—either statistically described parameters based on [17] or the above-mentioned rainfall radar data,
- (ii) gas attenuation—this measurement was discussed in the previous section.

Based on input parameters, several HAP propagation features, ranging from simple link statistics up to complex HAP network performance, can be analyzed. Results from propagation analyses will be discussed in the following sections.

#### 4.1. Single link and two diversity links deployment

Single HAP to a ground user link suffers from temporal rain attenuation. To combat this phenomenon, suitable rain fade margins are set during an assessment of the link budget or fade mitigation techniques, like power control and adaptive coding, are implemented [18]. Nevertheless, this solution is not always possible, particularly, for services requiring high availability. The cumulative distribution function of rain attenuation as analyzed for a 10 km (ground distance) link from the user to the HAP, which was set in the attitude of 20 km, is depicted in Figure 6. The curve is valid for the annual rain evolution over Prague, Czech Republic, in 2002.

An outage of a connection to the main HAP can be mitigated if users affected by the rain could reconnect to another station using route diversity (the principal scenario of route diversity can be seen in Figure 7). This is especially true for distant users, whose links to the main HAP could lead through a rainy area, even though these particular users are not themselves experiencing the rain event. The improvement in performance in dB between the single link attenuation and the joint two links attenuation at a given probability level is often referred as the diversity gain. The improved availability of particular user when route diversity is utilized can be evaluated or measured by the joint attenuation statistics. Many researches in a similar field have already been carried out dealing with earth-space diversity [19] and with diversity for terrestrial point-to-multipoint systems (e.g., [20, 21]). In [22], a method to establish the joint site attenuation statistics for a HAP station connected with two earth stations was developed based on combinations of satellite earth and terrestrial approaches. An analysis of the proper deployment of two diversity terminals received from a single HAP station was presented. The optimal diversity user separation has been found to be 10 to 20 km, providing 99.9% availability. A similar approach (although more in-depth), which considered correlations of rain attenuation distributions, was derived in [23].

The comparison of complementary cumulative distribution functions of rain attenuation for the above-discussed single HAP to user link at 48 GHz and, newly, for two-branch diversity links, where a user is able to connect to two HAPs, can be seen in Figure 6. In the latter case, one of the two diversity links was identical ( $d_{\text{main}} = d_{\text{diversity}}$ ) to the standalone link and the second was angularly separated by  $\varphi = 120^\circ$ ; both links had land distance of 10 km.

The diversity gain is expressed in Table 1. It can be clearly seen that a diversity gain of 1.5 dB for 99.9% availability can be achieved using route diversity. The diversity gain has a tendency to increase with the required availabilities (e.g., 7.1 dB for 99.99%).

The graph we referred to above only gives an illustrative example of the application of route diversity. The diversity gain is dependent on link length ratios, angular separations, and availabilities.

#### 4.2. Utilization of route diversity in HAP systems

A more sophisticated approach involves an analysis of the whole system within a given area. The performance of the

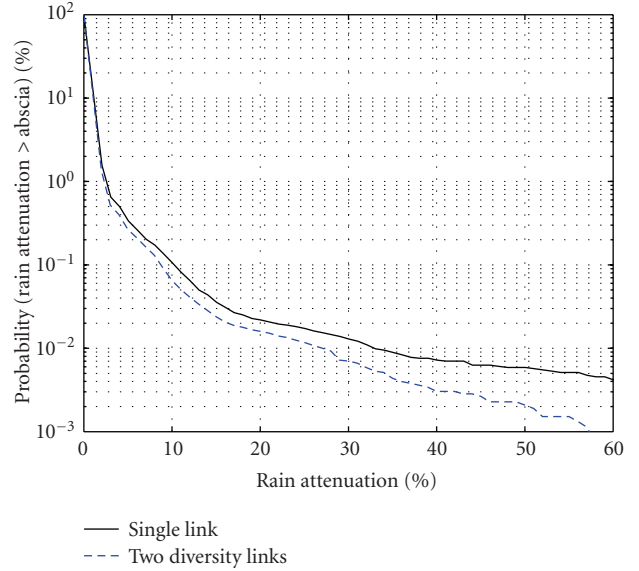


FIGURE 6: CDFs of rain attenuation for a single link and two-branch diversity links with the angular separation of 120 degrees and a ground link distance is 10 km.

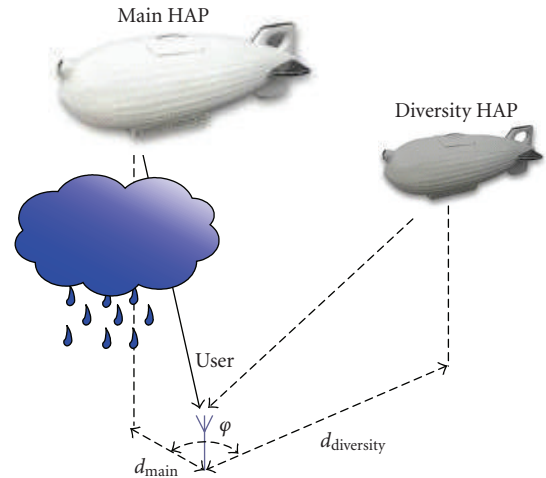


FIGURE 7: Basic scenario of the route diversity.

HAP system can be assessed in terms of outage probability in relation to the total number of operated links. The case discussed above, with two joined links, is now spread over a particular area based on the assumption that each user has the possibility of choosing another HAP station in the event of a link outage due to rain attenuation. In this way, HAP system performance can be studied simultaneously. In [24], different system outages during two storms with similar characteristics common for single links, but with different spatial features were analyzed.

To analyze system performance, an outage improvement probability  $P(\%)$ —a parameter taken from terrestrial point-to-multipoint system analyses [1]—was utilized. The outage

TABLE 1: Diversity gain of two diversity links with an angular separation of 120 degrees and a ground link distance of 10 km.

Availability (%)	Diversity gain (dB)
99.000	0.4
99.900	1.5
99.950	2.0
99.970	2.5
99.990	7.1
99.995	20.5
99.997	27.9
99.999	34.4

improvement probability is defined as the percentage of users with a successfully established diversity link out of the total number of users receiving a signal level from the nearest HAP below the threshold due to the rainfall. It can be expressed as [1] follows:

$$P = a_{\text{const}} \cdot \left( 1 - \left( \frac{\vartheta - \pi}{\pi - b_{\text{const}} \sqrt{1 - (d_{\text{main}}/d_{\text{div}})^2}} \right)^2 \right) \cdot \left( \frac{d_{\text{main}}}{d_{\text{div}}} \right)^{c_{\text{const}}}, \quad (1)$$

where  $\vartheta$  (rad) and  $d_{\text{main}}/d_{\text{div}}$  (-) stand for the angle separation and the ratio of the main and diverse link lengths, respectively.  $a_{\text{const}}$ ,  $b_{\text{const}}$ , and  $c_{\text{const}}$  are empirical parameters, that were derived [1] to be dependent on maximum rain rate, the rain fade margin, and the rain spatial parameter (useful for rain spatial classification according to rain impact on system performance).

The results of the analyses of HAP system performance were compared to the outage improvement probability statistics valid for a terrestrial system with the same parameters [25]: transmitter power 30 dBm, HAP antenna gain 29 dBi, ground terminal station antenna gain 39 dBi, and rain margin 24 dB. The particular example of the comparison of outage improvement probabilities as a function of the link length ratio ( $d_{\text{main}}/d_{\text{diversity}}$ ) and the angular separation ( $\varphi$ ) is for the particular rain scan as shown in Figure 8. For the sake of clarity, specific values from Figure 8 are given in Table 2.

It can be concluded that when route diversity is utilized a better performance improvement can be observed during a rain event in the HAP network than in the case of a terrestrial point-to-multipoint system. In our example, over 2.6% of mean outage improvement probability can be obtained (up to a peak of 5.5%; for angular separation  $\varphi$  near 180 degrees and a main to diverse link length ratio  $d_{\text{main}}/d_{\text{diversity}} = 1/2$ ).

## 5. CONCLUSION

In this paper, propagation issues related to HAP systems working at 48 GHz were presented and their specific features were analyzed. A Fabry-Perot resonator-based measurement system was introduced, and simulation and measurement results were discussed. This method can be used to study additional gas attenuation for specific HAP to ground links

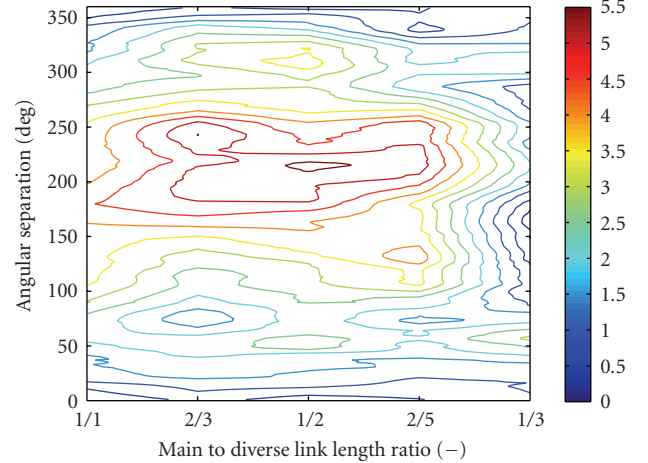


FIGURE 8: Comparison of outage improvement probabilities for HAP and a terrestrial network for the rain scan from Figure 5.

TABLE 2: Specific differences between outage improvement probabilities  $\Delta$ (%) from Figure 8.

Link length ratio (-)	Angular separation (deg)	$\Delta$ (%)
1/1	90	3.0
2/3	90	1.8
2/3	180	4.9
1/2	45	2.3
1/2	90	2.6
1/2	180	5.0

and inter HAP connections in higher layers of the earth's atmosphere.

The rain attenuation was also analyzed taking into account single link availability as well as the system performance for more complex HAP scenarios. Simulations of HAP system performance using route diversity during a rain event indicated that a higher outage improvement probability can be reached in a HAP system, when compared to a terrestrial point-to-multipoint system.

## ACKNOWLEDGMENTS

The research is a part of the activities of the Department of Electromagnetic Field of the Czech Technical University in Prague within the framework of the research Project of the Ministry of Education, Youth, and Sports of the Czech Republic no. LC06071 Centre of Quasi-Optical Systems and Terahertz Spectroscopy.

## REFERENCES

- [1] S. Zvanovec and P. Pechac, "Rain spatial classification for availability studies of point-to-multipoint systems," *IEEE Transactions on Antennas and Propagation*, vol. 54, no. 12, pp. 3789–3796, 2006.
- [2] J. H. van Vleck, "The absorption of microwaves by oxygen," *Physical Review*, vol. 71, no. 7, pp. 413–424, 1947.

- [3] J. H. van Vleck, "The absorption of microwaves by uncondensed water vapor," *Physical Review*, vol. 71, no. 7, pp. 425–433, 1947.
- [4] H. J. Liebe, G. G. Gimmestad, and J. D. Hopponen, "Atmospheric oxygen microwave spectrum—experiment versus theory," *IEEE Transactions on Antennas and Propagation*, vol. 25, no. 3, pp. 327–335, 1977.
- [5] H. J. Liebe, "Modeling attenuation and phase of radio waves in air at frequencies below 1000 GHz," *Radio Science*, vol. 16, no. 6, pp. 1183–1199, 1981.
- [6] International Telecommunications Union, "Attenuation by Atmospheric Gases," ITU-R Recommendation, pp. 676–6, 2005.
- [7] E. Salonen, S. Karhu, P. Jokela, et al., "Study of Propagation Phenomena for Low Availability," Final Report, ESA/ESTEC Contract 9455/91/NL/LC(SC), 1994.
- [8] P. Kania, L. Stříteská, M. Šimečková, and Š. Urban, "Pressure shifts of acetonitrile ground state parameters," *Journal of Molecular Structure*, vol. 795, no. 1–3, pp. 209–218, 2006.
- [9] E. P. Valkenburg and V. E. Derr, "A high-Q Fabry-Perot interferometer for water vapor absorption measurements in the 100 Gc/s to 300 Gc/s frequency range," *Proceedings of the IEEE*, vol. 54, no. 4, pp. 493–498, 1966.
- [10] "The FEKO," <http://www.feko.info/>.
- [11] "The CST," <http://www.cst.com/>.
- [12] T. A. Milligan, *Modern Antenna Design*, Wiley-IEEE Press, New York, NY, USA, 2nd edition, 2005.
- [13] International Telecommunications Union, "Preferred Characteristics of Systems in the Fixed Service Using High Altitude Platforms Operating in the Bands 47.2–47.5 GHz and 47.9–48.2 GHz," ITU-R Recommendation F.1500, 2000.
- [14] S. N. Ghosh and H. D. Edward, "Report No. 82," Geo-Physics Research Directorate, Airforce Cambridge Research Centre, 1956.
- [15] Z. Sokol, "The use of radar and gauge measurements to estimate areal precipitation for several Czech River Basins," *Studia Geophysica et Geodaetica*, vol. 47, no. 3, pp. 587–604, 2003.
- [16] P. Novak and J. Kracmar, "New data processing in the Czech weather radar network," in *Proceedings of the 2nd European Conference on Radar in Meteorology (ERAD '02)*, vol. 1 of *ERAD Publication Series*, pp. 328–330, Delft, The Netherlands, November 2002.
- [17] L. Féral, H. Sauvageot, L. Castanet, and J. Lemorton, "HYCELL—a new hybrid model of the rain horizontal distribution for propagation studies: 1. Modeling of the rain cell," *Radio Science*, vol. 38, no. 3, 2003.
- [18] A. Maurolagoitia, J. M. Riera, P. Garcia, and A. Benarroch, "Performance of fade mitigation techniques in a fixed 48 GHz HAPS network," *International Journal of Wireless Information Networks*, vol. 13, no. 1, pp. 19–30, 2006.
- [19] COST 255, "Radiowave Propagation Modelling for New Satellite Communication Services at Ku-Band and above," Final Report, Brussels, Belgium, 2002.
- [20] K. S. Paulson, R. J. Watson, and I. S. Usman, "Diversity improvement estimation from rain radar databases using maximum likelihood estimation," *IEEE Transactions on Antennas and Propagation*, vol. 54, no. 1, pp. 168–174, 2006.
- [21] K. S. Paulson, "Prediction of diversity statistics on terrestrial microwave links," *Radio Science*, vol. 38, no. 3, 2003.
- [22] T. Konefal, C. Spillard, and D. Grace, "Site diversity for high-altitude platforms: a method for the prediction of joint site attenuation statistics," *IEE Proceedings: Microwaves, Antennas and Propagation*, vol. 149, no. 2, pp. 124–128, 2002.
- [23] A. D. Panagopoulos, E. M. Georgiadou, and J. D. Kanellopoulos, "Selection combining site diversity performance in high altitude platform networks," *IEEE Communications Letters*, vol. 11, no. 10, pp. 787–789, 2007.
- [24] S. Zvanovec and P. Pechac, "Wave propagation simulations at 48 GHz for HAPs using rainfall radar data," in *Proceedings of the 1st COST 297—High Altitude Platforms for Communications and Other Services Workshop (HAPCOS '06)*, York, UK, October 2006.
- [25] FP6—CAPANINA, "Deliverable 14—Mobile Link Propagation Aspects, Channel Model and Impairment Mitigation Techniques," April 2005.